A FPGA based laser DPLL for atom interferometry

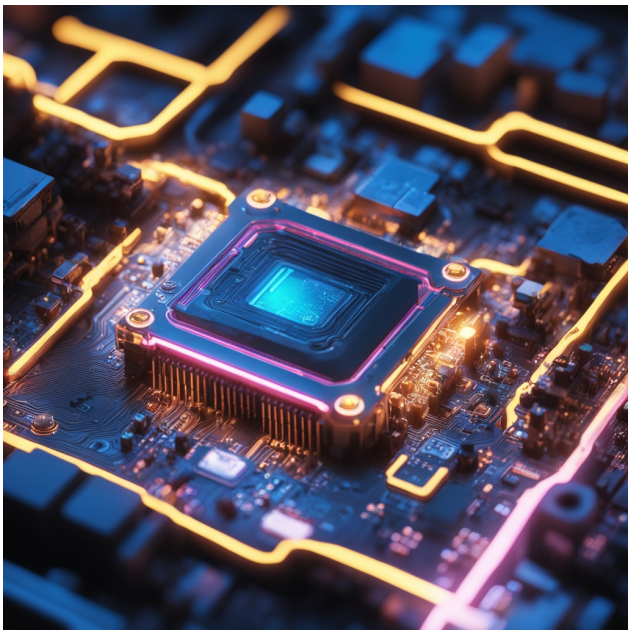

Von der QUEST-Leibniz Forschungsschule der
Gottfried Wilhelm Leibniz Universität Hannover
Zur Erlangung des Grades

Doktor der Naturwissenschaften

- Dr. rer. nat. -

genehmigte Dissertation von

Alexandros Papakonstantinou, M.Sc.

2024

Referent:	Prof. Dr. Ernst M. Rasel Institut für Quantenoptik Leibniz Universität Hannover
Korreferent:	Prof. Dr. Silke Ospelkaus Institut für Quantenoptik Leibniz Universität Hannover
Korreferent:	Dr. Sven Herrmann ZARM Universität Bremen
Vorsitz der Promotionskommission:	Prof. Dr. Luis Santos Institut für Theoretische Physik Leibniz Universität Hannover
Datum der Promotion:	02.11.2023

Alexandros Papakonstantinou: *A FPGA based laser DPLL for atom interferometry*,
PhD Thesis, Leibniz Universität Hannover ©2024

Abstract

Atom interferometers have gained attention in both fundamental physics research and practical applications thanks to their high accuracy. Improving them is a widespread area of research and generating highly phase stabilized light fields is crucial for enhancing their accuracy, pushing the requirements to their hardware beyond state-of-the-art.
Bose-Einstein condensates (BECs) are particularly advantageous as a probe in e.g. a classical Mach-Zehnder setup, since they enhance the interferometer's sensitivity due to their long possible observation times. These longer observation times, compared to thermal ensembles, allow for more precise measurements of accelerations by detecting the quantum mechanical phase of the atomic ensembles after an interferometry sequence. The creation of a BEC is a complex process that requires coherent, frequency stabilized light of different wavelengths.
Moving an AI which uses BECs into a microgravity environment allows for smaller apparatuses and longer interferometry sequences. However, the requirements in terms of accuracy for the hardware that drives the laser systems remain but their size, weight and power budget need to be reduced for space-born apparatuses.
One possible way to measure the quantum mechanical phase of an interferometer output is Raman double diffraction. For this purpose, a FPGA based digital phase locked loop (DPLL) was developed and evaluated for the usage in an atom interferometer with Raman double diffraction within the sounding rocket missions of MAIUS-B.
For space applications a digital system is very favorable since parameters of the loop can be adjusted without soldering and with communication from a distance. Furthermore, the digitally tunable Numeric Controlled Oscillator (NCO), implemented as the reference oscillator, enables tuning setpoints as high as the laser current range of the hardware. Additionally, the digital Phase Frequency Detector (PFD) of the DPLL can read phase errors between the reference and laser beat signals up to $2\,\mathrm{GHz}$ in combination with the developed hardware without external frequency dividers. Hence, the capture range of the phaselock is only limited by the hardware.
In the course of this thesis, the DPLL was successfully tested on multiple laser systems as well as with an electronic Voltage Controlled Oscillator (VCO). A characterization of the phaselock was achieved through evaluation of the conducted measurements at different laser system setups. A phase noise suppression to approximately $-60\,{}^{dBc}/_{\mathrm{Hz}}$ for frequencies between $100\,\mathrm{Hz}$ and $1\,\mathrm{MHz}$ around the carrier was achieved. Highly optimized optical PLLs achieve phase noise suppression to $-120\,{}^{dBc}/_{\mathrm{Hz}}$ at the expense of size, cost and complexity compared to the DPLL. Jumping between frequency setpoints with ECDLs showed that the DPLL was able to realize far frequency jumps up to $2\,\mathrm{GHz}$ in approximately $420\,\mu\mathrm{s}$.
Ultimately, the DPLL was able to drive Rabi oscillations with ^{87}Rb BECs and realize beam splitter and mirror pulses intended for Raman double diffraction with an efficiency of up to $97\,\%$ excited atoms. Afterwards, the adjusted light pulses were used for interferometry sequences, where an intentional tilt of the apparatus was measured through the population difference of the atomic states.
Overall, a hardware setup time within one day was achieved for different laser systems and a successful adjustment of the DPLL's parameters to achieve a phaselocked laser beat signal could be accomplished within a few hours.

Keywords: **digital phase-locked-loop**, **Raman double diffraction**, **microgravity**

Kurzfassung

Atominterferometer haben sowohl in der physikalischen Grundlagenforschung als auch in praktischen Anwendungen dank ihrer hohen Genauigkeit Aufmerksamkeit erhalten. Ihre Verbesserung ist ein weit verbreitetes Forschungsgebiet und die Erzeugung phasenstabiler Lichtfelder ist entscheidend für die Erhöhung ihrer Genauigkeit. Die Anforderungen, um besagte Lichtfelder erzeugen zu können, fordern die Hardware über den Stand der Technik hinaus.
Bose-Einstein-Kondensate (BEKs) sind aufgrund ihrer langen Verweildauer im Interferometer besonders vorteilhaft, da diese die Empfindlichkeit des Interferometers, beispielsweise im klassischen Mach-Zehnder-Aufbau, erhöhen. Die längere Verweildauer, verglichen mit thermischen Atomwolken, ermöglicht präziesere Messungen von Beschleunigungen durch Messung der quantenmechanischen Phase am Interferometerausgang. Die Erzeugung solcher BEKs ist ein komplexer Prozess für den frequenzstabilisiertes, kohärentes Licht verschiedener Wellenlängen benötigt wird. Der Aufbau eines Interferometers mit BEKs in einer Mikrogravitationsumgebung ermöglicht außerdem kleinere Apparate und längere Interferometriesequenzen. Die Anforderungen an die Genauigkeit der Hardware, die die Lasersysteme antreibt, bleiben jedoch bestehen, aber ihre Größe, ihr Gewicht und ihr Energiebudget müssen für weltraumtaugliche Geräte reduziert werden.
Eine Möglichkeit die quantenmechanische Phase eines Interferometerausgangs zu messen, ist die Raman-Doppelbeugung. Zu diesem Zweck wurde im Rahmen des MAIUS-B-Projekts eine FPGA-basierte digitale Phasenregelschleife (DPLL) für den Einsatz in einem Atominterferometer mit Raman-Doppelbeugung für eine Mikrogravitationsumgebung entwickelt und evaluiert.
Für Weltraumanwendungen ist ein digitales System sehr vorteilhaft, da die Parameter der Schleife ohne Löten und mit Kommunikation aus der Ferne eingestellt werden können. Außerdem ermöglicht der digital abstimmbare numerisch gesteuerte Oszillator (NCO), der als Referenzoszillator in der DPLL implementiert ist, Frequenzsollwerte, die so hoch sind wie der Laserstrombereich der Hardware. Zusätzlich ermöglicht der digitale Phasen-Frequenzdetektor (PFD) der DPLL in Kombination mit der entwickelten Hardware Phasenfehler zwischen Referenz- und Lasertaktsignal bis zu $2\,\mathrm{GHz}$ auslesen, ohne Einsatz externer Frequenzteiler. Der Erfassungsbereich des Phasenlocks ist somit nur durch die verwendete Hardware begrenzt.
Im Rahmen dieser Arbeit wurde die DPLL sowohl an mehreren Lasersystemen als auch mit einem elektronischen spannungsgesteuerten Oszillator (VCO) erfolgreich getestet. Eine Charakterisierung des Phasenlocks wurde durch Auswertung der durchgeführten Messungen an verschiedenen Lasersystemaufbauten erreicht. Es wurde eine Phasenrauschunterdrückung auf etwa $-60\,{}^{dBc}/_{\mathrm{Hz}}$ für Frequenzen zwischen $100\,\mathrm{Hz}$ und $1\,\mathrm{MHz}$ um den Träger herum gemessen. Hochoptimierte optische PLLs erreichen eine Phasenrauschunterdrückung bis auf $-120\,{}^{dBc}/_{\mathrm{Hz}}$, steigern jedoch Größe, Kosten und Komplexität im Vergleich zur DPLL. Das Springen zwischen Frequenzsollwerten mit ECDLs zeigte, dass die DPLL in der Lage war, weite Frequenzsprünge bis zu $2\,\mathrm{GHz}$ in etwa $420\,\mu\mathrm{s}$ zu realisieren.
Schlussendlich konnte die DPLL Rabi-Oszillationen mit ^{87}Rb BEKs treiben und Strahlteiler- und Spiegelpulse für die Raman-Doppelbeugung mit einer Effizienz von bis zu $97\,\%$ angeregter Atome realisieren. Anschließend wurden die angepassten Lichtpulse für Interferometrie-Sequenzen verwendet, bei denen eine absichtliche Verkippung der Apparatur über den Besetzungsunterschied der Atomzustände gemessen wurde.
Insgesamt wurde für das einrichten der Regelschleife für verschiedene Lasersysteme eine Zeit von weniger als einem Tag benötigt und eine erfolgreiche Anpassung der DPLL-Parameter zur Erzielung eines phasengelockten Laser-Beat-Signals konnte innerhalb weniger Stunden erzielt werden.

Schlüsselwörter: **digitale Phasenregelschleife**, **Raman-Doppelbeugung**, **Mikrogravitation**

Περίληψη

Τα ατομικά συμβολόμετρα (atom interferometers) έχουν χρησιμοποιηθεί τόσο στη βασική έρευνα της φυσικής όσο και σε πρακτικές εφαρμογές λόγω της υψηλής τους ακρίβειας. Η βελτίωση τους αποτελεί ένα μεγάλο διαδεδομένο πεδίο έρευνας και η δημιουργία εξαιρετικά σταθεροποιημένων φωτεινών πεδίων είναι ζωτικής σημασίας για τη βελτίωση της ακρίβειας τους, γεγονός που θέτει απαιτήσεις που υπερβαίνουν την υλική κατάσταση της τεχνολογίας.
Ένα Bose-Einstein-Condensate (BEC) είναι ιδιαίτερα χρήσιμο λόγω της μεγάλης διάρκειας ζωής του, καθώς ενισχύει την ευαισθησία του συμβολόμετρου, π.χ. στην κλασική διάταξη Mach-Zehnder. Ο μεγαλύτερος χρόνος παραμονής, σε σύγκριση με θερμικά ατομικά σύνολα, επιτρέπει ακριβέστερες μετρήσεις της επιτάχυνσης μέσω της μέτρησης της κβαντομηχανικής φάσης στην έξοδο του συμβολόμετρου. Η δημιουργία τέτοιων BEC είναι μια πολύπλοκη διαδικασία που απαιτεί συνεκτικό, σταθεροποιημένο φως διαφορετικών μηκών κύματος. Επιπλέον, η μετακίνηση ενός συμβολόμετρου που χρησιμοποιεί BECs σε περιβάλλον μικροβαρύτητας επιτρέπει μικρότερες συσκευές και μεγαλύτερες ακολουθίες. Ωστόσο, οι απαιτήσεις στην ακρίβεια για την ηλεκτρονική συσκεύη του συστήματως λέιζερ παραμένουν, ενώ το μέγεθος, το βάρος καθώς και η συνολική διαθέσιμη ενέργεια πρέπει να μειωθούν για διαστημικές συσκευές. Ένας τρόπος μέτρησης της κβαντομηχανικής φάσης της εξόδου ενός συμβολόμετρου είναι η Raman double diffraction. Για τον σκοπό αυτό αναπτύχθηκε και αξιολογήθηκε ένας ψηφιακός βρόχος κλειδώματος φάσης (DPLL) βασισμένος σε ενα FPGA μικροτσίπ για τη χρήση του σε ένα ατομικό συμβολόμετρο με Raman double diffraction που προορίζεται για περιβάλλον μικροβαρύτητας στα πλαίσια του προγράμματος του ερευνητικού πυραύλου MAIUS-B.
Για διαστημικές εφαρμογές ένα ψηφιακό σύστημα είναι πολύ ευνοϊκό, καθώς οι παράμετροι του βρόχου μπορούν να ρυθμιστούν χωρίς συγκόλληση και με επικοινωνία από απόσταση. Ο ψηφιακός ταλαντωτής (NCO), που υλοποιείται ως αναφορά, επιτρέπει τη ρύθμιση σημείων συχνότητας τόσο υψηλών όσο το εύρος του ρεύματος λέιζερ της ηλεκτονικής συσκευής. Επιπλέον, ο ψηφιακός ανιχνευτής φάσης (PFD) του DPLL μπορεί να διαβάσει σφάλματα φάσης μεταξύ των σημάτων αναφοράς και των σημάτων του λέιζερ έως και 2 GHz σε συνδυασμό με την συσκευή που αναπτύχθηκε. Ως εκ τούτου, το εύρος σύλληψης του DPLL περιορίζεται μόνο από την συσκευή.
Κατά τη διάρκεια αυτής της διατριβής, το DPLL δοκιμάστηκε με επιτυχία σε πολλαπλά συστήματα λέιζερ καθώς και σε έναν ηλεκτρονικό ταλαντωτή VCO. Ο χαρακτηρισμός του DPLL επιτεύχθηκε μέσω της αξιολόγησης των μετρήσεων που πραγματοποιήθηκαν σε διαφορετικές διατάξεις συστημάτων λέιζερ. Η μείωση του θορύβου φάσης μετρήθηκε σε περίπου $-60\,^{dBc}/_{\mathrm{Hz}}$ για συχνότητες μεταξύ 100 Hz και 1 MHz γύρω απο την τιμή αναφοράς. Εξαιρετικά βελτιστοποιημένα οπτικά PLL επιτυγχάνουν απόρριψη θορύβου φάσης έως και $-120\,^{dBc}/_{\mathrm{Hz}}$, αλλά αυξάνουν το μέγεθος, το κόστος και την πολυπλοκότητα σε σύγκριση με το DPLL. Οι μετρήσεις άλματος μεταξύ των σημείων ρύθμισης της συχνότητας έδειξαν ότι το DPLL ήταν σε θέση να πραγματοποιήσει μακριά άλματα έως και 2 GHz σε περίπου 420 μs. Τελικά, το DPLL κατάφερε να εκτελέσει Rabi oscillations με ατομική συνολή του ισότοπο του Ρουβίδιου (^{87}Rb) στην ατομική κατάσταση BEC και να πραγματοποιήσει παλμούς διαχωρισμού δέσμης και καθρέφτη που προορίζονται για Raman double diffraction με αποδοτικότητα έως και 97 %. Οι φωτεινοί παλμοί χρησιμοποιήθηκαν στη συνέχεια για ακολουθίες συμβολόμετρου που μετρούσαν μια σκόπιμη κλίση της συσκευής λόγω της διαφορετικής κατάληψης των ατομικών καταστάσεων. Συνολικά, ο χρόνος εγκατάστασης της συσκευής επιτεύχθηκε μέσα σε μία ημέρα για διαφορετικά συστήματα λέιζερ και η προσαρμογή των παραμέτρων του DPLL για την επίτευξη σταθεροποιημένου σήματος λέιζερ επιτεύχθηκε μέσα σε λίγες ώρες.

Βασικές λέξεις: **digital phase-locked-loop**, **Raman double diffraction**, μικροβαρύτητα

Contents

List of Figures

CHAPTER 1

Introduction

Atom interferometers (AIs) have become a vital tool in various areas of scientific research over the last decades. By measuring the acceleration that acted on an atomic ensemble, AIs can be used in earth science exploration, navigation and fundamental research [6].
For fundamental research, AIs are of special interest since they utilize the quantum nature of solid particles and can thus be an alternative for classical acceleration sensors.

1.1 Atom interferometers

In the most simplistic description of an atom interferometer, the atomic ensemble at the input of the interferometer is considered a two-level quantum system ($|1\rangle, |2\rangle$). Depending on the executed scheme, this two-level quantum system can experience Rabi oscillations after interaction with a resonant light field. Assuming a quantum degenerate gas at rest, the atomic ensemble can become a three-level quantum system ($|1\rangle, \pm|2\rangle$), where a resonant light field will split the ensemble between the two momentum states $-|2\rangle, -|2\rangle$ by two counter propagating light fields, which is called double diffraction [7]. A typical interferometer geometry is the Mach-Zehnder interferometer (MZI) setup which is illustrated in figure 1.1 for a double diffraction setup. For AIs atomic ensembles with low expansion velocities are needed and quantum degenerated gasses are preferred.

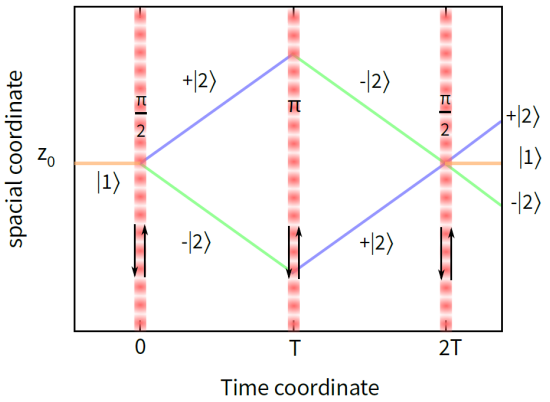

Figure 1.1: Schematic picture of a matter wave Mach-Zehnder interferometer setup for an atomic ensemble initially at rest with a momentum state $|1\rangle$. The initial state (orange) is diffracted by a laser pulse at time $t = 0$ into two arms (blue and green) with separate momentum states $\pm|2\rangle$, mirrored at time $t = T$ and recombined at time $t = 2T$. From the difference in the probability of occupancy of the outgoing states one can obtain the relative phase $\delta\Phi$ [8].

Choosing the product of interference time and Rabi frequency to $\pi/2$ the atomic ensemble is split into a coherent superposition between two momentum states. After a free evolution time T the momentum states of the interferometer arms are inverted by a π-pulse. After the full free evolution time $2T$, the interferometer is closed by another $\pi/2$ pulse.
Through detection of the population difference of the output states, a quantum mechanical phase difference $\delta\Phi$ can be obtained [5]. The phase difference can be described as a function of the acceleration $\vec{a}$ that acted on the ensemble during the free evolution time alongside the phase Φ_{laser}, that the light fields introduced to the atomic cloud during the interferometry sequence. They are described through:

$$\delta\Phi = \Phi_{acc} + \Phi_{laser} \tag{1.1}$$

$$\Phi_{acc} = \vec{k}_{eff} \cdot \vec{a} \cdot T^2 \tag{1.2}$$

$$\Phi_{laser} = \Phi_1 + 2\Phi_2 + \Phi_3 \tag{1.3}$$

where $\Phi_{1,3}$ are the phases imprinted onto the atomic ensemble during the first and second $\pi/2$ pulses and Φ_2 the phase imprinted during the mirror pulse.
It is clear from equation 1.2, that the sensitivity of such an AI scales with $\vec{k}_{eff}$ and the square of the free evolution time T. The free evolution time is usually limited in a gravitational field by the size of the experimental chamber. An obvious way to increase the free evolution time is to move the experiment into a microgravity environment or build a large baseline apparatus [9, 10]. Microgravity can be provided by drop towers [11, 12], sounding rockets [5, 13, 14] or orbital platforms [15–17] where usually a way to an orbital platform requires previous successful tests in drop towers and sounding rockets. The International Space Station (ISS) [18], micro satellites and free fliers represent possible orbital platforms.
By minimizing the phase Φ_{laser} introduced by the light fields through equation 1.3, the influence of the acceleration phase can be enhanced and therefore the interferometers sensitivity. This can be achieved through optimization of the light fields [19] or interferometry techniques such as double diffraction, which results in the laser phase being canceled out of the equation for the total phase [20].

1.2 The universality of the free fall

AIs are utilized for many different applications. Examples are magnetic field sensors, gravitational wave detection, atomic clocks, rotation sensors and other measurements of accelerating forces [21–23]. One important application of atom interferometers in fundamental physics are tests of the universality of the free fall (UFF) which is also known as the Einstein Equivalence Principle (EEP) formulated by Einstein [24]. The UFF states the equivalence of gravitational and inertial mass. The principle can be tested by comparing the free fall trajectories of different test masses. Possible violations of this equivalence can be expressed by the Eötvös factor η:

$$\eta = 2\frac{|a_1 - a_2|}{|a_1 + a_2|}, \tag{1.4}$$

where a_1 and a_2 are the accelerations on the test masses.
Non-vanishing results for measurements of the Eötvös factor would mean a violation of the EEP. The search for EEP violations is an important fundamental research since different approaches for

the unification of relativity and quantum mechanics predict violations on different levels [25, 26]. Early measurements of the Eötvös factor have been performed by Loránd Eötvös using a simple torsion balance. Modern versions of this torsion balance measure the Eötvös factor to a precision of $\eta \leq 10^{-13}$ using beryllium and titanium test masses [27]. Similar orbit based experiments with classical test masses reach a precision of $\eta \leq 10^{-15}$ [28]. Another important measurement of η was performed with the Lunar-Laser-Ranging experiment, which compared the free fall of earth and moon and reached a precision of $\eta \leq 10^{-13}$ [29].
The Eötvös factor can also be tested using an atom interferometer with quantum mechanical test masses by performing two acceleration measurements with different atomic species and obtaining the Eötvös factor from the results. Tests of this kind are of special interest because a classical principle like the EEP can be tested using test objects associated with quantum mechanics.

1.3 Challenges in space applications

The "Quantengase unter Schwerelosigkeit (QUANTUS)" project was founded to research the development of sources for ultracold atoms and their application in atom interferometers for microgravity environments. The goal of this project was to demonstrate the operation of an atom interferometer in microgravity to enable future missions in earth's orbit.
Alongside QUANTUS, the "Materiewelleninterferometer unter Schwerelosigkeit (MAIUS)" project began with the intention of building an atom interferometer on a sounding rocket as the next step towards an orbital platform. Following the MAIUS project, the next planned successor of the MAIUS mission is the collaboration project "Bose-Einstein Condensate and Cold Atom Laboratory (BECCAL)" between "National Aeronautics and Space Administration (NASA)" and "Deutsches Zentrum für Luft und Raumfahrt (DLR)", which intends to realize an atom interferometer on the ISS.
Extending the free evolution time T by moving an atom interferometry apparatus into a microgravity environment is a challenging venture. Commercial electronics that can drive these apparatuses are not optimized towards size, weight and power, which is very limited on sounding rockets, micro satellites or other orbital platforms like the ISS as well as in ground based experiments in drop towers. Furthermore, the requirements regarding robustness towards vibration during transportation introduce an additional challenge alongside communication, which needs to be achieved from a distance. Therefore, these projects demand custom build electronics in order to be accomplished.
Accordingly, electronic components for missions in such environments were and are currently being developed within the "Laser unter Schwerelosigkeit (LASUS)" project to fulfill the requirements ground and space born apparatuses pose [30].

1.4 Laser systems for interferometry

Laser stabilized light in atom interferometers has very stringent requirements towards phase noise and stability. Depending on the interferometer and the used atomic transition, this can be realized by constructing an optical Phase Locked Loop (PLL) to lock one laser to a set frequency setpoint and improve its stability and natural linewidth through adjusting the control loop.
Due to space limitations inside the QUANTUS family projects, lasers are used for multiple purposes in order to reduce their amount within the apparatus. Jumps between multiple frequency setpoints are therefore an additional requirement towards the electronic component controlling the laser system. A conventional analog optical PLL cannot hold up to these requirements, since

the separate parts of analog and hybrid PLLs cannot provide a wide enough range to realize the frequency jumps whilst simultaneously upholding the requirements towards phase noise and frequency stability without the need of changing loop parameters through soldering. Furthermore, utilizing such an optical PLL consumes an enourmous amount of time and high expertize in the field of control theory. Therefore, within this thesis, an all-digital field programmable gate array (FPGA) based PLL for lasers was developed with the purpose of fulfilling the requirements, that atom interferometers in microgravity requests. Furthermore, the setup time for an interferometry laser system would be enhanced by being fully digital and the setup of the PLL for existing laser systems would be possible in a very short time frame. The digital phase locked loop (DPLL) will be tested on different laser systems to evaluate its performance, since an atom interferometer type experiment strongly relies on extremely narrow coherent light of different frequencies. Tests on atomic ensembles will also be carried out in order to evaluate the DPLL's performance during interferometry sequences.

1.5 Scope of the thesis

Alongside the technical aspects of the experiment, a brief review of the necessary physics for laser trapping and cooling followed by the physics of atom interferometry will be given in chapter 2 and 3 alongside its requirements to the experimental hardware. After an introduction into control theory for PLLs in chapter 4, the technical aspects of the laser stabilization of the electronic control system as well as the executed measurements with different laser systems and atomic ensembles are discussed in chapter 5 and 6. The results of the measurements, comparison between the different laser systems and the performance of the developed system will also be given in chapter 6 followed by the overall conclusion and the proposed future development steps in chapter 7.

CHAPTER 2

Laser cooling and magnetic trapping

An AI's most valuable property is its high sensitivity towards accelerations. Therefore, a lot of research went into improving this aspect of the interferometer and one of the improvements is the usage of a Bose-Einstein-Condensate (BEC). A BEC is a state of matter, which is achieved by cooling down a gas of bosons close to absolute zero, leading to most of the atoms occupying the lowest energy state [31]. This leads to certain advantages. A BEC expands much slower than a thermal ensemble, leading to a higher free evolution time T in the interferometer sequence. Additionally, it can also be described by a single wave function instead of multiple wave functions, called wave function interference, leading to quantum mechanical effects being observable macroscopically. Detailed descriptions of the advantages of BECs in AIs can be found here [32–35].
Combining these advantages, one can create test masses with e.g. rubidium and potassium BECs, that can be described by two wave functions and expand very slowly [15–17]. This allows to elongate the free evolution time in the interferometer into the order of seconds and increases the measured acceleration phase Φ_{acc} that the atomic ensemble experience during the AI sequences according to equation 1.2.
The following chapters will shortly explain the steps of creating a ^{87}Rb BEC as it is performed in the QUANTUS family experiments [5, 13, 18, 32, 36–38]. Ultimately, the state preparation for the usage in an atom interferometer will be described in this chapter, alongside their requirements to the light fields.
Even though the main focus of this thesis is not the creation of BECs, the sequences set requirements to the laser system and are therefore necessary to be described shortly.

2.1 Cooling and trapping of neutral atoms

The magneto-optical trap (MOT) is an experimental configuration, which uses light and magnetic fields to simultaneously trap and cool neutral atoms [9, 39–41]. Although the targeted atomic species is electrically neutral, it can still be trapped by leveraging the Zeeman Effect [41]. This is achieved via coil pairs, creating a quadrupole field inside a vacuum chamber, which leads to the trapping of the atoms inside its minimum.
Thermal atoms have far above room temperature when evaporated into the vacuum chamber. Therefore, in order to trap as much atoms as possible their kinetic energy and thus their temperature must be reduced. The light fields of the MOT are utilized for reducing the mean kinetic energy $\langle E_{kin} \rangle$ through laser cooling, since the thermodynamic temperature is a function of $\langle E_{kin} \rangle$ and the Boltzmann constant k_B described by:

$$T_{temp} = \frac{2 \langle E_{kin} \rangle}{k_B} \tag{2.1}$$

In the following chapters, the MOT sequences will be explained.

2.1.1 2D-MOT

The 2-dimensional magneto-optical trap (2D-MOT) is a type of MOT and the first stage to trap and cool atoms in the QUANTUS experiment series. A possible setup configuration is illustrated in figure 2.1. Connected to this MOT are heatable alkaline reservoirs, called ovens in the following section, which contain rubidium and potassium at room temperature, although the focus will lie on ^{87}Rb. By heating these ovens, the metal evaporates into gases and diffuses into the vacuum chamber.

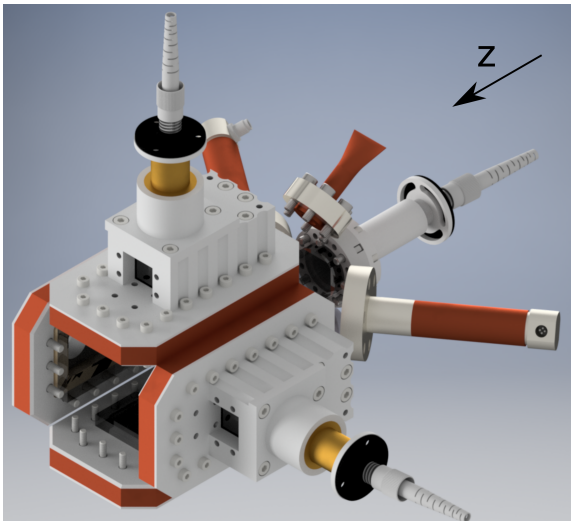

Figure 2.1: Illustration of the MAIUS-B 2D-MOT chamber. The coils are placed outside of the chamber in an Anti-Helmholtz configuration, generating a gradient magnetic field with a minimum in the center of the chamber along the z-axis. Laser beams are fed through two sides of the chamber and reflected at the opposite side in order to reduce the amount of beams, as well as two feedthroughs for pusher and retarder beams. Ovens with rubidium and potassium are connected at the corners of the chamber.

In order to trap these atoms in the chamber's center, two coil pairs with an Anti-Helmholtz configuration are mounted around the chamber. These coils generate a gradient magnetic field which can be calculated via the Biot-Savart-law (equation 2.2) and have a minimum in the chamber's center along the z-axis. This magnetic field splits the degenerate hyperfine states of the atoms into their magnetic angular momentum states. The energy states under the influence of an external magnetic field are shown in figure 2.2a and 2.2b.
Additional to the magnetic field, laser beams are fed into the 2D-MOT chamber through windows to realize laser cooling through their overlapping optical field [41]. This field consists of four counter propagating laser beams, which are red detuned to the transition frequencies of the atoms between the $|5^2S_{1/2}, F = 2\rangle = |g\rangle$ state and the $|5^2P_{3/2}, F' = 3\rangle = |e\rangle$ state, labeled the cooling transition of ^{87}Rb. The ground states $5^2S_{1/2}$ of ^{87}Rb are labeled with an F and the exited states $5^2P_{3/2}$ of the D_2 transition with an F'. They are illustrated in figure A.1 [1] in the appendix. The atoms in the chamber absorb photons and undergo the transition between ground $|g\rangle$ and excited state $|e\rangle$ whilst absorbing the photons energy and receiving its momentum (illustrated in figure 2.3a). Afterwards, the atoms emit a photon into a random direction and also get a random momentum according to Newton's third law, but as the direction is random, the average momentum due to the spontaneous emission is zero (illustrated in figure 2.3b). Effectively, the atom only absorbs momentum in the direction of the light field.

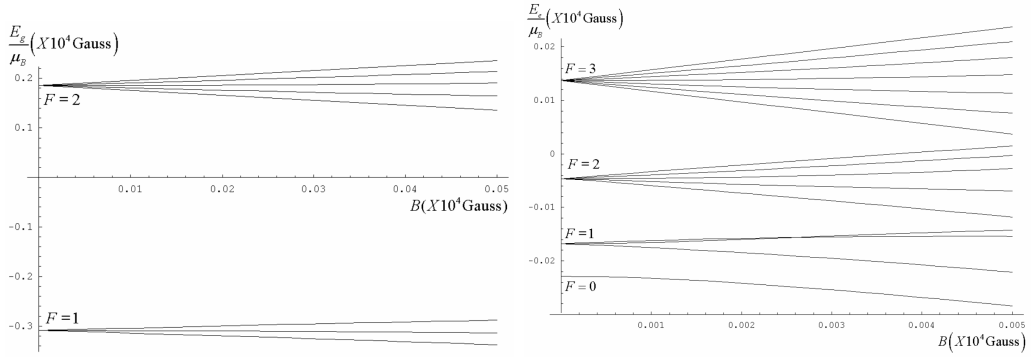

(a) (b)

Figure 2.2: Illustration of the hyperfine structure of $^{87}\mathrm{Rb}$ under the influence of an applied magnetic field for the ground states (figure 2.2a) and excited states (figure 2.2b). The Zeeman splitting of the hyperfine structure depends on the magnitude of the magnetic field [1].

Since there is a non-zero probability, that the atoms are transferred to the $|F' = 2\rangle$ and conduct a transition to the $|F = 1\rangle$ state, an additional light field is added to transfer the atoms from $|F = 1\rangle \rightarrow |F' = 2\rangle$, called repumper. From there, they reenter the cooling cycle by spontaneous emission from $|F' = 2\rangle \rightarrow |F = 2\rangle$.
In order to use this effect for cooling purposes, the absorbed photon needs to give the atom a momentum in the opposite direction it moves to. This is realized by detuning the laser light to a slightly lower frequency than the desired atomic transition. This method uses the Doppler-Effect to its advantage, which changes the frequency observed by the atoms, depending on the direction of their respective movement [42]. Therefore, atoms which have a momentum opposite to the laser light see a higher frequency of the photon and atoms, which have the same momentum direction as the laser light, see a lower photon frequency. Accordingly, only counter propagating atoms are probable to absorb the photon and its momentum. This is called Doppler-cooling and is a common procedure to cool down atomic ensembles.

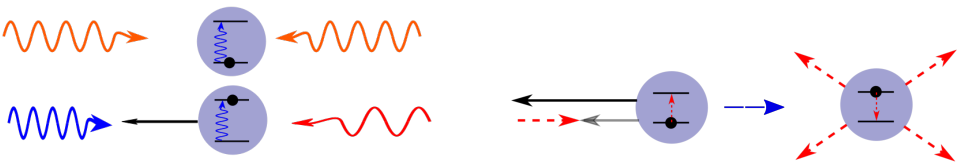

(a) (b)

Figure 2.3: Illustration of atoms in a one dimensional, counter propagating light field. Due to the red detuning of the light fields, the absorption of photons happens against the atoms direction, shown in 2.3a, leading to a reduced momentum of the atom, since the emission happens to a random direction, shown in 2.3b [2].

This cooling method considers a two-level atom regarding the energy state, which is a good approximation for ^{87}Rb due to the large energy splitting between the different F' states [41, 43]. The requirements towards the laser system are therefore set by the natural linewidth of the transition, which for the D_2 transitions is $\Gamma_c \approx 6\,\mathrm{MHz}$ [1]. The light fields should ideally be narrower

than $6\,\mathrm{MHz}$ for this experimental sequence in order to allow an accurate addressing of the atomic state.
Since the total momentum after the absorption and emission of the photon adds up in the opposite direction of the atom's movement, the atomic ensemble is effectively slowed down and cooled, since a lower average velocity means a cooler atomic ensemble.
The gradient of the quadrupole field results in an increase of the Zeeman splitting of the atomic transition. Therefore, the amount of absorbed photons increases when moving out of the magnetic minimum, resulting in a force which pushes the atoms towards the center of the MOT. Since this trap is two dimensional, the atoms are trapped along the z-axis in the chamber's center.

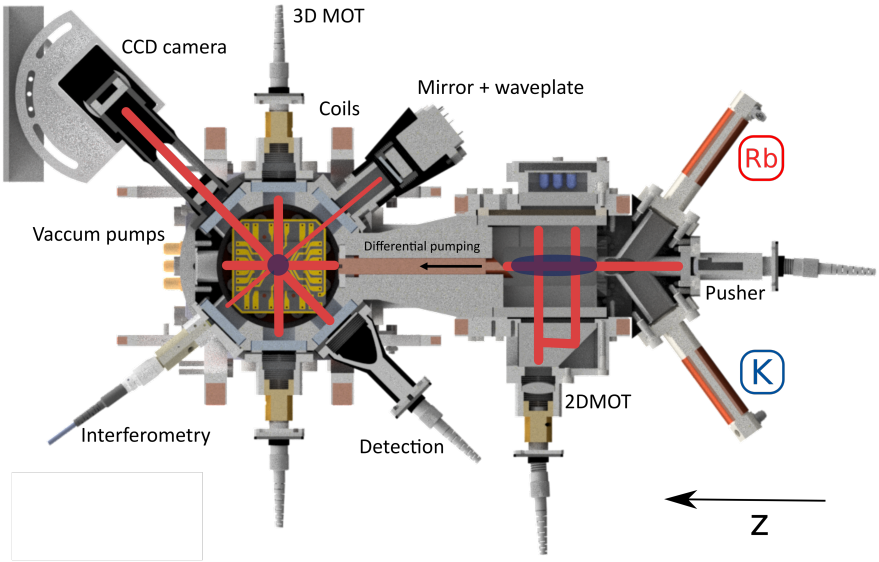

Figure 2.4: Illustration of the MAIUS-B 2D-MOT and 3D-chipMOT. Atoms in the 2D-MOT are trapped along the z-axis towards the 3D-MOT and pushed out via the pushing and retarding beam. Those two additional beams upgrade the regular 2D-MOT to a 2D+-MOT, leading to an additional cooling effect in the chamber [43].

The last step of the 2D-MOT is pushing the cooled atoms as an atomic beam into the interferometry chamber, where they will be trapped in a 3-dimensional chip magneto-optical trap (3D-chipMOT). Since the trap formed by the coils in the 2D-MOT is only two dimensional and the pressure in the two chambers differs due to vapor pressure originating from the ovens, the atoms constantly diffuse into the 3D-chipMOT due to the pressure difference. A chip MOT uses wires on a so called atom chip to generate a magnetic field by combining it with a field generated by coils, which will be described in the next section.
Often, the setup of the 2D-MOT is optimized and enhanced by additional beams called "pusher" and "retarder" beam (illustrated in figure 2.4), which leads to a cooler atomic beam and is further described under the title of 2D+-MOT by other researchers [8, 33, 44].

2.1.2 Magnetic trapping of neutral atoms

The Zeeman-Effect separates the degenerate states, which belong to certain angular momentum states m_F, when an external magnetic field is applied. They are separated by $\mu_B g_F \cdot B$, where μ_B is the Bohr magneton, g_F the Landé g-factor and B the absolute value of the external magnetic

field affecting the atoms [42].
The orbital angular momentum of a real atom couples to the total spin of the nucleus and the electron.

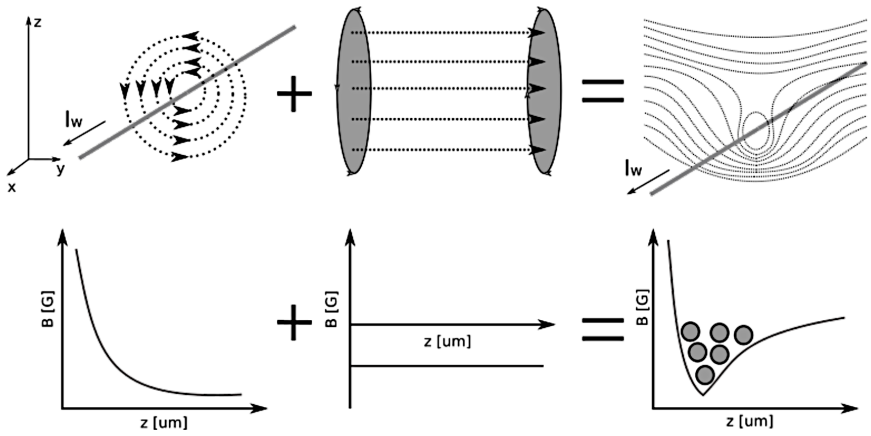

Figure 2.5: Setup of a wire combined with a coil pair to form a magnetic field trap. Combining the generated fields of a current flowing through a wire, shown on the LHS, and the constant mangnetic field created by a coil pair in an Anti-Helmholtz configuration, shown in the center row, leads to a magnetic field trap, illustrated on the RHS. The field strength in the graphs are in arbitrary units. Picture adopted from [38].

Thus by applying a constant magnetic quantization field, neutral atoms can be trapped by classical trapping methods. Atoms in a weak field seeking state can be trapped in a minimum of a local magnetic field. Such a minimum can for example be generated by a combination of current conducting wires on an atom chip coupled with a field generated by coils [45]. An easy example is the situation, where a field of one straight current conducting wire is overlaid with a field of just two coils, illustrated in figure 2.5. In this situation the field of the conducting wire combined with the field generated by the coils can be calculated by the Biot-Savart-law:

$$\vec{B}(\vec{r}) = \frac{\mu_0}{4\pi} \int_V \vec{j}(\vec{r'}) \times \frac{\vec{r} - \vec{r'}}{|\vec{r} - \vec{r'}|^3} dr' \tag{2.2}$$

where $\vec{j}$ is the current density through the conductor at the position $\vec{r}$ and $\vec{r'}$ is the vector at a given point in the area around the wire. V describes the volume over which the magnetic field is integrated. The constant μ_0 is the magnetic constant.
The modulus of the resulting magnetic field has a minimum along the wire axis forming a two-dimensional trap called a guide [46]. Closing the trap at the end of the trapping region could be achieved by bending the conducting wires.
The usage of a combination of coils and wires to form traps for neutral atoms is one of the basic components for a 3-dimensional chip magneto-optical trap (3D-chipMOT) in which the atoms are cooled using several different techniques. The wires in this chipMOT are implemented by an atom chip, which is used for other sequences along the way. Creating and optimizing magnetic fields is a well researched field and is explained in detail by other researchers [3, 45–47].

2.1.3 3D-chipMOT

The beam of cooled atoms from the 2D-MOT is collimated close to the surface of the atom chip of the 3-dimensional chip magneto-optical trap (3D-chipMOT). This trap operates in the same way as the 2D-MOT but in three dimensions. The 3D-chipMOT is a special type of 3D-MOT, that uses wires on a board to create magnetic fields as described in the previous section [48]. Figure 2.6a illustrates one example of a setup of the 3D-chipMOT with coils and an atom chip, realized for the MAIUS-B apparatus [33, 46].

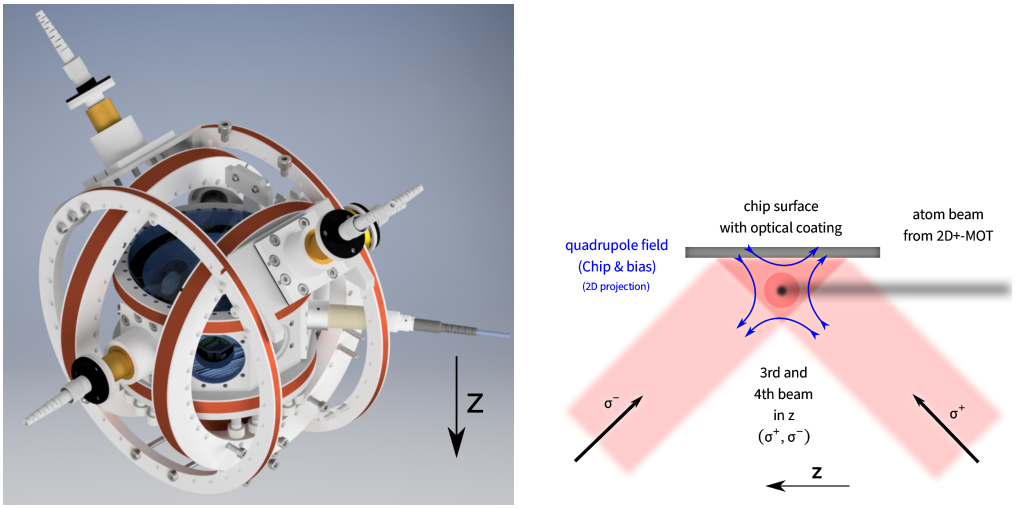

(a) (b)

Figure 2.6: Illustration of the MAIUS-B 3D-chipMOT. Figure 2.6a shows two coil pairs on the outside of the chamber together with the atom chip in the center create the magnetic field for trapping, the third is compensating disturbing fields from outside. The four laser beams are fed into the chamber in order to creating the overlapping light field in the minimum of the magnetic field. Figure 2.6b illustrates the schematic of an exemplary 3D-chipMOT with a reflective atom chip surface. Two beams hit the surface of the chip with opposite polarization σ^+, σ^-, providing the necessary light fields at the minimum of the magnetic field. The two remaining light beams, parallel to the atom chip surface, close the MOT and reduce the amount of beams from six to four compared to a conventional 3D-MOT [3].

Since a three dimensional MOT needs six laser beams (two for each spatial dimension) to achieve cooling and trapping of an atomic ensemble, the chip was coated with a mirror to reflect laser beams off of the surface leading to a reduced number of beams [48]. Figure 2.6b shows how the laser beams are reflected in the MOT close to the chip's surface.
The reason for using a setup with two different MOT chambers is the lifetime of the atomic ensemble. It is also possible to trap atoms from the background inside of the 3D chamber and set aside the 2D chamber completely, but there are multiple advantages of splitting the cooling and trapping process into two chambers. Since the atomic beam coming from the 2D-MOT is already cooled down, the time to reach the desired temperature in the interferometry chamber is decreased and the amount of trapped atoms is increased. Additionally, loading the MOT from a background gas of atoms would decrease the lifetime of the ensemble, since the vacuum pressure of the chamber would be higher due to the present gas in the background. Resulting collisions between the cooled ensemble and the background gas would be the reason for the reduced lifetime. Overall, splitting the MOT sequence into two chambers increases the lifetime of the cooled

ensemble tremendously compared to a standalone 3D-MOT setup [8]. This second sequence of cooling the atomic ensemble in the interferometry chamber reaches its minimum around a temperature in the mK regime.

2.1.4 C-MOT

The Compression magneto-optical trap (C-MOT) is an additional MOT sequence to further cool down the atomic ensemble and to decrease the trap volume in order to trap the ensemble in a purely magnetic trap later on [49]. It starts by moving the atomic ensemble closer to the chip by adjusting the magnetic fields. After moving the ensemble, the 2D-MOT is turned off, which decreases the average kinetic energy in the ensemble since no faster atoms are added anymore. The C-MOT works with the same cooling principles as the previous MOT sequences and reaches temperatures close to the cooling limit of a MOT, which is called the Doppler-Limit or Doppler-Temperature [2].

2.1.5 The Doppler limit

The Doppler-limit is the minimum temperature of an atomic ensemble, that can be reached in a MOT. It is reached when the heating and cooling process of absorbing and emitting a photon reach an equilibrium. The Doppler-temperature $T_{Doppler}$ of the ensemble can be calculated by

$$T_{Doppler} = \frac{\hbar\gamma}{2k_B} \tag{2.3}$$

with γ being the natural linewidth of the cooling transition. For ^{87}Rb this temperature is about $140\,\mu\mathrm{K}$ [1]. Since ^{87}Rb is not a two-level system, Sub-Doppler cooling effects are already present during the MOT sequences, leading to measured temperatures below the Doppler-Temperature. Sub-Doppler cooling will be the subject in the following sections.
With atomic ensembles at this temperature regime, a various number of experiments in atom physics were and continue to be performed [9, 50–53]. This thermal ensemble expands rather quickly. For the purpose of achieving long free evolution times T, as was mentioned in chapter 1, the atomic ensemble needs to have a very low expansion rate when releasing it from the trap. This can be achieved by further cooling the atomic ensemble, eventually reaching the phase transition to a Bose-Einstein-Condensate (BEC). The methods of achieving this phase transition will be explained in the next sections.

2.2 Phase transition into a BEC

Atoms can be cooled down beyond the fundamental Doppler-Limit with a MOT. In order to cool atoms even further down and reach the phase transition to a BEC, the ensemble can be cooled down further in an optical molasses [54, 55]. Molasses cooling falls into the category of Sub-Doppler cooling methods and can be achieved with different techniques, for example the Polarization-gradient-cooling [56], which will be explained shortly in the next section.
The requirements regarding the laser system during the following steps are still the natural linewidth of the D_2 transition mentioned before.
Although defining a temperature is not appropriate for atoms in the ground state (as they are in a BEC), where they have a momentum of $\vec{p} = 0 \rightarrow \langle E_{kin} \rangle = 0$ [41], it is nonetheless conveniently

used and will be used in the following sections.

2.2.1 Sub-Doppler cooling in an optical molasses

The Sub-Doppler cooling sequence starts by turning off all magnetic fields of the MOT, except for the compensation fields which shield the atomic ensemble from external electromagnetic noise. Considering that the optical fields still drive the state transitions of the atoms for cooling, the atoms still absorb and emit the photons of the light field. During this sequence, the atomic ensemble expands, since it is not trapped in a magnetic field minimum. Here, laser cooling is applied on the expanding atomic ensemble. By adding up the electric fields of two counter propagating light beams in σ^+/σ^--configuration, a polarization gradient is created in form of a helix (see figure 2.7). In this field, the degenerate states of the ensemble are split according to the AC-Stark shift [57].
The two counter propagating light fields create minima and maxima of σ^+/σ^- polarized light. By moving through the field, the atoms alternate between the AC-shifted light fields by absorbing and emitting photons, always seeking the state of the lowest energy. The energy lost by every occurring transition is the energy of the AC-Stark shift

$$\Delta E \approx \frac{\hbar\Omega^2}{4\delta} \tag{2.4}$$

with Ω being the Rabi frequency of the transition and δ the detuning of the light field.
Effectively, the atom's kinetic energy is carried away by the scattered light after the transition into the lower AC-Stark shifted energy levels. An example is shown in figure 2.7 for Polarization-gradient-cooling of ^{23}Na which is explained in detail here [58].

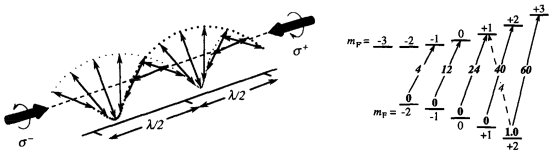

Figure 2.7: Illustration of the gradient field with σ^+, σ^- polarization used for Sub-Doppler cooling of ^{23}Na [58]. LHS: the σ^+, σ^- gradient creates a polarization gradient field in form of a helix. This leads to RHS: the population of the atomic species tends to transition to the most AC-Stark shifted sub states. Shown are the coupling strengths, relative AC-Stark shifts and steady-state populations of the various m_F sub-levels, adopted from [58] for the $F = 2 \rightarrow F' = 3$ transition.

The light fields are red detuned towards the AC-Stark shifted transitions. During this sequence the fields' detuning is increased whilst their power is reduced. By increasing the red detuning, only the faster atoms in the ensemble interact with the light field and the reduction of power reduces the probability to re-excite atoms.
This sequence is limited by the fundamental temperature limit of Sub-Doppler cooling which is the recoil energy transferred to an atom by the momentum of a single cooling light photon with a wavelength of λ. The recoil temperature T_r can be calculated by:

$$T_r = \frac{h^2}{k_B M \lambda^2} \tag{2.5}$$

with h being Plank's constant, M the atomic mass and k_B the Boltzmann constant. For $^{87}\mathrm{Rb}$, the recoil temperature is about $T_r \approx 360\,\mathrm{nK}$ [57].
During this sequence the ensemble expands while being cooled. To minimize the expansion with an optimal cooling efficiency, the molasses sequence needs to have a well defined duration. Also due to photons being scattered on the atom chip surface [3], the recoil limit cannot be reached in practice and the temperature after this cooling step is usually in the low $\mu\mathrm{K}$ regime.

2.2.2 Optical pumping and evaporative cooling

After optical molasses cooling, the atomic ensemble has been cooled down significantly, though in order to transition into a BEC, it still needs to be cooled down further. This is achieved by removing the fastest atoms from the ensemble via evaporative cooling in a magnetic field, after all atoms are transferred into the $|F = 2, m_F = +2\rangle$ state by optical pumping. With this technique, the atomic ensemble can reach a temperature in the area of a few nK and transition into a BEC [14].

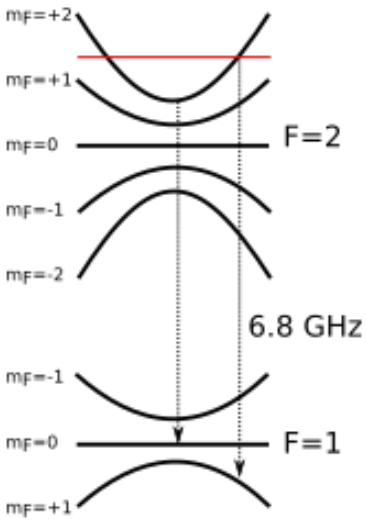

Figure 2.8: Illustration of the level diagram for ^{87}Rb microwave evaporation. The plot shows the hyperfine structure of the $|F = 1, 2\rangle$ states in a magnetic trap and the applied evaporation frequencies.

The energy state of the atoms, once the molasses cooling sequence is completed, is random across all angular momentum states in the ground state $|F = 2\rangle$. Since the evaporative cooling method needs to have all atoms in a magnetically trappable state, the atoms need to be transferred beforehand. A transition to the $|F = 2, m_F = +2\rangle$ state can be guaranteed according to transition rules by using σ^+ polarized light from a single laser to create a quantization field resonant to the $F' = 2$ transition.
By applying this light field, the ensemble is transferred into the $F = 2, m_F = +2$. This sequence is called optical pumping [59].
Like all sequences which were described above, this sequence also has a calculated duration, that was optimized in multiple experiments referring to probabilities of the D_2 transition [1].
Applying an external magnetic field after turning of the light field will split the degenerate $|F = 2\rangle$ states into their $|m_F\rangle$ hyperfine structure and they will arrange themselves higher or lower depending on their kinetic energy. Atoms in this state are trappable in a purely magnetic trap, but the atoms in the $|F = 1, m_F = 0, +1\rangle$ and $|F = 2, m_F = 0, -1, -2\rangle$ states are not (illustrated in figure 2.8), which can be used to remove atoms from the magnetic trap. Therefore by transferring the faster atoms into the $|F = 1\rangle$ states, the atomic ensemble effectively cools down, since the faster atoms are removed from the ensemble. The transition to these states can be achieved by transferring the atoms directly by applying RF fields in the MHz regime to achieve the transition to the $|F = 2, m_F = 0, -1, -2\rangle$ states or by applying a microwave field to achieve the transition to the $|F = 1, m_F = 0, +1\rangle$ states. This procedure is called evaporative cooling [60] and uses microwave frequencies from $f_{start} \approx 6.89\,\mathrm{GHz}$ down to $f_{stop} \approx 6.84\,\mathrm{GHz}$, to transition atoms into the not magnetically trappable states step by step [11].
The atomic ensemble during this cooling process reaches the phase transition to a Bose-Einstein-Condensate (BEC) [61, 62] which can be observed by measuring the phase space density of the

atomic ensemble shown in figure 2.9.

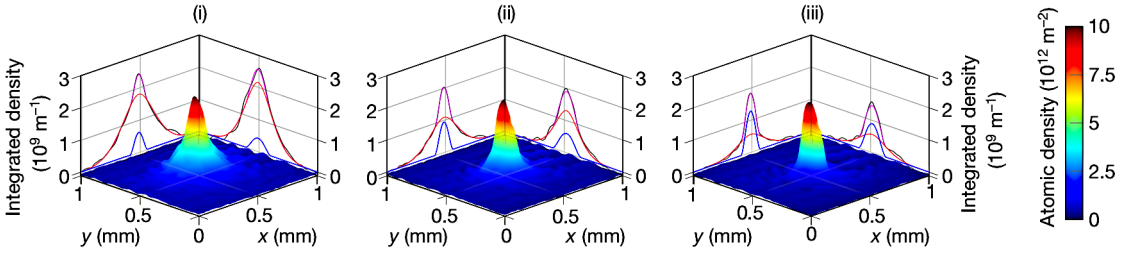

Figure 2.9: Illustration of the phase transition of an atomic ensemble during Bose-Einstein condensation. The blue curve in the background represents the amount of condensed atoms and the red curve the amount of thermal atoms. The violet line illustrates the total amount of atoms. The phase space density increases during evaporation until the point of condensation [37] but the total amount of atoms is reduced during evaporative cooling. From left to right, the percentage of condensed atoms are $8\,\%$, $20\,\%$ and $41\,\%$.

2.3 State preparation for atom interferometry

Succeeding the phase transition to a BEC, the atomic ensemble needs to be transferred to an internal state, which is best suited for the measured acceleration. For measurements of inertial forces, the preferred state is the magnetically insensitive $|m_F = 0\rangle$ state. The state transfer is explained in the following sections as well as an additional cooling method called Delta kick collimation (DKC).

2.3.1 Trap transfer and release

After being brought to quantum degeneracy, the atomic ensemble is in the $|F = 2, m_F = +2\rangle$ state and relatively close to the atom chip (about $\approx 200\mu m$ [3]). Since the center of the laser beam, which will be used for the interferometry sequences, is about $1\,\mathrm{mm}$ away from the chip's surface, the atomic ensemble must be moved further away. Furthermore, surface area effects with the chip would also disturb the experimental sequence which is also suppressed by increasing the distance to it [8].
The atoms are moved away from the chip by ramping down the current of the bias field responsible for reaching the desired room position. Simultaneously, the current going through the atom chip must be adjusted, so that the trap does not deform during the transfer process, which would lead to losses of atoms. The optimal timing and ramping of the currents, such that the loss of atoms during this step is minimal has been simulated and shown in detail by other researchers [3, 63].
After the BEC reaches the desired destination, the magnetic trap is turned off and the ensemble starts to expand in volume with a certain expansion velocity according to its temperature.

2.3.2 Delta kick collimation (DKC)

In order to increase the sensitivity of an atom interferometer, the expansion velocity of the ensemble should be minimized in order to achieve a long free evolution time T [64]. Since the

velocity is already quite low compared to thermal ensembles, BECs are very beneficial for such measurements from the get-go, but their properties can still be improved further.
Therefore, research to achieve even lower temperatures has been carried out [65, 66]. When looking at the momentum spread of the atoms after transferring and at the moment of release, the mean kinetic energy of the BEC would translate to a temperature of around $330\,\mathrm{nK}$ [68]. After turning off the magnetic fields, the atomic ensemble starts to expand and changes its shape. Looking at a simplified 1D space momentum picture, the momentum distribution transforms from a spherical to a cigar shaped distribution which is illustrated in figure 2.10 for the z-dimension. The reason for this deformation is, that the atoms move according to their momentum p_z towards their spatial dimension z and since the atoms with higher momentum move faster than the ones with lower momentum, the cigar shape is the result.

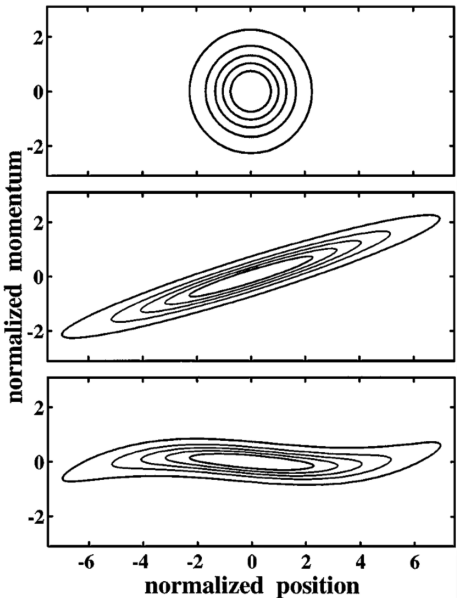

Figure 2.10: Illustration of the deformation of a BEC after releasing it from the magnetic trap. The figures illustrate the initial momentum (a), after a free evolution time (b) and after the delta kick (c) in the momentum space diagram [67].

By applying a precisely timed and shaped magnetic pulse, the momentum spread of the BEC is reduced noticeably and the mean kinetic energy of the atoms would translate into the pK regime [69, 70]. This technique of slowing down the expansion velocity is called Delta kick collimation (DKC) [67]. The sequence can be further optimized and results of $34\,\mathrm{pK}$ were recently achieved [12].

2.3.3 Adiabatic rapid passage (ARP)

The last preparation sequence prior to the AI sequences is the adiabatic rapid passage (ARP) [71] which is rapid in relation to the relaxation of the states and adiabatic enough so that the system can follow and a state transfer will be achieved [72]. After DKC the atoms are in the magnetically trappable $|m_F = +2\rangle$ state and therefore react sensitive to residual magnetic fields and are hence not well suited for precision measurements of inertial forces. In order to minimize the potential sources of outside noise, the ensemble has to be transferred into the first order magnetically insensitive state $|m_F = 0\rangle$.
Starting with a strong external magnetic field generated by the coils, the energy states are split into their hyperfine structure (shown in figure 2.2b).

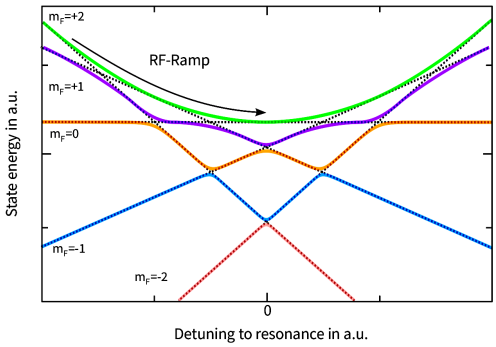

Figure 2.11: Illustration of the "dressed" states (colored lines) during ARP and the RF ramping (black arrow trajectory). Starting with a high detuning in the $|m_F = +2\rangle$ state, the detuning is ramped down to 0 during which the atoms transition into the $m_F = 0$ state [8].

Next up, a RF field is applied to the system, whose frequency is tuned down over the atomic resonances. This can be illustrated in the "dressed-state picture" [73] (figure 2.11), which shows the eigenenergies of the atomic ensemble dressed with the applied RF and magnetic fields [74].
These dressed states depend on the detuning Δ of the RF field with respect to the Zeeman energy splitting. Starting with a detuning in the $\Delta = 100\,\mathrm{kHz}$ regime, the RF field is being ramped down to $\Delta = 0$ whilst simultaneously adjusting the magnetic field strength accordingly.
This process is one method to transition the ensemble into the $|m_F = 0\rangle$ state [75], whilst another method would introduce an RF field to transition the atoms directly between their $|m_F\rangle$ sub states.
After the sequence is completed, the applied fields are turned off and the atomic states are projected to the "undressed" states, where the atomic ensemble stays in the $|m_F = 0\rangle$ state.
After turning off the external fields, the BEC is now in a preferred energetic state for inertial sensing and is cooled down far enough to have a long free evolution time in the order of s. The ensemble can now be used for precise atom interferometry.

2.4 Performance requirements

As previously mentioned, in order to allow an accurate addressing of the atomic states of the cooling transitions during the MOT sequences, the line width of the laser light should ideally be narrower than $\Gamma_c = 6\,\mathrm{MHz}$ for ^{87}Rb. An improved accuracy by a phaselocked laser can hence improve the cooling efficiency during the MOT sequences.
The hyperfine splitting of other atomic species, such as e.g. ^{41}K, are much closer together, which are in the range of a few MHz [5], in comparison to ^{87}Rb. Laser cooling of these species therefore has more stringent requirements to the light field frequency in order to address the atomic states accurately. A PLL can be necessary in this case, if the natural line width of the laser system is too broad.
Since space applications are limited in regards to size, weight and power, it is desirable to keep the amount of lasers as low as possible. Knowing the scattering rates and decay ratios of the F, F' states of the D_2 transition of ^{87}Rb, it is possible to realize Doppler cooling with one laser by jumping between the cooling and repumping transition. The frequency jumps of the laser need to be within the order of $\mu\mathrm{s}$ between the different frequency setpoints [76] in order to reduce the amount of lasers by one during the MOT sequences.

CHAPTER 3

Atom interferometry

Since the atom interferometer sets the requirements to the electronic system, this chapter will explain the experimental sequences during interferometry, specifically the ones, where the performance of the all-digital phaselock will be crucial.
This chapter starts with shortly explaining the fundamental principles of AIs, which find an application in many different fields of physics. Afterwards, a description of the Mach-Zehnder interferometer (MZI) configuration follows and an introduction to Rabi Oscillations, which are essential when describing and realizing interferometers with atoms. Here, the performance requirements to the DPLL will be exposed. Subsequently, the performance requirements will be explained in detail and summarized in the final section of the chapter including a description of phase noise and the resulting effects on the laser light.

3.1 Fundamental principles of atom interferometry

First of all, the basic idea behind an atom interferometer (AI) doesn't differ much from a regular interferometer with light, since according to de Broglie, atoms in movement have a wavelength as much as photons have momentum, which is stated by the matter-wave duality. Wavelength λ and momentum p of particles can be calculated by [77]:

$$\lambda = \frac{h}{p} \tag{3.1}$$

This means, that interferometry can be realized with atoms as well as with photons, for example in the traditional Mach-Zehnder interferometer setup [78] shown in figure 3.2 and explained later in section 3.1.1. The difference between interferometry with light and atom interferometry are the mirrors and beam splitters, which with photons are optical components and in AIs are timed light pulses driving atomic transitions. Depending on the probability of atoms being excited, the light pulses either work as beam splitters, where the atoms are in a superposition between ground and excited state, or mirrors, where the probability to find all atoms in the excited state is 1. Rabi oscillations describe the population probability between ground and excited state. These oscillations are displayed in figure 3.1 for different detunings and further explained in section 3.1.2.
An atom interferometer which uses cold atoms can work in different ways. It can directly manipulate a cold atomic ensemble [79], or utilize a moving molasses to launch the cloud and create an atomic fountain [80]. Alternatively, it can operate on a naturally falling cloud after it has been released. In all these cases, the ensembles of atoms lack coherence, meaning that individual atoms are independent of each other and their external wave functions are randomly phase shifted with respect to each other.
Similar to a light interferometer with a regular source, each atom in this scenario interferes with itself. The interference pattern is gradually constructed as atoms are processed one by one, through numerous trials. This process generates a signal that is proportional to the squared wave func-

tion, averaged over all unspecified experimental parameters, such as direction and momentum.

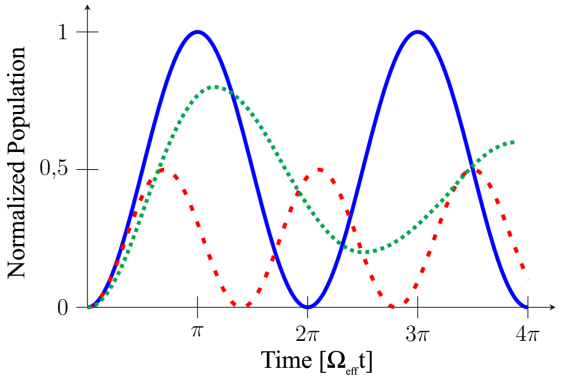

Figure 3.1: Illustration of different population probabilities depending on the effective Rabi frequency Ω_{eff} in a two level system as a function of pulse duration τ in time steps of $\Omega_{eff}\pi$. The frequency detuning towards the Rabi frequency Ω changes it to Ω_{eff} explained in section 3.1.2. With no detuning, the population probability to find an atom in the excited state is 50% after a time $\tau = \pi/2$ and 100% after $\tau = \pi$ (blue). For a detuning of $2\Omega_{eff}$, the probability changes to the red curve, which does not reach a population probability of 100% and is accelerated in regards to the blue line. A detuning, which increases with time leads to a damped Rabi oscillation, illustrated by the green line. Increasing the detuning as a function of time can occur e.g. due to spontaneous emission during the oscillation [81]. Another possible cause are shifting light fields, that drive the oscillation and therefore change Ω_{eff} with time.

A different situation occurs when using BECs, as done within the QUANTUS family. In BECs, the atoms all occupy the lowest energy state of the trap, resulting in a fully coherent condensate which would be the equivalent to a laser in light interferometry. By merging two initially separated condensates in a double trap, interferences have been directly observed, indicating a defined phase difference between them in this particular experiment. For more comprehensive and in-depth information about the functionality of AIs, there are numerous works available, including references provided here [82].
Taking into account these concepts of quantum mechanics, AIs can therefore be realized in the previously mentioned experiments of the QUANTUS family.

3.1.1 Mach-Zehnder interferometer

Mach-Zehnder interferometers are one of the standard setups and are usually the first reference when explaining atom interferometer (AI)s [78]. The setup is illustrated in figure 3.2 for the symmetrical and asymmetrical case. For the symmetrical MZI, both arms have the same free evolution time before and after the mirror, whereas the asymmetrical MZI adds a time difference to T.
Considering a Mach-Zehnder setup, the technical implementation of the beam splitters and mirrors depend on the manipulated particle. In case of photons, they are optical components made of glass, that are used in regular setups with lasers and other light sources. When dealing with electrons or other electrically charged particles, the beam splitters and mirrors are electric and magnetic fields, that split the particles' path in a similar way as the optical components [83, 84].

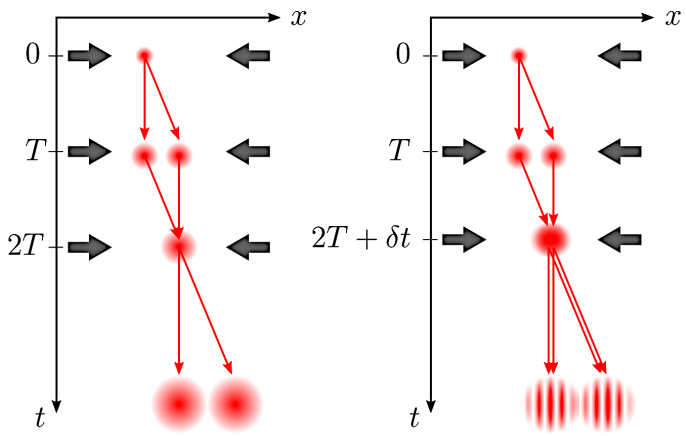

Figure 3.2: Illustration of the symmetrical and asymmetrical Mach-Zehnder setup for an atom interferometer. The interferometry sequence starts with a beam splitter pulse to split the ensemble into two states, after a time T a mirror pulse is applied in order to merge the ensembles again after a time $2T$. At this time, another beam splitter pulse is applied in (a) in order to achieve interference in the symmetrical setup. Here, the phase difference between the two arms decides the population of the two states. If an additional time difference δt is added, the interferometer becomes asymmetrical (b), where the phase difference between the two arms is visible in a constant phase shift of the fringe patterns between the output ports [14].

The Mach-Zehnder interferometer can also be realized with solid components using pseudo particles that describe for example the movement of momentum through a material. The beam splitters and mirrors are then realized through specific designed structures in the material such as microcavities or waveguides [85, 86].
For atomic ensembles, such as ^{87}Rb BECs, the beam splitters and mirrors are realized by light pulses with set frequencies and pulse duration. They drive a specific transition and lead to a certain momentum transfer which can be calculated through Rabi oscillations, since they are directly proportional to the interaction strength between laser light and the atomic cloud [87].

3.1.2 Rabi Oscillations

In the subsequent discussion about interferometry and Rabi Oscillations, the ground state $|g\rangle$ and the excited state $|e\rangle$ are a combination of the internal state and the external momentum of the ^{87}Rb atoms, and are defined as:

$$|g\rangle = |5^2S_{1/2}, F = 1, 2, m_F = 0, p_1\rangle \tag{3.2}$$
$$|e\rangle = |5^2S_{1/2}, F = 1, 2, m_F = 0, p_2\rangle \tag{3.3}$$

Depending on the initial state of the atom, the external momenta p_1, p_2 change to 0 for the initial state and $2\hbar|\vec{k}_{eff}|$ for the final state. The atoms are presumed to be in the magnetically insensitive state $m_F = 0$ for both employed hyperfine states, thus describing an atomic ensemble whose purpose is the usage in an interferometer for inertial sensing.

Rabi Oscillations are an important tool to understand the temporal evolution of the atomic state during the light pulses [88, 89]. The population probability $P_e(\delta, \tau)$ is a function of the Rabi frequency Ω for a one photon transition between two states. Ω depends on the natural line width

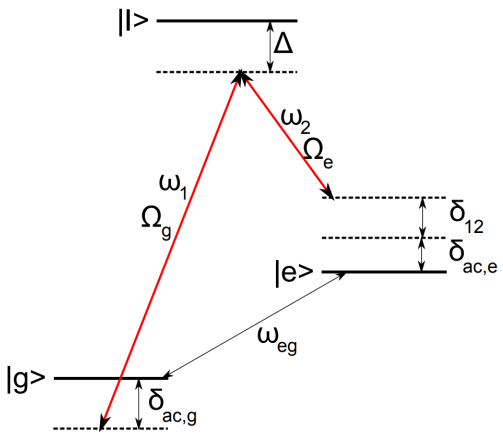

Figure 3.3: Illustration of a two photon transition between two states $|g\rangle$, $|e\rangle$ over an intermediate state $|i\rangle$.

Γ of the two states, the intensity of the light field I and the saturation intensity I_{Sat} [5, 34]:

$$\Omega = \Gamma\sqrt{\frac{I}{I_{Sat}}} \tag{3.4}$$

If the light field is detuned by a frequency δ to the resonance, Ω changes to the effective Rabi frequency Ω_{eff}:

$$\Omega_{eff} = \sqrt{|\Omega|^2 + \delta^2} \tag{3.5}$$

leading to a different population probability $P_e(\delta, \tau)$, which can be calculated by:

$$P(\delta, \tau) = \frac{1}{2}\left(\frac{\Omega}{\Omega_{eff}}\right)^2 (1 - cos(\Omega_{eff} \cdot \tau)) \tag{3.6}$$

with τ being the pulse duration of the light fields.
For inertial AI, a high momentum transfer during the interaction with the light fields is advantageous. Furthermore, it is necessary to use atomic transitions that have long-living states to prevent spontaneous decay from destroying coherence. Therefore, the $|F = 1\rangle \leftrightarrow |F = 2\rangle$ transition is chosen for Raman interferometry, since it is forbidden according to transition rules. Furthermore, the frequency difference between the hyperfine states is only $6.8\,\mathrm{GHz}$ and the resulting momentum by the absorption of the photon is only about $10^{-7} m/s$. Therefore, a two-photon transition is performed in order to increase the transferred momentum, illustrated in figure 3.3. The atomic ensemble is transferred in this three level system over an intermediate state $|i\rangle$ through absorption and stimulated emission of two photons. The atoms are then resonant to the two frequencies present in the light field and the effective Rabi frequency Ω_{eff} changes. It can be calculated through:

$$\Omega_{eff} = \frac{\Omega_g \cdot \Omega_e}{2\Delta} = \frac{\sqrt{I_1/I_{Sat} \cdot I_2/I_{Sat}}}{4\Delta\Gamma} \tag{3.7}$$

Here Ω_{eff} is a combination of the two Rabi frequencies Ω_g, Ω_e calculated for two one-photon transitions with equation 3.4. Δ represents the detuning of the intermediate state $|i\rangle$ to the next

excited state of the D_2 transition F'.
The total detuning δ between the light fields and the shifted transitions consists of multiple factors, which are illustrated in figure 3.3 and can be calculated with:

$$\delta = \delta_{12} - \delta_{ac} = (\omega_1 - \omega_2) - \omega_{eg} + \delta_{ac} - \delta_r - \delta_{Dop} \tag{3.8}$$

with δ_{ac} being the AC-Stark detuning, δ_{Dop} the Doppler detuning, ω_{eg} the frequency difference between the states in their hyperfine structure and ω_1, ω_2 as the frequencies of the light fields. δ_{12} is the detuning without the AC-Stark shift.
All these parameters depend on the performed atomic transition during interferometry, which will be subject of the next section.
The population probability $P_e(\delta, \tau)$ for the two photon process after a pulse duration τ can then be calculated. With a light pulse of a duration $\tau_{BS} = \pi/2 \cdot 1/\Omega$, one can realize beam splitter pulses and achieve a superposition of the atoms being in each state. Furthermore, light pulses with a duration of $\tau_M = \pi \cdot 1/\Omega$ diffract all atoms in the ensemble and are called mirror pulses [14].
Assuming a MZI setup as previously described, the sequences consist of:

- An initial $\pi/2$ pulse with a laser phase Φ_1
- a free evolution time T
- a mirror pulse π with a laser phase $2\Phi_2$
- a second free evolution time T
- and a final $\pi/2$ pulse to close the interferometer with a laser phase Φ_3.

These sequences can be described by matrices and a quantum mechanical wave function for the atomic state, which can been found here [4, 14, 52, 87]. The resulting probability of finding the atoms in the two states $|g\rangle$ $|e\rangle$ after the interferometry sequence P_{MZI} and without a detuning $\delta = 0$ is:

$$P_{MZI}(|g\rangle) = 1 - P_{MZI}(|e\rangle) = \frac{1}{2} - \frac{1}{2} sin(\delta\Phi) \tag{3.9}$$

with $\delta\Phi$ as the total collected phase during the sequence from equation 1.2 from chapter 1, which includes the laser phases $\delta\Phi_{1,2,3}$.
The beam splitter and mirror pulses can be realized in different ways. Either the Rabi oscillation occurs between two different internal states, e.g $|F = 1\rangle \leftrightarrow |i\rangle \leftrightarrow |F = 2\rangle$, or in between the same internal state, e.g. $|F = 1\rangle \leftrightarrow |i\rangle \leftrightarrow |F = 1\rangle$. If the atoms change their internal state, it is called Raman diffraction, if the oscillation occurs between the same state it is called Bragg diffraction.
Since Bragg diffraction does not need a phaselocked laser to achieve the transition, it won't be focused on further in this thesis. Nevertheless, Bragg transitions can occur during Raman transitions as losses, which needs to be taken into consideration. Therefore, a short introduction into Bragg diffraction is given in section A.2 in the appendix.

3.1.3 Raman diffraction

In Raman diffraction the atomic ensemble, besides changing its momentum state during the interferometry sequence, is also transferred into different internal state [90]. For an atomic ensemble

in the $|F = 2\rangle$ state, the two photon Raman transition occurs into the $|F = 1\rangle$ state via an intermediate state $|i\rangle$ close to the F' excited states. This changes the description of the states from equations 3.3 and 3.2 to:

$$|g\rangle = |F = 1, \hbar\vec{k}_{eff}\rangle \tag{3.10}$$
$$|e\rangle = |F = 2, 0\rangle \tag{3.11}$$

The resulting wave vector of this transition is:

$$\vec{k}_{eff} = \vec{k}_1 \pm \vec{k}_2 \tag{3.12}$$

Depending on the direction the photons of the transition are emitted and absorbed into, the effective wave vector $\vec{k}_{eff}$ is either the difference or the sum of the absorbed and the emitted photon. Since a high momentum transfer is favorable for inertial sensing, the light fields must be oriented in order to add both photon momenta to the atoms. This is achieved by counter propagating light fields that drive the transitions [52] and result in a transferred momentum during each Raman transition of $|\vec{k}_{eff}| \approx 2|\vec{k}_1| = 2|\vec{k}|$.
The photon absorption causes a detuning due to the Doppler shift δ_{Dop}:

$$\delta_{Dop} = \frac{\vec{p} \cdot \vec{k}_{eff}}{m} \tag{3.13}$$

with m as the atom's mass and $\vec{p} = m \cdot \vec{v}$ as the atom's momentum. The recoil shift δ_r also influences the detuning and is given by:

$$\delta_r = \frac{\hbar^2 |\vec{k}_{eff}|^2}{2m} \tag{3.14}$$

as well as the light fields themselves, which add an AC-Stark detuning $\delta_{ac,g}, \delta_{ac,e}$ towards both states, which can be calculated by [52]:

$$\delta_{ac,g} = \frac{|\Omega_g|^2}{4\Delta} + \frac{|\Omega_e|^2}{4(\Delta - \omega_{eg})} \tag{3.15}$$
$$\delta_{ac,e} = \frac{|\Omega_e|^2}{4\Delta} + \frac{|\Omega_g|^2}{4(\Delta + \omega_{eg})} \tag{3.16}$$

and results in a differential AC-Stark shift of [5]:

$$\delta_{ac} = \delta_{ac,e} - \delta_{ac,g} \tag{3.17}$$

Through calculations, the total detuning can be set to $\delta = 0$ for the Raman transitions and the probability to find the atoms in a state after the interferometry sequence can be calculated using equation 3.9. This is called Raman single diffraction [91, 92] and diffracts the atoms as illustrated in figure 3.4a.

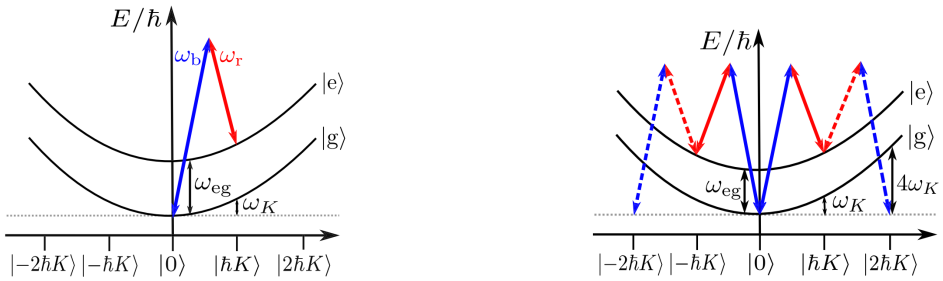

(a) (b)

Figure 3.4: Illustration of the atomic transition during Raman single and double diffraction in the energy-momentum diagram. For Raman diffraction, the initial and final energy state are different, so the Raman pulses change the energy as well as the momentum state of the atom. In case the initial momentum state is $|0\rangle$ (figure 3.4b), the transition can happen into two momentum states by counter propagating light fields. This is called Raman double diffraction. For Raman single diffraction (figure 3.4a), the initial momentum state can, but must not be non-zero e.g. $|+2\hbar k\rangle$ [4].

Another method arises when the atomic cloud with an initial momentum $|0\rangle$ is diffracted into two different momentum states $|\pm 2\hbar k\rangle$ simultaneously. A diffraction into two momentum states can be achieved by applying the light fields in two counter propagating directions, illustrated in figure 3.5.

This technique is called double diffraction [20, 93] (illustrated in figure 3.4b) and changes the previous calculations for the detuning.
Since the initial beam splitting pulse now has two momentum directions, the effective wave vector of the light pulse changes to:

$$|\vec{k}_{eff}| \approx 4|\vec{k}| \tag{3.18}$$

Initially, the total phase $\delta\Phi$ imprinted on the atomic ensemble during a MZI sequence consists of the acceleration phase Φ_{acc} and the laser phase Φ_{laser} described by equation 1.2 and 1.3 in chapter 1. The laser phase changes during double diffraction, since it is now imprinted on the atoms of both diffracted states. This leads to a resulting total laser phase of:

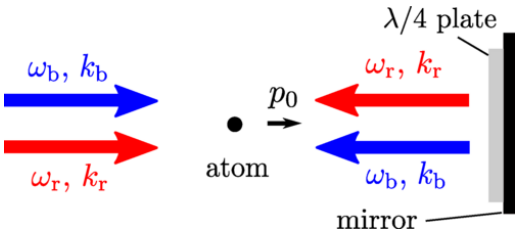

Figure 3.5: Setup of the light fields in order to realize Raman single and double diffraction. The setup is achieved with a $\lambda/4$ plate and a mirror. For single diffraction the atom engages in interaction with just one of the two counter propagating optical gratings due to the Doppler detuning of the other grating, depending on the initial momentum $|p_0\rangle$ of the atom. Each grating comprises two light fields with frequencies ω_b and ω_r, accompanied by wave numbers k_b and k_r, respectively. An initial momentum of $|p_0\rangle = |0\rangle$ in this setup would lead to the atom interacting with both counter propagating gratings, leading to a superposition of both excited states [4].

$$\Phi_{laser} = \Phi_1 - \Phi_1 + 2\Phi_2 - 2\Phi_2 + \Phi_3 - \Phi_3 = 0. \tag{3.19}$$

This is an important statement, since the measured quantum mechanical phase $\delta\Phi$ now only depends on the acceleration phase Φ_{acc}! This statement is true for this equation in the first order,

since in the second order of the equation, the run time of the light fields reintroduces the laser phase [20, 93].
Depending on which diffraction type is implemented, the requirements to the applied light fields change and challenge the laser system in different ways. They are described in section 3.2.

3.2 Performance requirements

Following the basic description of atom interferometry in the previous sections, this section will focus on the requirements AIs pose to the hardware and especially to the DPLL. Furthermore, laser phase noise is connected to frequency noise, which potentially influences the Rabi oscillation and must therefore be considered as well.

3.2.1 MOT and AI requirements

Starting with the MOT and cooling sequences in chapter 2, the requirements to the hardware are set by the limiting natural line width of the ^{87}Rb D_2 transitions.
The line width of the cooling $|F = 2\rangle \rightarrow |F' = 3\rangle$ and the repumping transition $|F = 1\rangle \rightarrow |F' = 2\rangle \rightarrow |F = 2\rangle$ should ideally be below $\Gamma = 6\,\mathrm{MHz}$.
Raman interferometry as performed in the QUANTUS family uses two light fields in order to achieve a two photon transition as previously described. The detuning δ for the Raman transition $|F = 2\rangle \rightarrow |i\rangle \rightarrow |F = 1\rangle$ as described in equation 3.8 depends on multiple factors and frequencies. These are presented in the following table [1]:

Table 3.1: Constants, assumed values and calculated values for Raman diffraction

Name	Constant	Value
Wavelength	λ	$780.241\,\mathrm{nm}$
atomic mass	m	$1.443 \cdot 10^{-25}\mathrm{kg}$
Plank's (reduced) constant	$\hbar$	$1.054 \cdot 10^{-34}\mathrm{Js}$
Raman transition frequencies	$\omega_{1,2}$	$384.230\,\mathrm{THz}$
Doppler Shift	δ_{Dop}	$15.0838\,\mathrm{kHz}$
Wave vector (D_2 transition)	$\lvert\vec{k}\rvert$	$2\pi/\lambda = 8.055 \cdot 10^6 1/m$
Recoil velocity	v_r	$5.885\,mm/\mathrm{s}$
Earth's gravitational acceleration	g	$9.81\,m/\mathrm{s}^2$
(one photon) Recoil shift	δ_r	$15.0838\,\mathrm{kHz}$
Name	Variable	Example
Detuning of $\lvert i\rangle$ to D_2 transition	Δ	$1\,\mathrm{GHz}$
Free evolution time	T	$1\,\mathrm{ms}$
Duration of Rabi pulses	$\tau_{BS,M}$	$100\,\mu\mathrm{s}$
Broadening of Rabi pulses	$\gamma(\tau_{BS,M})$	$1/2\pi\tau \approx 1.60\,\mathrm{kHz}$

The frequencies of the light fields ω_1, ω_2 for the transition depend on the detuning Δ of the intermediate state $|i\rangle$ to the $|F'\rangle$ states. The intermediate state is usually chosen to be very close to the F' states with a detuning around $\Delta \approx 1\,\mathrm{GHz}$ which leads to the light field frequencies being very close to each other and can therefore both be described by the wavelength $\lambda = 780\,\mathrm{nm}$, which translates to a frequency of $\omega_1, \omega_2 = 384\,\mathrm{THz}$. The recoil shift and Doppler shift, which are also part of the detuning δ, only depend on constants. Hence they can be calculated, as shown in

the table and compensated through adjusting the light fields. The AC-Stark shift δ_{ac} is a function of the detuning Δ of the intermediate state to the F' states, described through equations 3.15 and 3.16. The light field intensity and the saturated intensity I, I_{Sat} are influencing the AC-Stark detuning which can be calculated through equation 3.1. Since the light fields coupling to the energy states is a function of the detuning Δ, the frequencies $\omega_{1,2}$ and their light field intensities I_1, I_2, it can be compensated by adjusting the intensity proportion I_1/I_2 accordingly to achieve $\delta_{ac,g} = \delta_{ac,e}$ which is explained in detail here [94].
In comparison, the line width broadening of the Rabi pulse γ is a function of the pulse duration $\tau_{BS,M}$. These durations are variables and are changed in order to obtain the correct proportion between light field intensity and pulse duration for beam splitters and mirrors. The broadening of the Rabi pulse's line width sets the requirements for the phaselock's accuracy. For a duration of $\tau_{BS,M} = 100\,\mu\mathrm{s}$, the broadening is calculated to be $\gamma \approx 1.60\,\mathrm{kHz}$. It is anti proportional to the pulse duration, hence the longer the pulse the smaller γ becomes and increases the requirements to the phaselock.
In case of double diffraction, the imprinted laser phase becomes 0 as shown in equation 3.19. Therefore, the line width broadening γ sets the most stringent requirements to the laser system, by demanding the transition frequency of $|F = 2\rangle \rightarrow |F = 1\rangle$ to be:

$$\Delta\omega_{1,2} = 6.8347\,\mathrm{GHz} \pm \gamma \tag{3.20}$$

for an exemplary pulse length of $100\,\mu\mathrm{s}$. The relative accuracy of the DPLL must therefore be above $\approx 10^7$ for the Raman transition in order to effectively drive the Rabi oscillation without a damping due to losses in laser power or a shifting laser frequency.

3.2.2 Phase and frequency noise

A laser does in general not provide a frequency signal without noise (also called fluctuation or deviation), which is a result of many physical phenomena e.g. spontaneous emission of photons [95]. For a reasonably stabilized oscillator, such as a locked laser, the measured frequency as a function of time is assumed to deviate only slightly from the temporal mean frequency. The measured (or instantaneous) frequency $\omega(t)$ can then be defined as [95]:

$$\omega(t) = 2\pi\nu(t) = sin(2\pi\nu_0 t + \phi(t)) \tag{3.21}$$

with ν_0 as the carrier frequency of the oscillator and $\phi(t)$ as the noise of the phase as a function of time t. For simplification reasons, the phase noise is normalized ($x(t)$):

$$x(t) = \frac{\phi(t)}{2\pi\nu_0} \tag{3.22}$$

from which the frequency deviation $\Delta\nu(t)$ can be calculated with:

$$\Delta\nu(t) = \frac{dx(t) \cdot \nu_0}{dt}. \tag{3.23}$$

Phase and frequency noise of real oscillators contain power, which can be determined by integrating over the (one-sided) power spectral density $S_\nu(f)$ of the measured frequency spectrum in the Fourier domain. The power spectral density can be measured with a spectrum analyzer.
It can also be expressed by the phase noise spectral density $S_\phi(f)$, which is a function of the frequency power spectral density:

$$S_\nu(f) = f^2 \cdot S_\phi(f). \tag{3.24}$$

The total power of the frequency noise σ_ν can then be calculated with:

$$\sigma_\nu^2 = \int_0^\infty S_\nu(f) df. \tag{3.25}$$

In the laboratory, the total frequency noise's power cannot be determined over the whole spectrum between 0 and ∞, since that would require an infinite amount of time. Therefore, the bandwidth over which frequencies the spectral density is integrated is set to the relevant bandwidth (BW) around the ideal frequency between $f_1 \leftrightarrow f_2$. A noise spectral density $S(f)$ as a function of the frequency f is illustrated in figure 3.6.

When calculating the influence of noise, it can be categorized into different types, which can be reasonably well modeled by a superposition of five independent noise influences [96]. In a stabilized oscillator, of those five types of noise, two types are dominating in the frequency bandwidth which is of interest in this thesis. These are white noise and 1/f-noise, of which the latter becomes more dominant at low frequencies around the carrier peak. In order to calculate the total frequency noise from the spectral density $S_\nu(f)$, white noise behavior is assumed for the bandwidth $BW = f_2 - f_1$. Often in literature and datasheets, the frequency noise $\Delta\nu(f)$ is called root mean square (rms) noise $\Delta\nu_{rms}(f)$, since it is calculated by [97]:

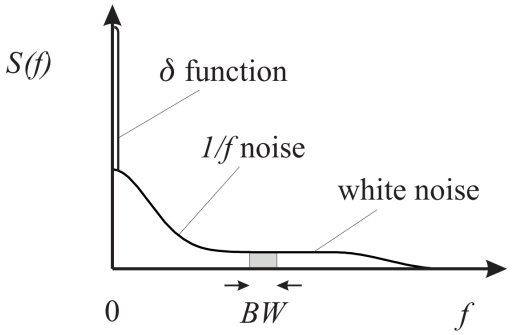

Figure 3.6: Illustration of the one-sided power spectral density as a function of the frequency f around the carrier of a stable oscillation (positioned at the δ peak). The different regimes of the power spectral density are dominated by different noise types, which change the calculation of the phase and frequency noise in equation 3.25 [95].

$$\Delta\nu_{rms}(f) = \sqrt{\int_{f_1}^{f_2} S_\nu(f) df}. \tag{3.26}$$

The rms noise can also be expressed as a function of the phase noise power spectral density $S_\phi(f)$ using equation 3.24, which is helpful when using a measurement tool called a phase noise analyzer. Another common value which is used in literature is the spectral purity $\mathcal{L}(f)$. It provides the same information as the rms phase noise, but differ in the unit of angle. The spectral purity is defined through [95]:

$$\mathcal{L}(f) = \frac{1}{2} S_\phi(f). \tag{3.27}$$

Choosing the frequency bandwidth to measure noise depends on the application. For the case that dividers are included in the path, the one-sided phase noise spectral density changes to [98]:

$$S_\phi = 20 \cdot log_{10}(N) + S_{\phi,div} \tag{3.28}$$

with $S_{\phi,div}$ being the one-sided phase noise spectral density after division and N being the total amount of divisions between $S_{\phi,div}$ and S_ϕ. For the rms noise, the addition of dividers does not change the calculated value, since it cancels out during the integration over the frequency bandwidth $BW = f_2 - f_1$ according to equation 3.26 [99].
Assuming a pulse duration of $\tau_{BS,M} = 100\,\mu\mathrm{s}$ for a Raman transition as previously described, the line width broadening of the pulse is around $\gamma = 1.60\,\mathrm{kHz}$, meaning the frequency span $f_1 \leftrightarrow f_2$ in which the noise is relevant is above $f_1 = 100\,\mathrm{Hz}$. For longer pulse durations $\tau_{BS,M}$, the relevant lower frequency border f_1 decreases. The contribution of noise, which is present above $1\,\mathrm{MHz}$ can be neglected, since PLLs use low pass filters, that reduce the noise contribution of frequencies above their control bandwidth drastically [100].
Finally, the noise measured in the Fourier domain needs to be converted back to the time domain in order to obtain the phase noise $\phi(t)$, which also goes by the name jitter or phase time [19, 98]. The jitter is obtained by inverting the Fourier transformation of the measured phase noise $\Delta\phi(f)$ with $\mathcal{F}(\Delta\phi(f)) = \Delta\phi(t)$ or with [95, 99]:

$$\Delta\phi(t) = \frac{\Delta\phi(f)}{2\pi\nu_0} \tag{3.29}$$

which provides the phase noise in a suitable unit when dealing with tolerances described in the time domain.
After accumulating the requirements, Raman single and double diffraction pose to the laser system, an approach to achieve these requirements has been demonstrated by other researchers before [19, 91, 98, 100]. The setup usually consists of two Raman lasers to achieve the two photon transition. The first Raman laser is frequency stabilized to a D_2 transition of ^{87}Rb through modulation transfer spectroscopy via a gas cell. The second Raman laser is locked by an optical PLL to the first Raman laser with a detuning of ω_{eg} to the first laser. These two lasers are then overlapped to create a frequency beat signal, which is fed into the phaselock feedback path by passing through a photo diode. The beat signal is then mixed or divided down to be processable by the electronics and mixed with a stabilized reference oscillator creating a phase error signal. This error signal is than fed into a loop filter which creates the control value for the second Raman laser's current and hereby closing the loop.
These setups are highly optimized to achieve a very low laser rms phase noise and consume an enormous amount of time to set up. However, they are not optimized regarding space, power consumption and weight, which is a limiting factor in space missions as mentioned in chapter 1. Additionally, the components utilized for these optical PLLs are usually analog, whose advantages and disadvantages will be described in chapter 4.
The all-digital PLL developed and studied in course of this thesis will be evaluated according to the requirements that Raman interferometry poses and in addition illustrates the advantages it poses by being a fully digital system, which accelerates the setup of the phaselocked laser drastically and is advantageous for space missions, since through its usage the amount of lasers can be reduced.

CHAPTER 4

The Phase Locked Loop (PLL)

A laser can be described as a controllable oscillator. In order to control the frequency and phase of such an oscillator, a Phase Locked Loop (PLL) can be used to control its phase and frequency by linking it to a reference oscillator. Through this connection, the controllable oscillator follows the reference. Adding a loop filter into the control loop, the phase noise and frequency drift of the controllable oscillator is reduced, which is necessary to achieve highly frequency stabilized laser light. Furthermore, through the addition of frequency dividers and multipliers more complex links between the controllable oscillator and the reference can be realized.
The most basic setup of such a PLL can therefore be realized with the following components:

- Phase detector
- Loop filter
- Controllable oscillator

The task of each component in the phaselock is rudimentary shown in figure 4.1 and will be further explained in chapter 4.2.

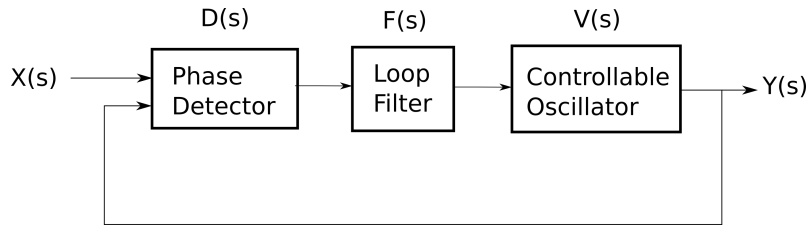

Figure 4.1: Illustration of a basic Phase Locked Loop (PLL) setup with its components described as transfer functions in the Laplace domain. $X(s)$ represents the input signal, $Y(s)$ the output signal and $D(s), F(s), V(s)$ the transfer functions of the individual components described by the complex frequency s.

This chapter starts with an introduction into the theory of phase locked loops, learning about the fundamental principals, how phaselocks work, which different parts of PLLs exist and what components they consist of. After understanding the basic principles of control theory, the developed code of the phaselock model for this thesis is presented and each component of it is explained separately. Consequently, the transfer function is determined in the Laplace domain and transformed into the discrete Z-domain for digital circuits. Hereby, the connection is obtained between the requirements towards phase noise and jumping speed which originate from laser cooling and atom interferometry and the adjustable loop coefficients for the loop filter by the user. Ultimately,

the DPLL's performance is estimated by simulating it with Altera's simulation programm ModelSIM®.

4.1 Phase Locked Loop (PLL) variants

Depending on the experimental setup, there are several types of PLLs available, each with advantages and disadvantages. They will be further explained in this chapter. Since every model has advantages and disadvantages, there is no universal choice of phaselock that works perfectly for every application.

Analog

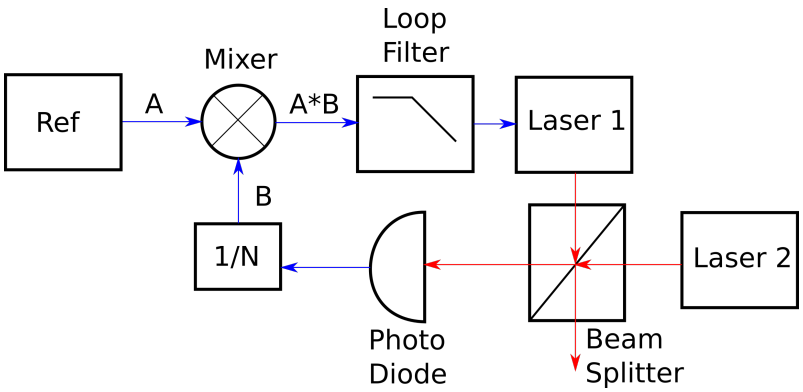

Figure 4.2: Illustration of an exemplary analog PLL. The phase detector is a mixer which combines the two input signals (the reference A and the feedback laser beat signal B) in order to obtain the beat signal $A \cdot B$ between them. The loop filter is a low pass filter that creates the control value for the VCO which in this example is one of the two lasers. The laser light of laser one is combined with the light of laser two (illustrated by the red arrows) in a beam splitter and focused onto a photo diode, creating the electrical feedback signal (illustrated through blue arrows) for the mixer. The divider (1/N) is an optional element.

The most basic and oldest PLL setup in experiments, whose requirements demand very high accuracy at a rather narrow frequency span (in the range of several $10\,\mathrm{MHz}$), are analog PLLs. Their theory is well known and there is a high variety of examples available on how the user can build his own hardware for their desired application [101, 102].
Assuming a setup for an optical phase locked loop in a Raman laser system, the components of the PLL consist of an analog mixer as a phase detector and a loop filter which gets the signal of a reference A and the beat signal B between laser one and laser two. The phase detector, which creates an error signal in the form of a frequency beat $A \cdot B$, is then fed into the loop filter, for example a PID filter. This creates a control signal, which can be fed back into the laser system to lock the laser to a certain frequency. A basic setup is illustrated in figure 4.2.
The signals A, B can be written as [103]:

$$A = U_1 \cdot cos(\omega t + \phi_1) \tag{4.1}$$

$$B = U_2 \cdot cos(\omega t + \phi_2) \tag{4.2}$$

which create a beat signal according to trigonometric function of the form:

$$A \cdot B = U_1 \cdot U_2 \cdot cos(\omega t + \phi_1) \cdot cos(\omega t + \phi_2) \tag{4.3}$$
$$= 1/2 \cdot U_1 \cdot U_2 \cdot (cos(2\omega t + \phi_1 + \phi_2) + cos(\phi_1 - \phi_2)). \tag{4.4}$$

Since the loop filter is in general a low-pass filter [101], the higher harmonic $cos(2\omega t + \phi_1 + \phi_2)$ is suppressed and only the phase error $cos(\phi_1 - \phi_2)$ remains. The loop filter uses this signal to create a control value for laser one, which changes its frequency accordingly. By optically mixing the beams from laser one and two, the feedback signal that goes into the phase detector is created, which closes the loop.
This setup works very well, if the focus of the desired phaselock lies on minimizing the phase noise of the feedback loop. The frequency range of the input is small [104] and related to the loop filter parameters, since mixer components tend to have small capture ranges.

Hybrid

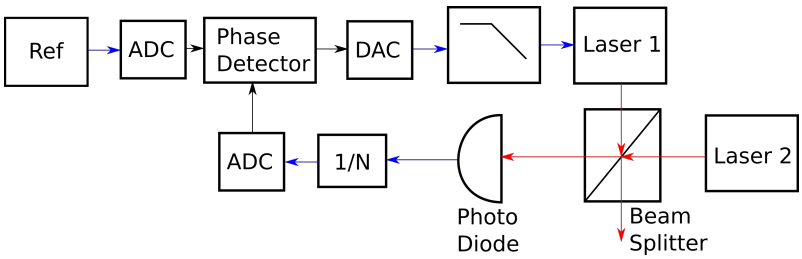

Figure 4.3: Illustration of an exemplary hybrid PLL. The phase detector receives a digital reference signal converted by an ADC and a digitalized feedback signal of the laser beat (digital signals are black arrows and analog signals are blue arrows) in order to obtain the phase error signal between them. The analog loop filer receives the error signal from the phase detector, which is converted to an analog signal beforehand by a DAC. The loop filter is a low pass filter that creates the control value for the controllable oscillator which in this example is one of the two lasers. The light of laser one is combined with the light of laser two (illustrated by the red arrows) in a beam splitter and focused onto a photo diode, creating the electrical feedback signal. The divider (1/N) is an optional element.

Analog frequency mixers are able to work with frequencies of over $1\,\mathrm{GHz}$, digital mixers can work with frequencies around $100\,\mathrm{MHz}$. Even though the analog mixer is superior when working with higher frequencies, the capture range of such mixers is limited. If the requested capture range is too high for an analog phase detector, the common way to increase the readout span of the input is to digitalize the phase detector and combine it with an analog loop filter [105, 106]. This gives the user a broader input bandwidth for frequencies, since the phase detector of a digital circuit has a higher capture range but the loop filter needs to be tuned through soldering.
A digital phase detector alongside the frequency mixer is the Phase Frequency Detector (PFD), which is further explained in chapter 4.5. The PFD surpasses the capture range of the mixer by far, since its only limited by the reference oscillator. An example of a hybrid PLL setup is shown in figure 4.3.

Fully digital

Lastly, if the user of the PLL wants a broad frequency band to work in without adjusting the loop filter through soldering or other analog methods, the suitable way to implementing a phaselock is by digitalizing it completely [107, 108].
A digital phase locked loop (DPLL) for laser systems is rarely realized [109, 110]. On the other hand they are frequently used to create frequencies in domains up to a few GHz and their applications extend to various domains where precise timing, synchronization, and frequency control are essential. Commercial applications for DPLL's are e.g. wireless communication systems, FM receivers and audio and video processing [111–113]. A Direct Digital Synthesizer (DDS) is another commercial example, which creates stable frequencies up to $1\ \mathrm{GHz}$ and consists solely of digital components including a Numeric Controlled Oscillator (NCO), which is part of a DPLL.
An example of a DPLL setup is illustrated in figure 4.4.

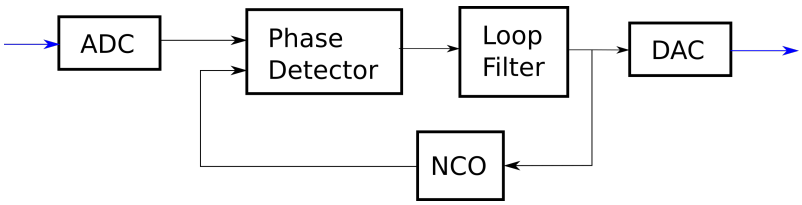

Figure 4.4: Illustration of an exemplary digital phase locked loop (DPLL) used as part of a receiver. The loop receives a digital reference signal converted by an ADC (digital signals are represented by black and analog signals by blue arrows). The phase detector receives the digitalized signal together with the feedback signal of the loop and outputs the phase error between them for the digital loop filter. The loop filter outputs a control value, which is fed into a digital controlled oscillator called a Numeric Controlled Oscillator (NCO). The NCO outputs a digital frequency signal, which is fed back to the phase detector. In order to receive the correct signal, the input frequency of the loop must be known and the NCO must be tuned accordingly so that the loop filter outputs the right value to the DAC.

DPLLs have the advantage that they can be adjusted for their specific usage very fast compared to analog and hybrid models. Their disadvantages lies in their discrete accuracy and resolution of the loop filter, which cannot compare to analog models that achieve continuous values as their control output of the filter.

4.2 Control theory

The usage of a PLL to control a frequency signal is a well researched field and has found usage in many different experiments and commercial applications. Thus, the control theory explained in the next chapter will be focused on the components the phaselock is build with and used later on after covering the basic principles of a DPLL.

4.2.1 Phase-Frequency detector

Phase detectors used in PLLs are usually one of two classes: multiplier (or mixer) and sequential phase detectors [102]. Multipliers, which are typically XOR-gates or similar two-input gates, generate their output as the average between the input signal waveform (the controllable signal) and the waveform of the local oscillator (the reference). The mixed signal, as displayed in equation

4.3 is called a beat signal. These phase detectors have no memory capabilities but have the advantage of being tolerant to noisy input signals.
Sequential phase detectors work with the time interval of the transition between the input signal and the local oscillator waveform which generates a very useful error output for loop filters. They also don't depend on other input parameters of the waveforms which simplifies the setup of a digital loop filter. In comparison, these phase detectors are more sensitive to noisy inputs than multipliers.
The chosen phase detector for the digital phaselock presented in this thesis was a Phase Frequency Detector (PFD), which is a sequential phase detector [114, 115]. It is widely used and therefore described and implemented by many different researchers as well as companies [116].

Setup and functionality

The most basic form of a PFD starts with two D flip-flops, an AND gate and a feedback connection to the D flip-flops. The schematic is shown in figure 4.5.

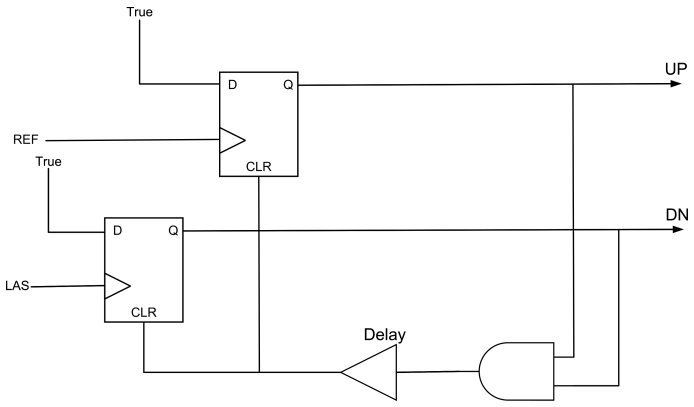

Figure 4.5: Illustration of a standard PFD setup with flip flops and an AND gate. The two input signals REF and LAS are processed into Up and Down signals, which show the phase relation between the inputs. The delay element is caused by the sampling time of the digital components, if the PFD is realized as code.

Starting with the input side, the PFD receives two signals

- the reference signal REF
- the controllable signal LAS (short for laser)

which are then fed into the clock terminals (CLK) of the flip-flops. The outputs of the flip-flops are:

- Up
- Down

and are both fed into the AND gate, which then gives out a signal to the asynchronous Clear terminals (CLR) of the flip-flops.
An example for a possible input signal for REF and LAS is given in figure 4.6a as well as their respective Up and Down output waveforms. Figure 4.6a shows a REF signal which is initially faster than the LAS signal, resulting in a positive output signal at the Up output. Further on, the REF

signal slows down and is at one point as fast as the LAS signal, resulting in a zero value output for Up and Down. Afterwards, the LAS signal surpasses the REF signal in speed and the Down signal has a positive output.
The output on the respective channels indicates the direction of a phase/frequency error signal that represents if the signal at the LAS input is either slower or faster than the REF signal. When both signals are outputting a non-zero value, the flip-flops are cleared to 0, since at that moment the inputs are in phase. The length of the generated signals indicates the magnitude, how far the two input signals are apart. An additional illustration is the state machine of the PFD, that shows the relation between positive input signals and the output values of the PFD. It is illustrated in figure 4.6b.
Nomenclature dictates, that since the information of the phase error lies in the output pulse width, this PFD model is an analog configuration to measure the phase between two signals.

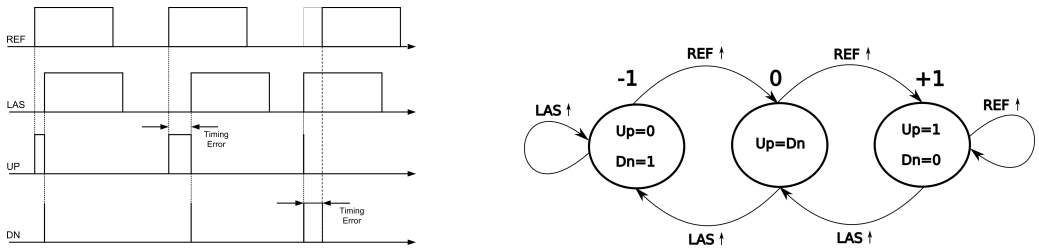

(a) (b)

Figure 4.6: Illustration of the different output forms of the Phase Frequency Detector (PFD) as signals (figure 4.6a) and in the state machine (figure 4.6b). Depending on the rising edges of the reference signal REF and VCO signal LAS, the output is positive for the Up output or the Down output. This information provides the relation of the phase difference between the two input signals.

Since this model can be easily implemented as code in DPLLs, one can argue if the nomenclature is too strict in this case, since this model can be both an analog component or digital code [102]. The effects of delay in the feedback to the Clear terminals set an upper limit to the input signals of the PFD.
In the Laplace domain, which is used in control theory to describe control circuits [117], the PFD can be described through its two input phases θ_r, θ_o and the phase error output θ_e, assuming a linear approximation close to its lock frequency, by:

$$\theta_e = \theta_r - \theta_o \tag{4.5}$$

It is considered a proportional element.

Phase and frequency noise performance

As mentioned before, PFDs are less sensitive to noise in the input lines, since they only see zero-crossings. Therefore, they don't see amplitude fluctuations which can be observed in the waveform figure 4.6a where the input waveforms are always normalized to 1 or 0 beforehand. In comparison, mixers see amplitude noise and their error value output will show the fluctuations which will be imprinted onto the output of the PLL.
Phase and frequency fluctuations on the other hand can be seen by the PFD to which mixers are less sensitive to [101]. Therefore, the phase noise of the reference oscillator input and the laser

input must be measured and taken into account. The capture range of the PFD is only limited by the hardware and even large frequency differences between the two input signals still produce a usable error output. A mixer in comparison performs poorly when the two signals have a large frequency difference but performs better when the two signals are almost locked. Since jumps between frequency setpoints will be performed with the DPLL, a PFD is more suitable for the use with a laser than the mixer.
Improvements to make the PFD less sensitive to phase and frequency fluctuations will be introduced in the description of the developed PLL model in chapter 4.3.

4.2.2 Loop filter

The next component is the loop filter, which receives a phase error signal from the PFD. There are two commonly known filter types: active and passive filters. Passive filters consist solely of passive components like resistors and capacitors. Since the introduction of operational amplifiers, active filters have taken over in PLLs and are widely used [102]. These filters are usually realized with analog components where high precision and low phase noise is required and examples for digital loop filters are uncommon. In this thesis, a proportional integral derivative (PID) filter was implemented in the digital control system [118].
A PID filter consists of three different components:

- the proportional gain P
- the integral gain I
- the derivative gain D

which use an error signal to create a control value. The sum of the three gains is the output for the controllable oscillator and will steer the phase error to 0 if not otherwise specified. Figure 4.7 displays a basic setup of an arbitrary PID filter with its parts consisting of analog components. This filter is set up with very rudimentary components, which are well researched in control theory [119].

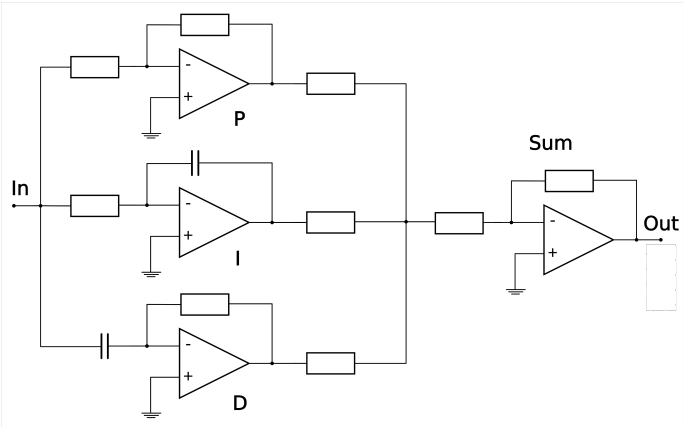

Figure 4.7: Illustration of the analog proportional integral derivative (PID) filter constellation. From top to bottom, the proportional gain P, the integral gain I and the derivative gain D are obtained through a circuit consisting of operational amplifiers, capacitors and resistors. The fourth circuit after the summation amplifies the sum of the signal.

Starting with the proportional gain P, the calculated control parameter solely depends on the difference between the demanded setpoint and the process variable which is the error signal from the PFD. Since the desired difference is an error value of 0, it solely depends on the error signal. The P response is calculated momentarily and doesn't take previous error values into account, hence the name proportional. An amplification factor K_P is added to adjust the control parameter and is multiplied with the calculated P response. The proportional response cannot achieve a phase error value of 0 and creates a control error, which needs to be compensated with one of the following gains [119].
Next in line is the integral gain I, which is calculated by adding up the error signal with time, called an accumulator. This leads to the control signal increasing rapidly in value, even if the error signal is small. It reaches a steady state when the inputted error signal stays at 0 and the calculation of the integral response therefore depends on the steady state error, since it takes previous error values into account. For this gain, another amplification factor K_I is introduced, which is multiplied with the calculated I response.
The derivative gain D calculates its control value based on the rate of change of the error signal. It is the fastest reacting part of the loop filter and can only be used in combination with the gains mentioned above, since it cannot create a control value to steer the error towards 0 but only reacts to the rate of change. Therefore it won't reach the setpoint by itself and has to be combined with a proportional or integral gain. The derivative response is also multiplied with an amplification factor K_D after calculation for adjustment purposes [101, 102, 117, 119].
The three separately calculated gain values are summed up after being multiplied by their respective amplification factors and then fed into the controllable oscillator. An additional amplification circuit for the sum of the gains, as shown in figure 4.7, is optional. This output value can be described by the differential equation of the PID filter in the time domain through:

$$u(t) = K_P \cdot e(t) + K_I \cdot \int_0^t e(\tau)\,dt + K_D \cdot \frac{d}{dt}e(t) \tag{4.6}$$

where $u(t)$ is the output value and $e(t)$ is the input error [117].
The process of obtaining the optimal amplification factors for the gains is called "tuning" and there are different approaches to achieve optimal tuning. The "trial and error" and the "Ziegler-Nichols" method will be explained shortly, since they are the most frequently used methods of tuning PID controllers [120].

Table 4.1: Factors for the calculation of P, I and D gains proposed by Ziegler and Nichols. T_i is the rise time and T_d is the derivative time needed to calculate the I and D gains. K_c is the critical gain for P and P_c is the oscillation period of the critical gain.

Control	K_P	T_i	T_d
P	$0.5 \cdot K_c$	–	–
PI	$0.45 \cdot K_c$	$P_c/1.2$	–
PID	$0.6 \cdot K_c$	$0.5 \cdot P_c$	$P_c/8$

In order to start the "trial and error" method, the I and D gains are set to 0 and the P gain is increased until the system starts to oscillate. Once oscillation is achieved and the system reacts to disturbances with the desired speed, the I gain is increased. By increasing the I gain, the oscillation is reduced but at the same time the overshoot increases, since the I gain adds up the previous

errors. The tuning of the I gain is set to achieve a minimal steady state error. Lastly the D gain is tuned by increasing it until the system reacts fast enough to changes in the error signal which can be tested by feeding noise signals into the loop.
The "Ziegler-Nichols" method starts in the same manner as the "trial and error" method by tuning the P gain until the system oscillates. In this state, the critical gain K_c and the period of oscillations P_c can be measured. Using these factors, the I and D gains are calculated as proposed by Ziegler and Nichols shown in table 4.1 [121].
In order to calculate the I and D gain from the integral time T_i and the derivative time T_d, the following equations can be used:

$$K_I = \frac{K_P}{T_i} \tag{4.7}$$

$$K_D = K_P \cdot T_d. \tag{4.8}$$

Through measuring K_c, P_c the differential equation of the PID loop filter can be adjusted to a specific system.

4.2.3 Reference oscillator

The reference oscillator creates the frequency reference the phaselock will lock the controllable oscillator onto.

Since the imperfections of the reference will be imprinted directly onto the control value, the demand to implement it with as much accuracy as possible is favorable.
The requirements to the reference oscillator can differ, depending on the system, and can usually not all be met simultaneously, but they need to be taken into account when determining the quality of the phaselock [102]. The requirements for the reference oscillator usually focus on:

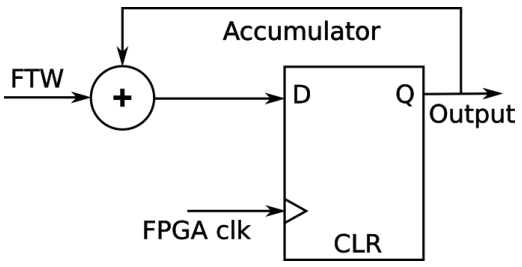

Figure 4.8: Schematic of the Numeric Controlled Oscillator (NCO) realized with a flip flop.

- frequency accuracy
- wideband frequency modulation
- wide tuning range
- low phase noise
- small size
- low power consumption
- integration on a chip.

The reference for a DPLL will be digital as well, which makes the last three requirements easily achieved.
A digital oscillator controlled with numbers is called a Numeric Controlled Oscillator (NCO) and

can be used for multiple purposes outside of a PLL. For example, the output of a NCO is a rectangular wave, but can be converted to a sine wave via a lookup table and generated through a digital analog converter (DAC). This creates an analog frequency signal which is controlled digitally and is called a Direct Digital Synthesizer (DDS) [122].
The NCO consists of a register, that accumulates a frequency tuning word (FTW) $u_c[n]$ at every clock cycle f_{clk} and adds it to a phase $e_0[n]$:

$$e_0[n] = e_0[n-1] + u_c[n-1]. \tag{4.9}$$

The frequency resolution of such an oscillator is $f_{clk}/2^b$ with the amount of bits b and it can output frequencies of up to $f_{clk}/2$ [102].
In this thesis, the NCO outputs the most significant bit (MSB) as soon as the accumulator overflows. The frequency of the generated signal is controlled by the frequency tuning word (FTW), which can be steered by the user. This signal is then fed into the PFD as the earlier mentioned REF signal (see chapter 4.2.1). A setup of the NCO with a flip flop is illustrated in figure 4.8.

4.2.4 Controllable oscillator

The controllable oscillator of a PLL, often called a Voltage Controlled Oscillator (VCO), is the part of the phaselock which is controlled by the output value of the PID filter and outputs the signal at the desired frequency. In order to have an active feedback loop, the signal is also fed back into the PFD to adjust the phase error signal θ_e continuously. Any sort of oscillator can be approximated as a VCO if it is possible to be controlled through a modulated voltage [103]. Therefore, lasers can also be approximated as a VCO, although they would technically be a current controlled oscillator.
The general transfer function of a VCO, assuming linear behavior, would be defined through its input control signal $v_c(t)$, its gain K_o and its phase output θ_o through:

$$\frac{\partial \theta_o}{\partial t} = K_o \cdot v_c(t) \tag{4.10}$$

Linear behavior can be assumed, when the oscillator is in lock or close to it [101]. The specific type of controllable oscillator is specified by the system it is used in, which will be described in chapter 6.

4.3 The developed PLL model

In this section of the thesis, the phaselock model, which was developed for the experiments and measurements in chapter 6, is explained. It is based on a basic PLL model described in the previous section and modified for the usage with a laser, whose current is steered via the generated control value. The DPLL is written in VHDL code and compiled by the Quartus® software from Altera for their FPGAs.
The setup of the standalone and fully digital phaselock model without the laser is shown in figure 4.9.

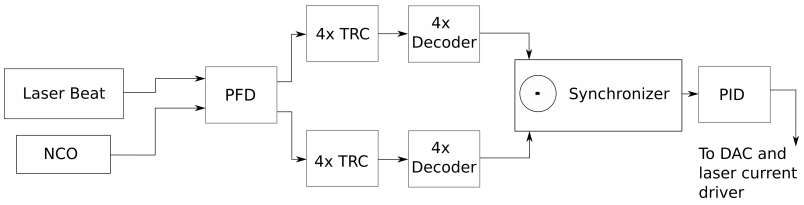

Figure 4.9: Illustration of the developed DPLL model with its individual components. It consists of the NCO which creates the reference frequency for the phaselock, the PFD which creates the error signal between laser beat and NCO represented through Up and Down signals. This signal is split up to 8 TRCs and decoders, running at the $300\,\mathrm{MHz}$ FPGA clock with different clock phases. The error signal is generated by a subtraction in the synchronizer, after the 8 signals from the decoder output are synchronized to the $100\,\mathrm{MHz}$ clock. This error value is then fed to the digital PID filter, creating the control value for the laser current driver by passing through a DAC.

The full VHDL code is attached to this thesis and shown in the appendix chapter A.3.

4.3.1 Numeric Controlled Oscillator (NCO)

Starting with the input side of the DPLL, the input setpoint is adjustable by the user through a frequency tuning word (FTW). This FTW needs to be translated into a reference oscillation for the PFD which is realized through a Numeric Controlled Oscillator (NCO) that creates a digital oscillation as previously explained in chapter 4.2.3.
The Nyquist limit sets a frequency limit at half the clock of the FPGA, which for the Intel® MAX10 FPGA series is $f_{Ny} = 1/2 f_{FPGA} \approx 150\,\mathrm{MHz}$. The FTW length is also limited to a $b_{FTW} = 32\,\mathrm{bit}$ setpoint, although only $31\,\mathrm{bits}$ can be used, since the last bit is above the Nyquist limit. The resolution limit of the NCO setpoint can be calculated to be $\Delta f_{NCO} = 69.85\,\mathrm{mHz}$:

$$\Delta f_{NCO} = \frac{f_{FPGA} \cdot N}{2 \cdot 2^{b_{FTW}}} = \frac{f_{Ny} \cdot N}{2^{b_{FTW}}} = \frac{150\,\mathrm{MHz} \cdot 2}{2^{32}} = 69.85\,\mathrm{mHz} \tag{4.11}$$

External dividers are usually involved in the path between the photo diode readout of the laser beat and the PFD input in order to increase the frequency range that electronic components can work with. They reduce the high frequency signals from GHz to MHz. Consequently, they lower the NCOs resolution by the division factors, which is represented by the value N, whose lowest value in this setup is $N = 2$. This NCO was developed in VHDL code and can be found in appendix chapter A.3.1.

4.3.2 Phase Frequency Detector (PFD)

After generating a tunable digital reference frequency, the DPLL continues with analyzing the phase difference between the two inputs, the NCO and the laser beat. Those inputs are fed into the Phase Frequency Detector (PFD), whose theoretical functionality was described in chapter 4.2.1 and outputs a signal which describes the phase relation between laser and NCO. Since the incoming signal of the laser must be digitalized so that the detector is capable of measuring its frequency, it has to be divided by external dividers on the board and in the software. Transforming the analog laser beat signal is achieved by an effective 1-bit ADC, which is the logic input of the FPGA. The FPGA's clock runs on a frequency of $f_{FPGA} = 300\,\mathrm{MHz}$, so the maximum frequency an input signal is allowed to have is the Nyquist limit which lies at $f_{Ny} = 1/2 f_{FPGA} = 150\,\mathrm{MHz}$. The aforementioned external dividers are necessary to achieve a readable laser beat frequency,

which can vary from MHz to GHz.
Laser frequencies used for $^{87}\mathrm{Rb}$ transitions lie in the range of THz, which are not processable for any electronic devices in the hardware. Therefore, the laser beam with a frequency f_1 is mixed with another beam with frequency f_2 close to it, generating mixed frequencies at $f_1 \pm f_2$, where $f_{Beat} = f_1 - f_2$ lies in the GHz range. This signal is called laser beat and is commonly used for laser frequency locking [103] and is fed into the PFDs LAS input. Further information on the laser system setups and the electronics will be given in chapter 6. The VHDL code of the PFD is attached in appendix chapter A.3.2.

4.3.3 Error calculation converting an analog pulse length to a digital phase error

The following section focuses on the error value calculation of the DPLL. In a traditional phaselock setup it is simply realized by a single phase detector. In order to achieve a higher error resolution, a faster reaction time and higher control bandwidth, the error calculation in the developed PLL is improved by phase shifting the FPGA clock to have four readout points during one clock cycle, which effectively increases the sampling rate. These four phase shifted values need to be added up to result in a higher resolution error value. This is achieved by four Twisted Ring Counter (TRC)s per PFD output channel, whilst simultaneously minimizing possible bit flips as noise sources through counting in Grey code. These counters need to be read out, decoded and synchronized afterwards to acquire the error value.

Twisted Ring Counter

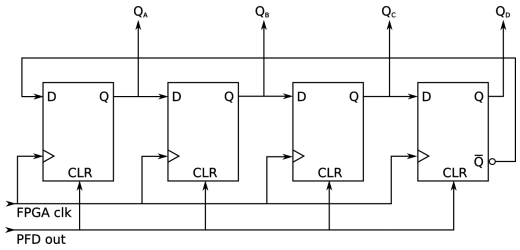

(a)

Clock Pulse No	FFA	FFB	FFC	FFD
0	0	0	0	0
1	1	0	0	0
2	1	1	0	0
3	1	1	1	0
4	1	1	1	1
5	0	1	1	1
6	0	0	1	1
7	0	0	0	1

(b)

Figure 4.10: Illustration of the $4\,\mathrm{bit}$ Twisted Ring Counter (TRC) realized with flip flops (figure 4.10a) and the resulting lookup table (figure 4.10b). The inputs of the TRC are the Up or Down PFD output and one of the four FPGA phase shifted $300\,\mathrm{MHz}$ clocks.

Error signals generated from the PFD, as described earlier, have output values, which consist of Up and Down signals or $e(t) \in [-1, 0 - +1]$ when described by the state machine. In order to increase the possible output values, a higher readout rate of the PFD would be necessary. The PFD only sees rising and falling edges of the two input signals resulting in an asynchronous output signal to the FPGA clock. It is possible to exploit the asynchronous nature by reading out its output

error faster than the FPGA clock by creating four phase shifted clocks and using them to read out the error value at a higher repetition rate. This creates an effective readout rate of $1200\,\mathrm{MHz}$ for the PFD and increases the value's length to $4\,\mathrm{bits}$. This leads to a higher output value for the error in case the inputs are very far apart and thus a faster PLL. Furthermore, the Up and Down output signals of the PFD are counted separately, so the higher value length is doubled and enables a spectrum for the error output of $8\,\mathrm{bits}$ which translates to $e(t) \in [-128, .., +128]$.
In order to get those higher values for the error signal, the initial two outputs needed to be added up which was realized through Twisted Ring Counter (TRC)s driven by the phase shifted clocks. Since there are two PFD outputs and four phase shifted clocks, eight TRCs are needed to add up the two $1\,\mathrm{bit}$ signals of the PFD to an $8\,\mathrm{bit}$ error value. The counters give out their value in Grey code, which is less sensitive to bit flips, but needs to be decoded to binary code later on for further processing. The schematic and resulting lookup table of the possible TRC values are shown in figure 4.10a and 4.10b. The VHDL code of the TRC is attached in appendix chapter A.3.3.

Decoder

Since the error signal generated from the TRCs is in Grey code, it needs to be converted to conventional code for further processing. A converter which translates these values at the clock rate of the FPGA was implemented for every TRC present in the code. After the converter sequence, the error signal is split into four phase shifted signals with a bit length of $b_{Dec} = 3$ for the Up and Down output of the PFD. The VHDL code of the converter is attached in appendix chapter A.3.4.

Synchronizer

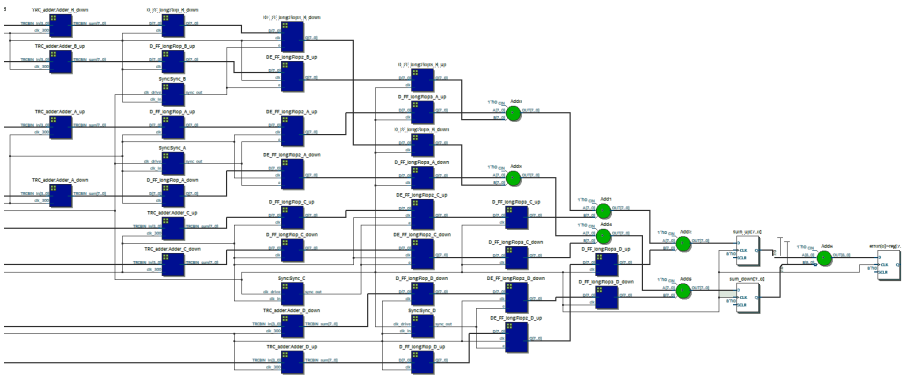

Figure 4.11: Illustration of the synchronizer VHDL code realized as a block diagram by the Quartus software. The red/yellow square blocks accumulate the values of each TRC Up/Down output for three $300\,\mathrm{MHz}$ clock cycles. The blue square blocks are flip flop structures to first synchronize the phase shifted signals to each other and then to the $100\,\mathrm{MHz}$ clock. The following circles are adders which first create the accumulated Up and Down signal and afterwards the $8\,\mathrm{bit}$ error output through subtraction. The input values have been decoded to conventional binary code from Grey code beforehand.

Assuming it would be possible to run the PID filter with $f_{FPGA} = 300\,\mathrm{MHz}$, the next processing step after the decoder is to synchronize the four phase shifted signals to one reference phase and performing a subtraction, which could be realized with a few flip flops. Unfortunately, the PID calculation consists of multipliers larger than $18\,\mathrm{bits}$ which cannot run with $300\,\mathrm{MHz}$ but only with

the lower $100\,\mathrm{MHz}$ clock of the FPGA. This limit is set by the speed grade of the multiplier elements of the Intel® MAX10 FPGA [123]. This requires an additional setup of flip flops and adders to synchronize the phase shifted input values to each other and create the error output in the slower clock domain. The schematic of the designed synchronizer after it was compiled in Quartus is illustrated in figure 4.11
Following the synchronization to the $100\,\mathrm{MHz}$, the $8\,\mathrm{bit}$ error signal is calculated by a subtraction and fed into the loop filter. The synchronizer code is attached in appendix chapter A.3.5.

4.3.4 PID loop filter

Calculating the P, I and D gain with the provided error signal seems straight forward, since equation 4.6 shows how the gains are calculated. In order to achieve a derivative and integral gain in VHDL code, a pipelining of the error value needed to be introduced. Pipelining in this case means, that the error value is on hold for one or more clock cycles and its values are saved in the FPGA's memory. This enables the calculation of the derivative and integral gain, that are defined as the change of the error value in time (D) and the steady state error (I). The proportional gain (P) is the current error input.
Special notice must be given in this code to the integral response, since it tends to increase excessively in a very short time frame. Therefore, it was defined as a very long bit string to not saturate immediately. Additionally, all gains have a saturation cap to not overflow. The realization can be best described through a block diagram of the FPGA code, which is illustrated in figure 4.12, where every flip flop in the chain introduces a pipelining in the calculation.
Furthermore, the multiplication with the factors K_P, K_I, K_D needs to be pipelined as well, since the immediate multiplication with the constants would strain the FPGA over its capabilities, due to the amplification factors being variables controlled by the user.
An additional pipeline step is necessary for the summation of the gains which creates the output value for the laser current control. This value also has a saturation cap, since it is turned into an analog signal by a $16\,\mathrm{bit}$ DAC, setting the limit to the accuracy and resolution of the output value. The schematic of the designed PID filter after it was compiled is shown in figure 4.12 and the VHDL code is attached in appendix chapter A.3.6. In this schematic, every flip flop, adder, multiplier and saturation block adds a pipelining to the loop filter.

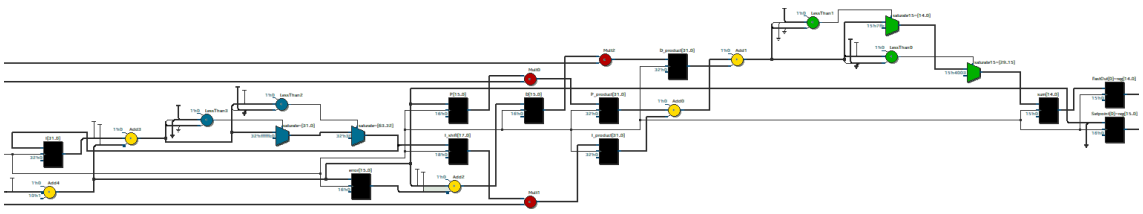

Figure 4.12: Illustration of the PID VHDL code realized with flip flops, multipliers and saturation blocks by the Quartus software. The black square blocks are flip flops and the yellow circles are adders. The blue circles in combination with the blue trapezes are the saturation function for the I gain and the green circles/trapezes combination are the saturation of the sum output. The red circles are the three multipliers, which multiply the P,I and D gain with their amplification factors.

The output value of this loop filter is a $16\,\mathrm{bit}$ signed value, which is fed to a $16\,\mathrm{bit}$ DAC, generating an analog voltage signal that is modulated onto the laser current.
The FPGA's resources which are required for the realization of the DPLL are illustrated in table 4.2.

Table 4.2: FPGA resources used for the implementation of the DPLL.

DPLL component	Logic cells	Logic registers	18×18 multipliers	Clock domain
NCO	46	39	0	300 MHz
PFD	3	2	0	None
TRCs	133	128	0	300 MHz
Decoders	112	0	0	300 MHz
Synchronizer	158	156	0	300 MHz & 100 MHz
PID	182	63	3	100 MHz

4.4 Transfer function

Following the description of the separate PLL components, the transfer function of the phase-lock can be obtained. This is necessary in order to compare the DPLL's performance with the theoretical performance this control loop would have. A transfer function is obtained by Laplace transferring the transfer functions of the individual components and describing them with the complex frequency s. In the Laplace domain, the open loop and closed loop transfer function can be obtained by simple multiplication of the components present in the loop. Later on, a transfer into the Z-domain is necessary, since digital components are described in control theory by a series of Dirac pulses, which is realized through this transformation.

4.4.1 Description in the Laplace domain

The transfer function of a system can be calculated to be able to predict a rough dimension of the system's performance. For PLLs, the transfer function can be calculated by dividing its components in fragments, transferring them into the Laplace domain and calculating the function for every component and combining them in the end by multiplication. The closed loop and open loop transfer functions can be approximated by assuming a linear PLL model, since transfer functions can only be calculated for linear systems [117]. In the following calculations, a basic PLL model is used for the calculations and specified later on for the developed DPLL [102]. The basic PLL setup in figure 4.1 can be described by the open loop transfer function $G(s)$ in the Laplace domain using the complex frequency $s = \delta + i\omega$ through:

$$G(s) = \frac{Y(s)}{X(s)} = D(s) \cdot F(s) \cdot V(s) \tag{4.12}$$

with $X(s)$ being the input and $Y(s)$ the output of the PLL after Laplace transformation. Starting with equation 4.6 for the description of the PID controller, one can Laplace transform this equation to get $F(s)$:

$$F(s) = K_P + \frac{K_I}{s} + K_D \cdot s \tag{4.13}$$

Since the phase detector gets phases as inputs and outputs a phase as well (frequencies are defined as the derivative of phases [102]), shown through equation 4.5, it is proportional in the

Laplace domain and its transfer function can be described by its gain K_d:

$$D(s) = K_d \tag{4.14}$$

The VCO can be described by the Laplace transfer of equation 4.10. Since its input is a linear value and it outputs a frequency, it can be described as a component with integral behavior and gain K_o:

$$V(s) = \frac{K_o}{s} \tag{4.15}$$

By combining equations 4.15, 4.14 and 4.12 the open loop transfer function $G(s)$ for the PLL is obtained:

$$G(s) = K_d \cdot \frac{K_o}{s} \cdot F(s) \tag{4.16}$$

The closed loop transfer function $H(s)$ relates the phase of the reference signal $\theta_r(s)$ with the phase of the VCO $\theta_o(s)$ in a closed loop:

$$\theta_o(s) = H(s) \cdot \theta_r(s) \tag{4.17}$$

with:

$$H(s) = \frac{G(s)}{1 + G(s)} = \frac{K_d K_o F(s)}{s + K_d K_o F(s)} \tag{4.18}$$

$H(s)$ also states the efficiency of transmitted phase to the VCO and therefore the phase noise suppression of the oscillator.
A measure of the transmitted phase noise is given by the error transfer function $E(s)$, which describes the relation of θ_e and θ_r:

$$\theta_e = E(s) \cdot \theta_r \tag{4.19}$$

and is calculated through:

$$E(s) = \frac{1}{1 + G(s)} = 1 - H(s) \tag{4.20}$$

The denominator $1 + G(s) = 0$ is known as the characteristic equation of a control loop, from which the natural radian frequency ω_n and the damping coefficient ζ can be calculated for second order PLLs. In case of a loop filter with a derivative gain, the equation tends to get complicated. Inserting equation 4.13 into 4.18 and after some simplifications, which are attached in appendix chapter A.4.1, $H(s)$ can be described through:

$$H(s) = \frac{s^2 \cdot (K_d K_o K_D) + s \cdot (K_d K_o K_P) + (K_d K_o K_I)}{s^2 \cdot (1 + K_d K_o K_D) + s \cdot (K_d K_o K_P) + (K_d K_o K_I)} \tag{4.21}$$

From the characteristic equation, one can obtain the damping coefficient ζ and the natural radian frequency ω_n of the loop through:

$$1 + G(s) = 0 = s^2 + 2\zeta\omega_n s + \omega_n^2 \tag{4.22}$$

The factors ζ and ω_n can now be calculated using equation 4.21 (the intermediate calculations are attached in A.4.2):

$$\omega_n = \sqrt{\frac{K_d K_o K_I}{1 + K_d K_o K_D}} \tag{4.23}$$

$$\zeta = \frac{K_P}{2}\sqrt{\frac{K_d K_o}{(1 + K_d K_o K_D)K_I}} \tag{4.24}$$

4.4.2 Discrete description of the DPLL in the Z-domain

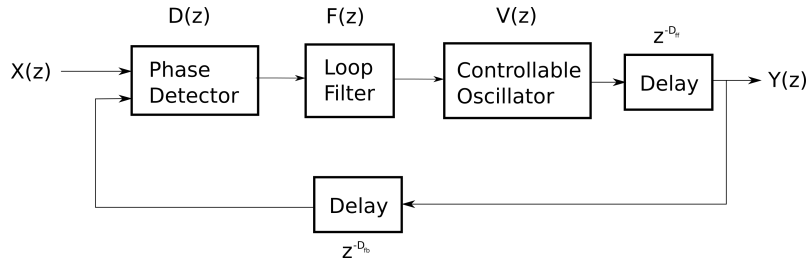

Figure 4.13: Setup of the digital PLL model developed in this thesis in the Z-domain with implemented delays. The individual components are described through their transfer functions in the Z-domain. A possible feed back and feed forward delay is introduced through the factors $z^{-D_{ff}}, z^{-D_{fb}}$.

Digital control systems are discrete. Therefore, they are transferred into the Z-domain to be described more accurately as a series of Dirac pulses with a sampling period [119]. The bilinear transform maps the s-plane in the Laplace domain onto the z-plane in the Z-domain through the substitution [108, 124]:

$$s \leftarrow \frac{1}{T_s}\left(\frac{z}{z-1}\right) \tag{4.25}$$

with $T_s = {}^1/_{f_s}$ being the sampling period. The discrete PLL model can be setup in the Z-domain in a similar matter as the basic model in the Laplace domain. The difference between the two models are the introduced delays in the system, which are illustrated in figure 4.13.
Based on equation 4.18, the system transfer function for the continuous model can be transferred with equation 4.25, resulting in:

$$H(z) = \frac{k_d k_o F(z) \cdot z^{-(D_{ff}+D_{fb})}}{\frac{1}{T_s}\left(\frac{z}{z-1}\right) + k_d k_o F(z) \cdot z^{-(D_{ff}+D_{fb})}} \tag{4.26}$$

with the transferred gains k_d, k_o of the phase detector and controllable oscillator. The coefficients $z^{-D_{ff}}$ and $z^{-D_{fb}}$ present a possible feed forward and feed back delay in the loop. Assuming

$D_{ff} = D_{fb} = 0$, this leads to:

$$H(z) = \frac{k_d k_o F(z)}{\frac{1}{T_s}\left(\frac{z}{z-1}\right) + k_d k_o F(z)} \tag{4.27}$$

The discrete transfer function of the PID filter can be obtained by using equation 4.13 and transforming s with equation 4.25 to z:

$$F(z) = k_P + k_I \cdot T_s \left(\frac{z}{z-1}\right) + \frac{k_D}{T_s}\left(\frac{z-1}{z}\right) \tag{4.28}$$

with k_P, k_I, k_D as the PID's respective transferred gains. After inserting equation 4.28 into 4.27, one can conclude through comparison, that the form of the discrete PLL model without any additional delays, is very close to the continuous model described in the previous chapter with the addition of the sampling period T_s to each factor. Since there are three variables (K_P, K_I, K_D) but only two factors to describe them as a function of (ζ, ω_n), the amplification factors will always be codependent to each other. Therefore, the coefficients of the Ziegler-Nichols tuning method in table 4.1 from chapter 4.2.2 are used to obtain the gain amplification coefficients and describe them with ζ, ω_n with equations 4.23 and 4.24:

$$k_P = \frac{K_P}{T_s} = \frac{0.6 \cdot K_c}{T_s} \tag{4.29}$$

$$k_I = \frac{K_I}{T_s} = \frac{K_P \omega_n}{2\zeta T_s} = \frac{0.6 \cdot K_c \omega_n}{2\zeta T_s} \tag{4.30}$$

$$k_D = \frac{K_D}{T_s} = \frac{K_d K_o K_I - \omega_n^2}{K_o K_d} = \frac{\frac{0.6 \cdot K_d K_o K_c}{\omega_n} - \omega_n^2}{K_d K_o} \tag{4.31}$$

The trade off between maximal overshoot and settling time to steady state can be influenced by ζ and is usually set, so the overshoot is minimized during a phase error. In praxis, a factor of $0.5 < \zeta < 2$ is a common range for the damping coefficient and $\zeta = 1/\sqrt{2} \approx 0.707$ is usually the best compromise between overshoot and settling time [97, 102, 108, 119]. The natural radian frequency ω_n is determined through the requirements to the DPLL, since it can be calculated through the desired minimum phase noise $\Delta\psi_{max}$ and the required jumping speed between two setpoints $\partial\Delta\omega/\partial t$. The necessary equations for the calculation are the following:

$$\lim_{s\to 0} \frac{2\partial\Delta\omega/\partial t}{s^2} \cdot \frac{1}{1+G(s)} = \frac{2\partial\Delta\omega/\partial t}{K_o K_d K_I} = \frac{2\partial\Delta\omega/\partial t}{\omega_{n,min}^2} = \Delta\psi_{max} \tag{4.32}$$

$$\leftrightarrow \omega_{n,min} = 2\pi f_{n,min} = \sqrt{\frac{2\partial\Delta\omega/\partial t}{\Delta\psi_{max}}} \tag{4.33}$$

The developed digital phase locked loop (DPLL) can now be customized to the laser systems to achieve the requirements for atom interferometry described in chapter 3.2, since they set the limits for the phase noise $\Delta\psi_{max}$ and jumping speed $\partial\Delta\omega/\partial t$ from whom K_P, K_I, K_D can be determined.

4.5 Simulation of the DPLL

Since the implementation of the PID loop filter challenged the FPGA resources to its limit, the assumption in equation 4.27 which stated, that there are no delays in the feedback loop could not be realized and an analytical solution in the z-Domain was not possible. Therefore, the DPLL was simulated with Altera ModelSIM® in order to achieve an estimation of the phaselock's performance. In this simulation, the NCO was used as the controllable oscillator, which was locked to a fixed frequency setpoint, generated by the simulation programm.

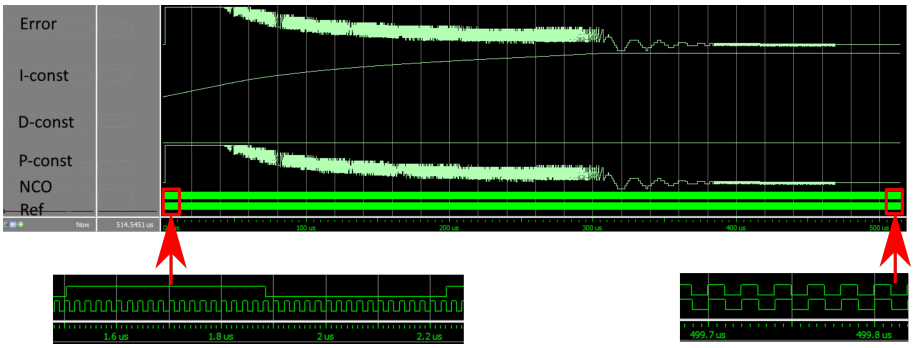

Figure 4.14: Simulation of the DPLL phaselocking a NCO to a fixed frequency setpoint. The NCO is used in this simulation as the controllable oscillator which is locked to a fixed frequency setpoint. The simulation was performed with Altera ModelSIM® .

Figure 4.14 illustrates the simulation of the phaselock, where the NCO is locked to the set frequency setpoint. The NCO is being adjusted to the frequency of the generated reference signal by the DPLL, which can be seen in the right zoom in 4.14 after the NCO had a different frequency in the beginning of the simulation, which is shown in the left zoom. Therefore, the phaselock first increases the frequency of the NCO, since the phase error between the signals is large. When the frequency of the NCO and the reference signal are the same, but the signals are out of phase, the phase locking starts, which is visible at about $310\,\mu\mathrm{s}$, where the phase error oscillates around 0. Around $470\,\mu\mathrm{s}$ the signals are phaselocked, since the phase error is 0 from this moment on.
The implementation of the loop filter's I gain revealed to be challenging. The integral part showed itself to saturate very quickly in the simulation, even with the lowest multiplication value $K_I = 1$. Therefore, it was realized as a bit stream with $32\,\mathrm{bit}$ in order to not saturate immediately and constantly output its maximum value. Since the implemented DAC on the developed hardware has only $16\,\mathrm{bit}$, the bit stream needed to be reduced before being summed up with the proportional and derivative gain (the description of the hardware will be subject in the following chapter). Subsequently, a cut of the integral gain was unavoidable. Simultaneously, the immediate saturation of the I gain needed to be considered and therefore the lower $10\,\mathrm{bits}$ of the calculated I gain were cut out. This increased the possible input values of K_I but at the same time reduced the accuracy of the PID filter, which is the aforementioned disadvantage in section 4.1 of a fully digital PLL.
This loss of accuracy and the resulting loss of possible phase noise suppression needs to be considered during the measurements in the following chapters, from which the phaselock's performance will be evaluated.
After successfully simulating a phaselocked controllable oscillator by the DPLL, it was ready for measurements with the hardware.

CHAPTER 5

Hardware

This chapter presents an overview of the hardware used for the DPLL. In order to accomplish the requirements of laser based experiments in microgravity, the developed hardware is part of the TBus standard, which is optimized for compact and autonomous operating systems. It is shortly described in the first section of this chapter for easier comprehension as well as the communication and the power supply board. The hardware, which was developed during this thesis is the third iteration of the laser frequency control board, which is described in detail afterwards. The chapter closes with a short description of the laser current driver board, which completes the hardware setup to control a laser system with the DPLL.

5.1 Hardware setup

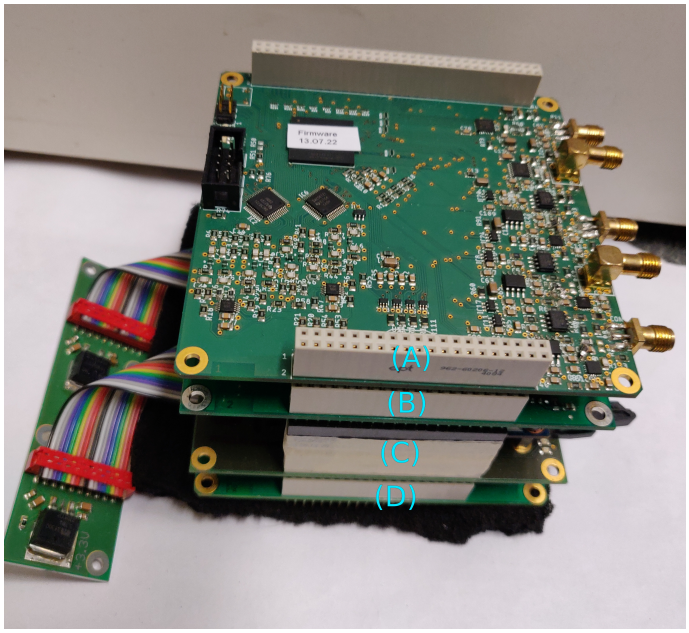

Figure 5.1: Picture of the hardware setup used for the DPLL measurements which consisted of a laser frequency control board (A), a laser current driver board (B), an Ethernet communication board (C) and a power supply board (D).

The DPLL hardware test setup consisted of the laser current driver board, the Ethernet communication board, the power supply board, and the laser frequency control board illustrated in figure 5.1. The frequency control board was developed during this thesis and is part of the TBus stan-

dard, similar to all the boards mentioned before.
TBus is an internal design standard for a printed circuit board (PCB) that was specifically created to meet the requirements of laser based experiments conducted in microgravity environments. This standard is designed to be optimal for compact, self-contained systems like drop tower capsules and sounding rockets. Originally developed by Dr. Thijs Wendrich for the usage in the QUANTUS drop tower missions, the TBus standard has been utilized in several PCBs with integrated microelectronics for experiments in atom optics within the LASUS project, which was supported by the DLR [30].
A stack of TBus cards can be accessed via an interface card, which in this setup was the Ethernet communication board. USB, PC104, NI-FPGA and plastic optical fibre (POF) are available as possible communication for the TBus as well. The boards used in the testing environment were able to function without negative voltages, so a power supply board that supplies positive voltages was sufficient for the environment. As a graphical user interface, LabVIEW® was chosen in order to control the testing environment. The communication protocol of the TBus standard has been described in detail here [38] and a short summary of the TBus standard is given in appendix chapter A.5.
In order to obtain the measured data from the experimental setups, the following lab equipment was used in the succeeding sections:

- R&S FSWP Phasenoise Analyzer for obtaining residual phase noise and spectrum data sets in the frequency domain [125],
- R&S RTM3004 oscilloscope for measuring data in the time domain [126],
- R&S HMP4040 as a laboratory power supply connected to the TBus power supply [127].

5.2 Laser frequency control board

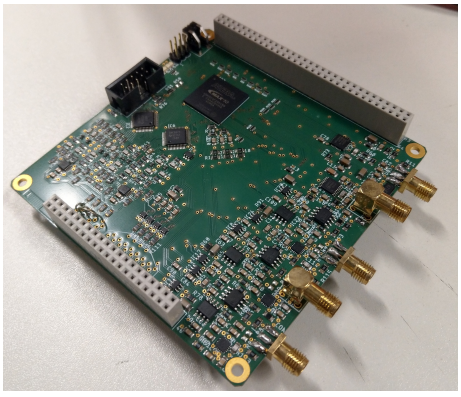

(a)

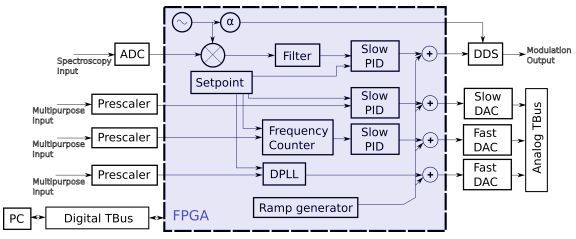

(b)

Figure 5.2: Illustration of the third iteration of the laser frequency control board. In figure 5.3a a picture of the developed frequency controller is shown and in figure 5.2b the functionality of the frequency controller is illustrated via a block diagram.

First in line is the laser frequency controller, whose Intel® 10M16DAF256C8G FPGA [123] included the DPLL software. The developed successor of the board's second iteration is shown in figure 5.2a and the schematic and board layout of the frequency controller are shown in the appendix chapter A.6.1.

The board is capable of controlling up to four lasers simultaneously through one spectroscopy lock and three phaselocks/offsetlocks. It consists of the following in- and outputs:

- 1 × Fast alternating current (AC) coupled input for any kind of modulation spectroscopy with a high resolution and a high sample rate ($12\,\mathrm{bit}, 25\,\mathrm{MSPS}$) analog digital converter (ADC), for stabilizing a laser on some atomic transition,
- 1 × DDS based sine wave output to enable frequency modulation spectroscopy,
- 3 × Multipurpose inputs which are connected to the FPGA as:
  - AC coupled beat inputs, to measure a beat signal for frequency stabilization, up to about $2\,\mathrm{GHz}$,
  - DC coupled inputs with an auxiliary, low speed ADC ($12\,\mathrm{bit}100\,\mathrm{kHz}$), for basic spectroscopy without modulation to help with locating the frequency of the lasers that use other stabilization methods,
  - DC coupled RF power detector for amplitude measurements of input signals up to $2\,\mathrm{GHz}$,
- 4 × Fast outputs ($14\,\mathrm{bit}, 25\,\mathrm{MHz}$) for the current drivers, connected via the analog TBus connector,
- 4 × Slow outputs ($14\,\mathrm{bit}, 100\,\mathrm{kHz}$) to control the temperature controllers or the piezo outputs, also connected via the analog TBus connector.

The communication with the frequency controller's FPGA happens through the digital TBus. The first path in figure 5.2b is the spectroscopy path. Via the AC coupled spectroscopy input, the modulation transfer spectroscopy stabilization is realized. The input signal is mixed with an internal oscillator and after passing a filter, the resulting signal is fed into a slow PID. Its control value is used afterwards by the DDS chip on board to create a modulation sine wave. This output wave is modulated onto a laser current to stabilize it to some atomic transition via a gas cell. An additional phase shifting is also implemented in the path.
On the input side, the beat signal is connected to the FPGA by three inputs with each including a divider IC in their path from ON Semiconductor (MC12093) [128]. The available division values are $N = 2, 4, 8$ in addition to a divider in the FPGA with the possible values $N = 1, 2$. The combination allows a maximum division of $N = 16$, enabling a readout frequency limit of $2.2\,\mathrm{GHz}$ for beat frequencies. The readout of the beat signal occurs through the FPGA's low volt differential signalling (LVDS) inputs, which are less sensitive to high frequency noise. This signal can now be processed in two ways:

- either by a frequency counter to create a control value via the slow PID (which runs at $10\,\mathrm{MHz}$)
- or by the DPLL to create a control value with its implemented fast PID (which was described in section 4)

The digital output setpoint of both options is converted to an analog signal by a DAC from Texas Instruments (DAC5672) [129]. The output compliance range goes from $0\,\mathrm{V}$ to $3.3\,\mathrm{V}$, which is converted to a current range on the laser current driver board, explained in the next section. The accuracy of the output signal was strongly dependent on the accuracy of the DAC. The converted output signal goes from the DAC to the fast outputs into the analog TBus, from where it reaches the laser current driver board.

If the ECDL's frequency is steered through its cavity length by a piezo element alongside its current, the control signal originates from a PID controller also implemented in this board's FPGA. The control signal is given out through the slow outputs of the frequency controller into the analog TBus connector by the analog signal output of the DAC.

5.3 Laser current driver board

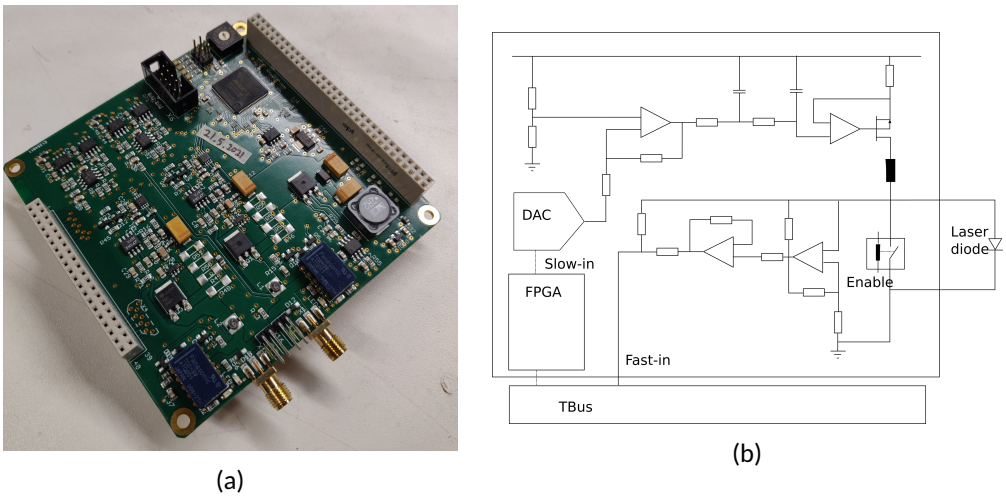

(a) (b)

Figure 5.3: Illustration of the fourth iteration of the laser current driver board. A picture of the laser current driver is shown in figure 5.3a and in figure 5.3b the functionality of the current driver is illustrated via a block diagram.

The laser current driver board, as the name suggests, controls the currents of the laser diodes by modulating the control value it receives from the frequency control board onto the current. The output of the DPLL that generates the control value drives one current output on this board. Figure 5.3a illustrates the fourth iteration of the current driver, which was developed by Dr. Thijs Wendrich. It is based on a setup described by K. G. Libbrecht and J. L. Hall [130] and modified with additional features for remote operation and a more detailed description can be found here [30]. The board contains two output ports for the laser current, the maximum amplitude of which is determined by two paths on the board:

- the slow input controlling the operating point, that is adjusted in order to convert $5\,\mathrm{V}$ to a current up to $140\,\mathrm{mA}$, which is specified by the onboard soldering options and set by the user via the FPGA,
- the fast input controlling the modulation, which is adjusted by the conversion of the $0\,\mathrm{V} - 3.3\,\mathrm{V}$ given out by the frequency control board to a current around $1\,\mathrm{mA}$. This signal is modulated onto the operating current and includes the control signal of the DPLL output.

The output of the frequency control board and the modulation path is illustrated in 5.3b. The schematic and board layout is shown in the appendix chapter A.6.2, which includes the paths of the operating point and the modulation point. The resistors on the board were adjusted in order to provide a maximum laser current of $110\,\mathrm{mA}$ for the measurements with the laser diode.

CHAPTER 6

Measurements

This section presents the characterization of the developed DPLL implemented into the new iteration of the frequency control board as well as the measurements carried out using this system. Using the hardware configuration described in the previous chapter, a characterization of the phaselock was performed with an electronic VCO, which served as a testing environment for subsequent measurements with different laser systems.
For the measurements two lasers of the QPort project were utilized and phaselocked to characterize the DPLL's performance. The ability to execute far frequency jumps is a fundamental trait of the DPLL, which is only limited by the current limit of the hardware. Therefore, a laser system consisting of ECDLs with a broader current range then the QPort lases was sought after. The lasers developed by the group in the "Humbold Universität zu Berlin" turned out to be an excellent testing environment for far frequency jumps, especially since they will be used in the MAIUS-B flight model, alongside the DPLL.
Ultimately, the phaselock's performance regarding Raman double diffraction in a MZI setup was tested with ^{87}Rb BECs, that were created in the MAIUS-B physics package [131] using their ground laser system.

6.1 Preliminary characterization of the DPLL with a VCO

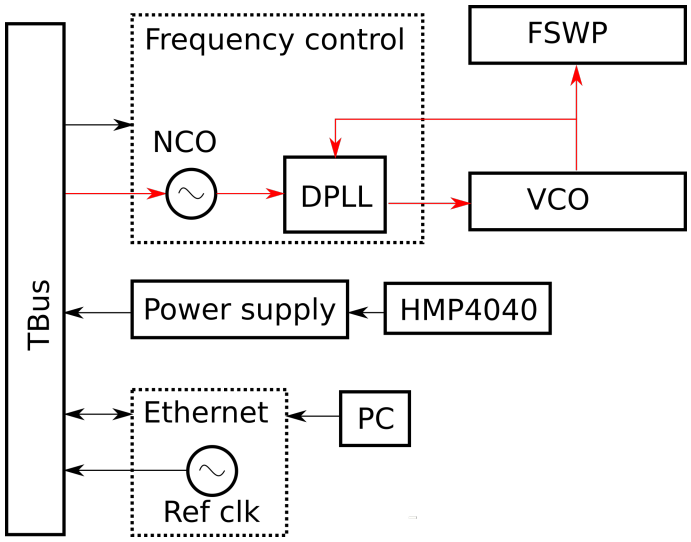

Figure 6.1: Illustration of the setup with a Voltage Controlled Oscillator (VCO) for a preliminary DPLL characterization. The data for the power and phase noise spectral density of the VCO, the Numeric Controlled Oscillator (NCO) and the reference oscillator were obtained in loop by the Phasenoise Analyzer (FSWP).

A laser, as explained in chapter 4.2.4, can be approximated as a VCO for the purposes of developing the DPLL. Therefore, in preparation for the implementation with lasers, a testing environment with an electronic VCO was realized in order to achieve a phaselock with the DPLL, as illustrated in figure 6.1.
A MiniCircuits® POS300+ VCO [132] was used for this setup with an accessible tuning range of $50\,\mathrm{MHz}$ between $130\,\mathrm{MHz} - 180\,\mathrm{MHz}$ for the $3.3\,\mathrm{V}$ voltage output range of the frequency control card.
This setup was assembled to achieve a preliminary characterization of the DPLL for later comparison with the performance on a laser system.

6.1.1 Characterization of the NCO and reference oscillator

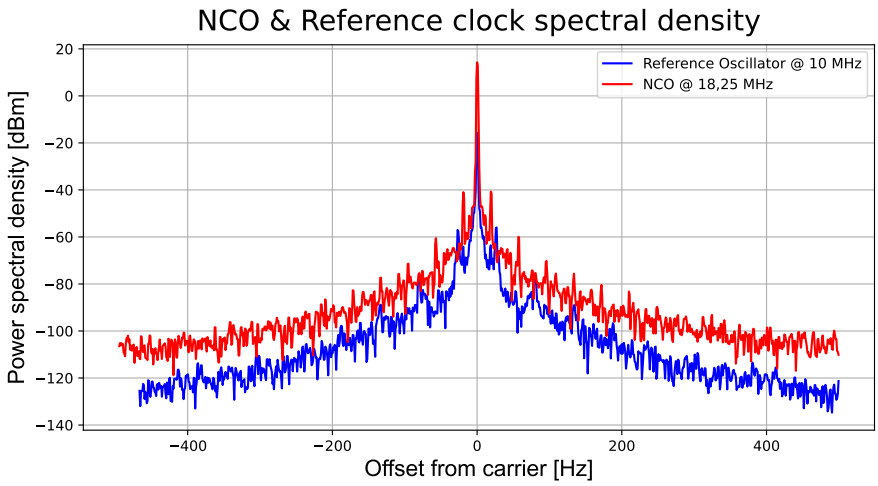

(a)

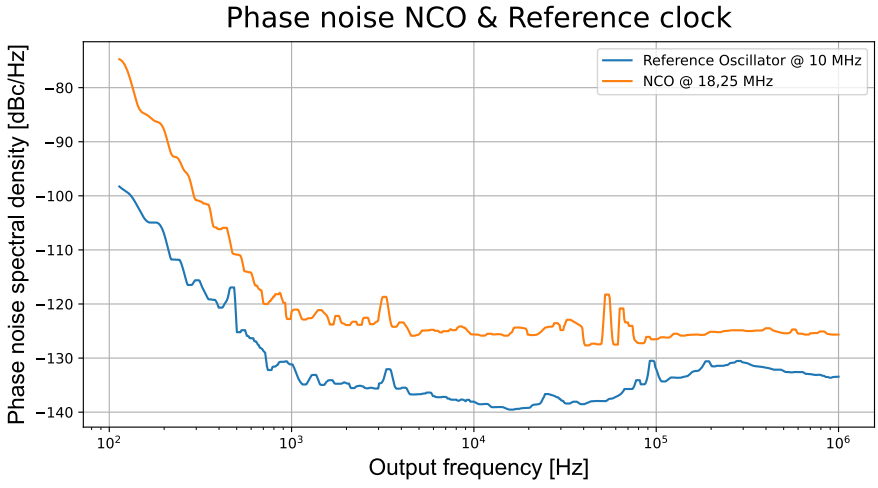

(b)

Figure 6.2: Results of the NCO measurements. In 6.2a, the power spectral density of the NCO and the reference clock of the TBus stack is illustrated. In 6.2b the one-sided phase noise spectral density of the reference clock and the NCO is illustrated. The reference clock ran at a frequency of $10\,\mathrm{MHz}$ and the frequency setpoint of the NCO was set to $18.75\,\mathrm{MHz}$.

Prior to the measurements with a free running and locked VCO, the Numeric Controlled Oscillator (NCO) needed to be characterized. Since the NCO of the PLL code imprinted its noise directly onto the oscillator, its power and phase noise spectral density of its signal were measured at a debug pin on the frequency control board with the RTM3004 oscilloscope.
The graphs 6.2a and 6.2b show the results of the measurements for the NCO at a carrier frequency of $18.75\,\mathrm{MHz}$ which translates to the VCO setpoint of $150\,\mathrm{MHz}$. The power spectral density showed a $3\,\mathrm{Hz}$ line width at FWHM with a RBW of $1\,\mathrm{Hz}$. The rms phase noise accumulated to $2\,\mathrm{mrad}$ over a bandwidth of $10\,\mathrm{Hz} - 1\,\mathrm{MHz}$ with a RBW of 10 %.
The FPGA used the reference clock of the TBus system internally to create the clock frequency for the NCO and the DPLL code and therefore imprinted its noise into the loop as well. Therefore, the phase noise of the reference clock was imprinted to the NCO and needed to be characterized as well. The reference oscillator was an oven stabilized quartz oscillator from Abracon® [133] which ran at a stable frequency of $10\,\mathrm{MHz} \pm 10\,\mathrm{ppb}$. Figure 6.2a and 6.2b show the results of the measurements for the reference oscillator next to the NCO. The power spectral density showed a line width of $3\,\mathrm{Hz}$ with a RBW of $1\,\mathrm{Hz}$ for the oscillator and the phase noise spectral density a rms phase noise of $350\,\mu\mathrm{rad}$ for a bandwidth of $10\,\mathrm{Hz} - 1\,\mathrm{MHz}$. Spot noise measurements for the NCO and the reference clock are illustrated in table A.2 in the appendix.

6.1.2 Performance without the DPLL

Prior to the characterization of the phaselock in this experimental setup, measurements with an inactive DPLL were conducted. The power and phase noise spectral density of the VCO are illustrated in graphs 6.3 and 6.4. They show the power spectral density within a bandwidth of $1\,\mathrm{MHz}$ around the carrier peak and the one-sided phase noise spectral density for a bandwidth of $100\,\mathrm{Hz} - 1\,\mathrm{MHz}$. The spectrum showed a line width of $3\,\mathrm{kHz}$ at FWHM with a RBW of $1\,\mathrm{kHz}$ and a rms phase noise of $3\,\mathrm{rad}$ over the bandwidth with an RBW of 10 %. The RBW for the phase noise measurement of each FFT segment was based on a percentage of the segment start offset by the instrument [125].

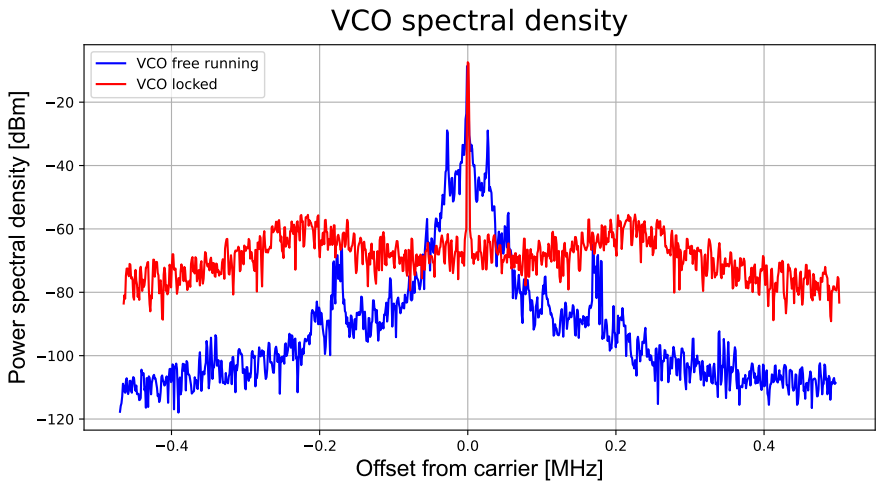

Figure 6.3: Measurement results of the DPLL for the power spectral density of the free running and phaselocked electronic VCO. The frequency setpoint for the phaselocked VCO was set to $150\,\mathrm{MHz}$.

6.1.3 Performance with the DPLL

Afterwards, the VCO was optimized to a setpoint frequency of $150\,\mathrm{MHz}$ where the power and phase noise spectral density plots were obtained. The parameters for these measurements were:

- proportional gain $P = 674$
- integral gain $I = -3$
- derivative gain $D = 151$
- internal divider $N = 8$
- correlation factor $XCorr = 10$

The spectral density of the VCO with an active DPLL software is illustrated in figure 6.3 and showed a line width of $23\,\mathrm{Hz}$ at FWHM. The phase noise spectral density of the locked oscillator is illustrated in figure 6.4 and revealed a rms phase noise of $30\,\mathrm{mrad}$ for a bandwidth of $10\,\mathrm{Hz} - 1\,\mathrm{MHz}$ with a RBW of 10 %. Spot noise measurements for the free running and locked VCO are illustrated in table A.1 in the appendix.

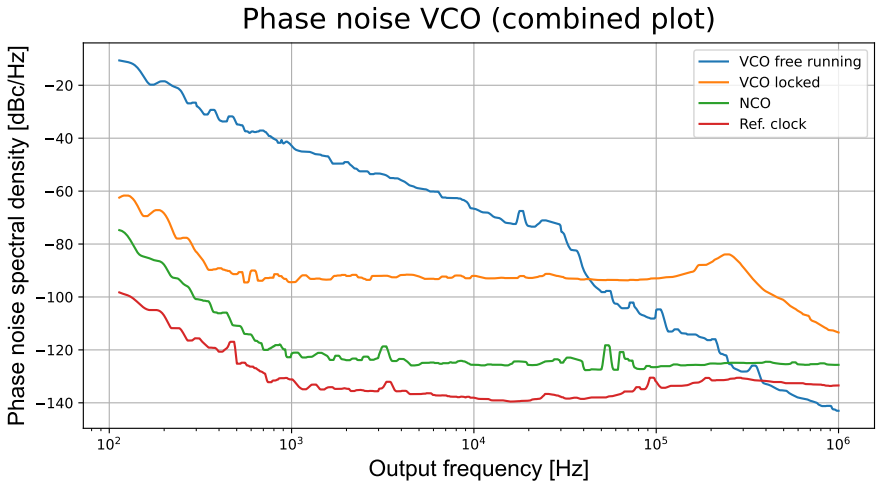

Figure 6.4: One-sided phase noise spectral density of the VCO with (red) and without (blue) an active DPLL. The frequency setpoint for the measurement with an active phaselock code was set to $150\,\mathrm{MHz}$.

6.1.4 Discussion of DPLL results at the VCO

Starting with the characterization of the NCO, the line width at a setpoint of $18.75\,\mathrm{MHz}$ was measured to be $3\,\mathrm{Hz}$ for an RBW of $1\,\mathrm{Hz}$, which was the highest accuracy that the measurement tool provided for the power spectral density. The reference oscillator was measured to be at the same line width. A difference could be seen when observing the one-sided phase noise spectral density. The NCO had a higher phase noise across the bandwidth from $100\,\mathrm{Hz}$ to $1\,\mathrm{MHz}$ compared to the reference oscillator. The spot noise measurements revealed, that the mean phase noise of the NCO was about $10\,{}^{dBc}/_{\mathrm{Hz}}$ higher compared to the reference oscillator between $1\,\mathrm{kHz}$ and $1\,\mathrm{MHz}$ to the carrier. The spot noise measured at $100\,\mathrm{Hz}$ to the carrier revealed to be about

$20\,{}^{dBc}/_{\mathrm{Hz}}$ higher than the reference oscillator. The origin of the noise could be found in the FPGA's datasheet [123], which showed, that it's internal FPGA PLL adds this noise to the NCO. This resulted in the measured rms phase noise of the NCO at about $2\,\mathrm{mrad}$, which was higher than the reference oscillators phase noise of $350\,\mu\mathrm{rad}$.
The performance for the electronic VCO showed very promising results by reducing the unlocked VCO's initial line width from $3\,\mathrm{kHz}$ to $8\,\mathrm{Hz}$ at FWHM. The integrated phase noise spectral density S_ϕ was decreased from $7\,\mathrm{dBc}$ to $-30\,\mathrm{dBc}$ which resulted in the rms phase noise decreasing from about $3\,\mathrm{rad}$ to $30\,\mathrm{mrad}$ for the bandwidth of $100\,\mathrm{Hz}$ to $1\,\mathrm{MHz}$. The spot noise measurement also illustrated very good noise suppression in comparison with the unlocked VCO. Obtained values of spot noise were measured to be below $-90\,{}^{dBc}/_{\mathrm{Hz}}$ above a frequency of $1\,\mathrm{kHz}$ and at $-64.19\,{}^{dBc}/_{\mathrm{Hz}}$ at $100\,\mathrm{Hz}$ to the carrier. Above $1\,\mathrm{MHz}$ to the carrier, the phase noise spectral density fell below $-100\,{}^{dBc}/_{\mathrm{Hz}}$, which showed the expected low pass filter behavior of a PLL. The control bandwidth was visible through distinguishing the characterizing control peak of a PLL which was positioned at roughly $350\,\mathrm{kHz}$.
Even though the DPLL showed a promising noise suppression inside its control bandwidth, the mean phase noise spectral density of the VCO revealed itself to be about $20\,{}^{dBc}/_{\mathrm{Hz}}$ higher than the NCO, whose origin could not be the FPGA's PLL. The reason for the additional noise was the result of the way the I gain was generated, as explained in chapter 4. The rounding of the error value in the code resulted in a rounding of small errors to 0 and that led to a reduced noise suppression of the loop, which was visible in the phase noise spectral density and the rms phase noise of the VCO. The calculated phase jitter for the bandwidth was measured to be $35\,\mathrm{ps}$.
The successful realization of a phaselocked VCO opened the way to test the DPLL with a laser system, since the noise suppression should be sufficient for an ECDL, which has common line widths of about a few $100\,\mathrm{kHz}$.

6.2 Characterization of the DPLL with ECDLs

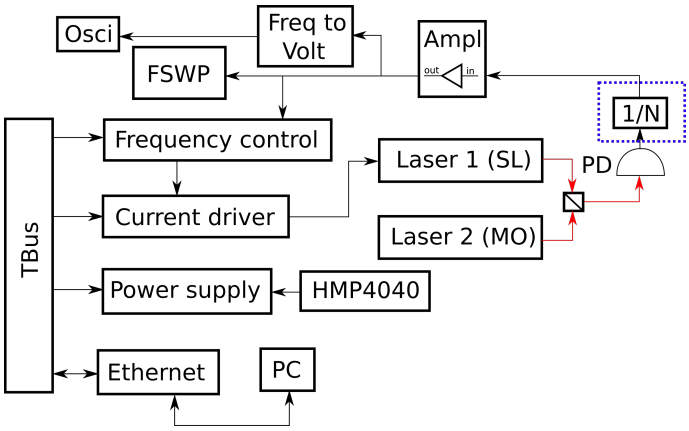

Figure 6.5: Illustration of the laser system setup at the QPort experiment for the characterization of the DPLL. The beat signal between laser 1 (SL) and laser 2 (MO) is read out by a photo diode (PD) and passed through a frequency divider (1/N) if needed. The output signal is then amplified (Ampl) and split multiple paths. In order to create a feedback loop, the signal is fed back to the frequency control board, where it is processed by the DPLL to create a control value for the current driver so that the laser can be phaselocked. The other signal path lead to the Phasenoise Analyzer (FSWP) to obtain the power and phase noise spectral density. A jumping sequence between frequency setpoints is analyzed by a frequency to volt converter, which gives out a signal processable by the RTM3004 oscilloscope.

The successful demonstration of the phaselock firmware with an electronic VCO opened the way to the next stage, which was testing the phaselock in a laser system environment. The chosen laser system is illustrated in figure 6.5 and was part of the neighboring QPort experiment [134, 135]. A fiber diode laser from NKT Photonics® 's laser system Koheras HARMONIK [136] and an ECDL [137] was optically mixed with each other. The resulting beat signal was fed into the input of the frequency control board after passing an ZFL-500NL+ amplifier [138] to obtain the necessary minimal readout amplitude of the board.
The first measurements were conducted with a "free running" master laser, i.e. the laser was not locked to an atomic transition through modulation transfer spectroscopy via a gas cell. Therefore, the frequency of the laser changed with time due to temperature shifts in the laboratory environment. The output current was set to $102.3\,\mathrm{mA}$ with an available current tuning range of about $2\,\mathrm{mA}$, which translated to $80\,\mathrm{MHz}$ for the DPLL.
Since the master laser was not locked, the beat frequency could be tuned close to $350\,\mathrm{MHz}$ by adjusting the master laser's current, thus achieving a testing environment without additional external dividers. The internal division for the DPLL was set to $N = 8$.
The data processing of the beat signal by the hardware and phaselock firmware is similar to the previous testing environment up to the output point of the control value to the fast outputs. Here, the signal was fed from the analog TBus to the laser current driver board and modulated onto the output current which steered the ECDL, as illustrated in figure 5.3b. This laser was therefore titled slave oscillator (SL) and the laser from NKT Photonics was titled the master oscillator (MO). In the following measurements the beat signal was read out in-loop.

Table 6.1: Frequencies of the signals at different measurement points.

Measurement	NCO output	Beat input	Laser/VCO
VCO	$18.75\,\mathrm{MHz}$	$150\,\mathrm{MHz}$	$150\,\mathrm{MHz}$
Laser/MO locked	$41.25\,\mathrm{MHz}$	$330\,\mathrm{MHz}$	$1.320\,\mathrm{GHz}$
Laser/MO free running	$43.75\,\mathrm{MHz}$	$350\,\mathrm{MHz}$	$350\,\mathrm{MHz}$

Subsequent to the characterizing measurements with a free running MO, the DPLL software was tested with a frequency locked MO. The NKT laser was locked to the ^{85}Rb cooling transition which has a detuning of $1.5\,\mathrm{GHz}$ to the ^{87}Rb cooling transition. The beat between SL and MO resulted in a frequency around $1.3\,\mathrm{GHz}$. Since the tuning range for the current amounted to $320\,\mathrm{MHz}$ around the setpoint, the laser could not be locked to a setpoint around $350\,\mathrm{MHz}$. Therefore, an additional divider with $N = 4$ was added to the path between the readout of the photo diode and the beat input of the frequency controller. This resulted in a beat frequency close to $350\,\mathrm{MHz}$.
The current of the laser current driver was set to $100.8\,\mathrm{mA}$ with an available frequency tuning range for the DPLL of about $320\,\mathrm{MHz}$ for the laser without division. An internal division of $N = 8$ was chosen in addition to the external divider. The measured frequencies in the testing environment differ, depending where in the loop they are measured, since dividers are implemented in the loop. The values at the NCO output, the frequency control board's beat input and the actual frequency at laser/VCO are displayed in table 6.1.

6.2.1 Performance without the DPLL

Prior to the characterization of the DPLL in this laser testing environment, measurements were conducted using an inactive phaselock to serve as a basis for comparison later on. Figure 6.6a

depicts the power spectral density of the laser beat with a free running and locked MO, respectively. The graph illustrates the frequency spectrum with a bandwidth of $10\,\mathrm{MHz}$ close to the carrier peak and indicated a line width of $40\,\mathrm{kHz}$ for a locked and $90\,\mathrm{kHz}$ for a free running master laser at FWHM.
Posterior to the measurements of the spectral density, measurements of the one-sided phase noise spectral density were conducted with an inactive DPLL and a locked and free running master laser in order to be comparable, which the graph 6.6b displays.

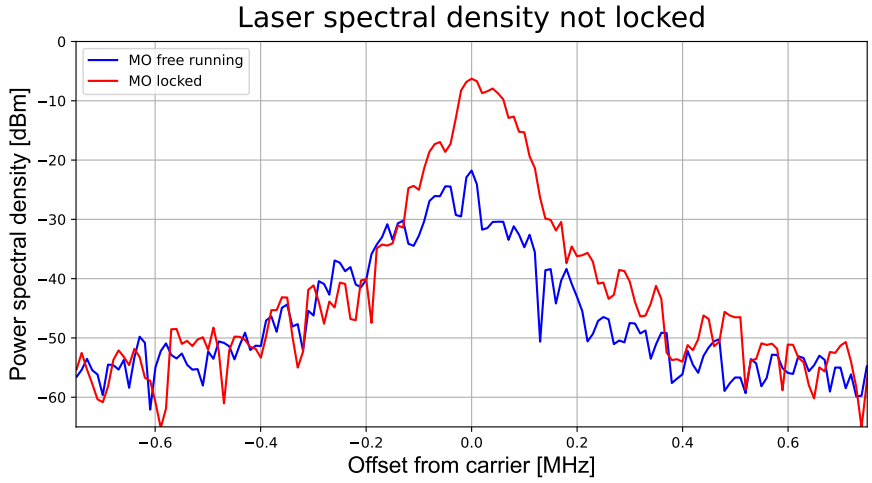

(a)

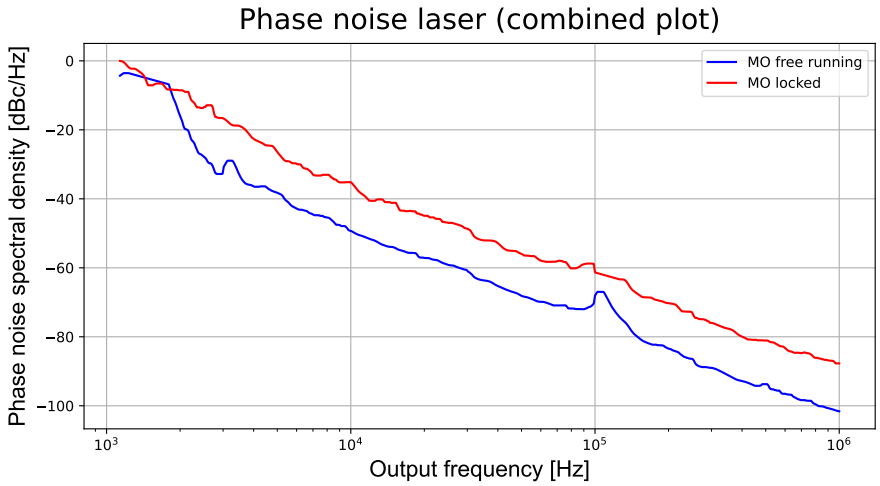

(b)

Figure 6.6: Illustration of the power spectral density 6.6a and the one-sided phase noise spectral density 6.6b of the QPort laser beats without the DPLL. The blue curves show the measured densities with a locked MO and the red curves with a free running MO. The phase noise spectral density can only be obtained for a stable oscillation (explained in section 3.2). Therefore, the bandwidth for the measurement was set between $1\,\mathrm{kHz}$ and $1\,\mathrm{MHz}$, since an unlocked laser tends to shift with time, which lead to values above $0\,{}^{dBc}/_{\mathrm{Hz}}$ below $1\,\mathrm{kHz}$, i.e. values above the carrier.

6.2.2 Performance with the DPLL

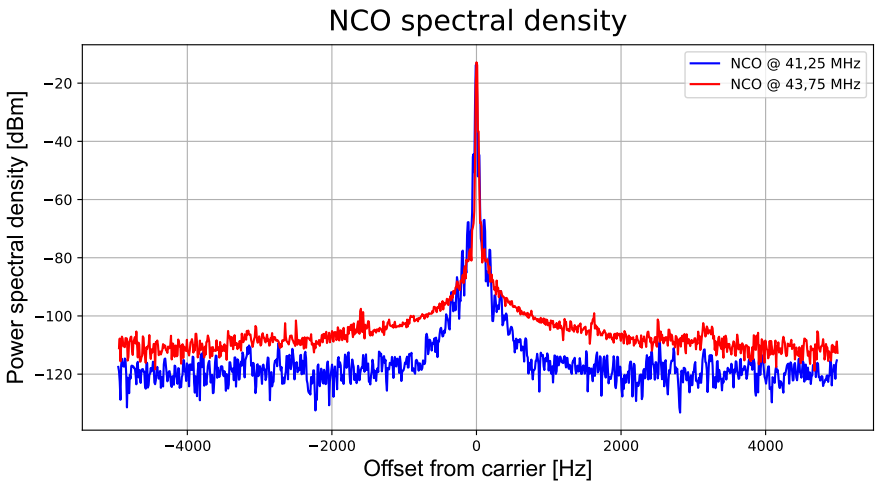

(a)

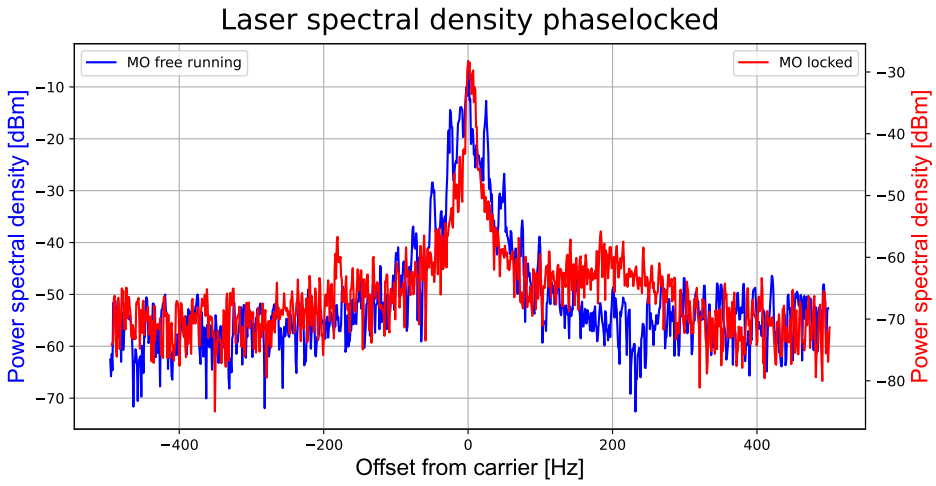

(b)

Figure 6.7: Illustration of power spectral densities. In 6.7a the NCO with frequency setpoints for the locked (blue) and free running MO (red) are displayed. In 6.7b the power spectral density for the laser beats with active DPLL are illustrated for a locked (red) and free running (blue) MO.

After conducting measurements using an inactive code, the slave ECDL was locked to a beat frequency of $350\,\mathrm{MHz}$ for a free running master laser. For the measurements with a locked master laser, a setpoint of $1.320\,\mathrm{GHz}$ was chosen, since the setpoint at $350\,\mathrm{MHz}$ couldn't be reached due to mode hops of the laser.
In order to evaluate the phase noise and spectral density of the laser beat later on, the NCO signal created by the DPLL code was outputted through a debug pin on the frequency control board. Since the noise from the NCO is directly imprinted onto the oscillator, this allowed for an accurate measurement of the phaselock's performance in the laser environment by subtracting the noise of the reference.

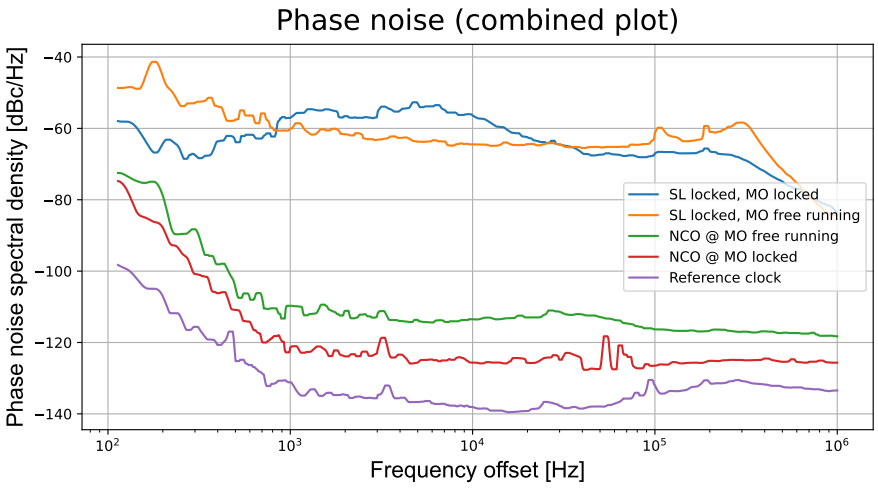

Figure 6.8: One-sided spectral density of the phase noise for the reference oscillator, the NCO and the QPort laser beat (SL) for a locked and free running master oscillator (MO) with active DPLL.

The graph 6.7a show the results of the NCO measurement at a carrier frequency of $43.75\,\mathrm{MHz}$ for the free running and $41.25\,\mathrm{MHz}$ for the locked master laser. The spectral density plot showed a $30\,\mathrm{Hz}$ line width for the NCO setpoint with the locked and $30\,\mathrm{Hz}$ for the NCO setpoint with the free running master laser at FWHM. The graph 6.8 shows the one-sided phase noise spectral density from which the rms phase noise for the different setpoints of the NCO was calculated. The rms phase noise for the NCO setpoint for a free running laser was $3\,\mathrm{mrad}$ and for the locked master laser $5\,\mathrm{mrad}$ integrated over a frequency bandwidth of $100\,\mathrm{Hz} - 1\,\mathrm{MHz}$.

Table 6.2: Resulting measurement data at the QPort experiment for the reference oscillator, the NCO, the VCO and the laser beat between SL and MO. The bandwidth for obtaining these values was from $100\,\mathrm{Hz}$ to $1\,\mathrm{MHz}$.

Signal	Carrier ν_0	Spectral density S_ϕ	rms Phase noise $\Delta\phi(f)$	Phase jitter $\Delta\phi(t)$
Reference oscillator	$10\,\mathrm{MHz}$	$-70\,\mathrm{dBc}$	$350\,\mu\mathrm{rad}$	$5\,\mathrm{ps}$
NCO for VCO	$18.25\,\mathrm{MHz}$	$-60\,\mathrm{dBc}$	$2\,\mathrm{mrad}$	$15\,\mathrm{ps}$
NCO/MO locked	$41.25\,\mathrm{MHz}$	$-50\,\mathrm{dBc}$	$6\,\mathrm{mrad}$	$20\,\mathrm{ps}$
NCO/MO free running	$43.75\,\mathrm{MHz}$	$-50\,\mathrm{dBc}$	$3\,\mathrm{mrad}$	$10\,\mathrm{ps}$
VCO free running	$\approx 150\,\mathrm{MHz}$	$7\,\mathrm{dBc}$	$3\,\mathrm{rad}$	$3\,\mathrm{ns}$
VCO with DPLL	$150\,\mathrm{MHz}$	$-30\,\mathrm{dBc}$	$30\,\mathrm{mrad}$	$35\,\mathrm{ps}$
SL with DPLL/MO locked	$1.320\,\mathrm{GHz}$	$-10\,\mathrm{dBc}$	$490\,\mathrm{mrad}$	$230\,\mathrm{ps}$
SL with DPLL/MO free running	$350\,\mathrm{MHz}$	$-5\,\mathrm{dBc}$	$800\,\mathrm{mrad}$	$360\,\mathrm{ps}$
SL free running/MO locked	$\approx 340\,\mathrm{MHz}$	$55\,\mathrm{dBc}$	$950\,\mathrm{rad}$	$350\,\mathrm{ns}$
SL free running/MO free running	$\approx 430\,\mathrm{MHz}$	$40\,\mathrm{dBc}$	$110\,\mathrm{rad}$	$50\,\mathrm{ns}$

Following the characterization of the NCO for the setpoint frequencies, the spectrum and phase noise of the laser beat, the spectral density of the laser beat with an active DPLL and a locked or free running master laser respectively, was obtained. The power spectral density of the laser beat with an active DPLL software showed a line width of $50\,\mathrm{Hz}$ for a locked and $70\,\mathrm{Hz}$ for a free running master laser at FWHM.

Interpreting the phase noise spectral density of the laser beat resulted in a rms phase noise of $800\,\mathrm{mrad}$ for a free running and $490\,\mathrm{mrad}$ for a locked master oscillator, integrated over a frequency span of $100\,\mathrm{Hz} - 1\,\mathrm{MHz}$. The control bandwidth of the DPLL software could also be obtained from figure 6.8 through distinguishing the characterizing control peaks of a phase locked loop which were positioned at roughly $350\,\mathrm{kHz}$ in the graph. Spot noise data were also obtained during these measurements and are displayed in table A.3 for the reference oscillator, the NCO and the laser beat for a free running and locked master oscillator (MO).
From the measured data for the phase noise, the imprinted phase jitter can be calculated through equation 3.29 and is displayed for the conducted measurements in table 6.2.

6.2.3 Discussion of DPLL results at the laser system

The NCO's performance played a critical role by limiting the best possible results to its own performance. Since the frequency setpoints for the laser were different to the setpoint for the characterization with the electronic VCO, its phase noise and power spectral density was measured once more. The measured power spectral density showed a line width of $\approx 3\,\mathrm{Hz}$ for all used setpoints. The obtained one-sided phase noise spectral density illustrated a noise level below $-110\,{}^{dBc}/_{\mathrm{Hz}}$ between $10\,\mathrm{kHz}$ and $1\,\mathrm{MHz}$, between $-90\,{}^{dBc}/_{\mathrm{Hz}}$ and $-110\,{}^{dBc}/_{\mathrm{Hz}}$ for $1\,\mathrm{kHz}$ and around $-70\,{}^{dBc}/_{\mathrm{Hz}}$ for $100\,\mathrm{Hz}$ to the carrier. The rms phase noise between the NCO setpoints vary between $2\,\mathrm{mrad}$ and $5\,\mathrm{mrad}$ with a resulting phase jitter between $12.864\,\mathrm{ps}$ and $21.094\,\mathrm{ps}$. The varying phase and spot noise between the different setpoints could be explained by the digital nature of the NCO. Frequencies produced by the NCO as a reference signal for the PFD were created through FTWs as explained in section 4.2.3. Certain frequencies in the digital domain could not be described exactly by a bit stream and were achieved only as a beat signal between two close reference points. This mechanism resulted in worse rms phase noise values of the NCO for different frequencies.
The conducted measurements were carried out with a free running and locked MO to which the SL was phaselocked. This was carried out in order to compare the performance and find possible differences. Comparing the power and phase noise spectral densities of the laser beat between a locked and free running MO revealed overall worse values for the locked MO. Since the only difference between the setups are the spectroscopy lock of the MO and the additional external divider, the spectroscopy lock could be the only source of additional noise to the system, since the divider should not affect the rms phase noise according to [99]. Another indicator that the spectroscopy lock was the origin of the additional phase noise was the fact that the characterizing control peak of the spectroscopy lock was visible. It was positioned around $10\,\mathrm{kHz}$ and could therefore not be the control peak of the DPLL, meaning it was imprinted into the loop.
The lasers performance with an active DPLL showed a very promising improvement in comparison with an unlocked laser. The laser's power spectral density values were, as expected, worse then the VCO's, since a laser has a much higher initial line width. With an active DPLL the line width of the laser beat was reduced from $40\,\mathrm{kHz}$ to $50\,\mathrm{Hz}$ for a locked and from $90\,\mathrm{kHz}$ to $70\,\mathrm{Hz}$ for a free running MO. The spot noise showed an improvement with an active phaselock by revealing spot noise values for both laser setups between $-50\,{}^{dBc}/_{\mathrm{Hz}}$ and $-70\,{}^{dBc}/_{\mathrm{Hz}}$ for frequencies between $100\,\mathrm{Hz}$ and $100\,\mathrm{kHz}$ and falling below $-80\,{}^{dBc}/_{\mathrm{Hz}}$ for frequencies above $1\,\mathrm{MHz}$ to the carrier. Spot noise measurements revealed that most of the power of the laser beat was concentrated below $100\,\mathrm{Hz}$ to the peak, which was one of the requirements for successfully executing Rabi pulses for Raman double diffraction assuming a pulse length of $1\,\mathrm{ms}$.
The rms phase noise decreased from $100\,\mathrm{rad}$ to $490\,\mathrm{mrad}$ for a locked and from $950\,\mathrm{rad}$ to $800\,\mathrm{mrad}$ for a free running master laser, which resulted in a calculated phase jitter of $230\,\mathrm{ps}$ for a locked and $360\,\mathrm{ps}$ for a free running MO.
Despite demonstrating promising noise suppression within its control bandwidth, the DPLL ex-

hibited a mean phase noise spectral density in the laser beat that was approximately $40\,{}^{dBc}/_{\mathrm{Hz}}$ higher than that of the NCO. The additional noise originated from the implementation of the I gain, which was also present during the measurements with the electronic VCO. The rounding of the error value in the code resulted in the rounding of small errors to 0, thereby reducing the noise suppression capabilities of the loop. This reduction is evident in both the phase noise spectral density and the rms phase noise. Compared to the characterization with the VCO, the mean noise suppression for the laser setup was $20\,{}^{dBc}/_{\mathrm{Hz}}$ worse, which originated from the higher initial line width of the laser. Therefore, noise could not be as effectively suppressed by the DPLL for the laser as for the VCO.

6.3 Jumping between frequency setpoints

Following the successful demonstration of the DPLL with a laser system at a fixed setpoint, a frequency jump between two setpoints was carried out. During this sequence, the jumping speed of the phaselock was obtained and measured through a frequency to voltage converter, which was inserted in the setup between the external divider and the beat input of the frequency control board as an additional measurement point.

6.3.1 Frequency jumps with the QPort laser system

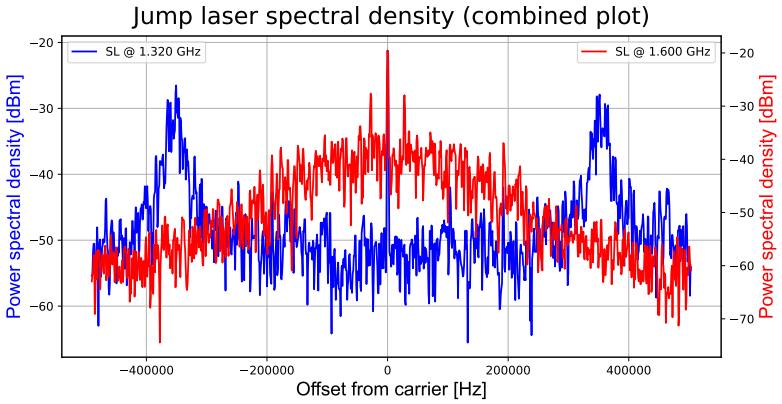

(a)

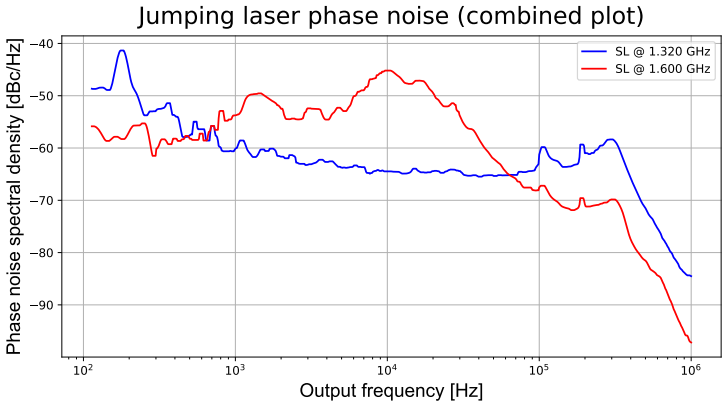

(b)

Figure 6.9: Power and one-sided phase noise spectral density before and after the jumping sequence.

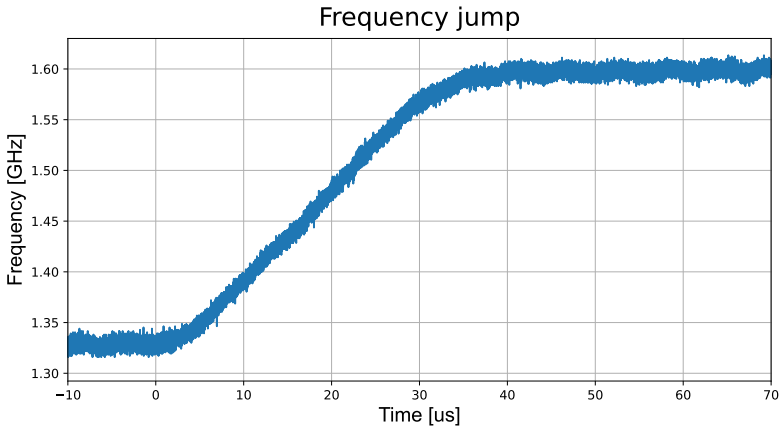

Figure 6.10: Frequency jump with the QPort laser system. The SL laser achieved a $280\,\mathrm{MHz}$ frequency jump from $1.320\,\mathrm{GHz}$ to $1.6\,\mathrm{GHz}$ in about $35\,\mu\mathrm{s}$.

The jumping sequences were measured with the frequency to voltage converter and an oscilloscope at the QPort laser system illustrated in figure 6.5. The evaluation of this measurement showed a jumping speed of $35\,\mu\mathrm{s}$ for a frequency difference of $280\,\mathrm{MHz}$ for SL, which translated to a voltage difference around $46\,\mathrm{mV}$. The different frequencies were a result of the amount of dividers for the separate elements of the loop, since the signal for the NCO was divided by $N = 8$ and the laser beat for the hardware was divided by $N = 4$. A voltage difference of $40\,\mathrm{mV}$ was measured by the frequency to voltage converter for the jump of the beat signals after a division by $N = 4$. The jumping sequence is illustrated in figure 6.10.
Following the measurement of the jumping speed, the phaselocked laser beat was measured with unchanged parameters for the PID filter. The obtained spectral density plots of the laser beat are illustrated in figure 6.9b. The power spectral density plot displayed a FWHM line width of $< 50\,\mathrm{Hz}$ for the carrier at $1.320\,\mathrm{GHz}$ and $90\,\mathrm{Hz}$ for the carrier at $1.6\,\mathrm{GHz}$. For a more precise evaluation of the phaselock quality, the one-sided phase noise spectral density of the laser beat for the two frequency setpoints was measured and illustrated in figure 6.9a. Calculating the rms phase noise for the two setpoints resulted in a value of $490\,\mathrm{mrad}$ for $1.320\,\mathrm{GHz}$ and $2\,\mathrm{rad}$ for $1.6\,\mathrm{GHz}$ by integrating over a bandwidth of $100\,\mathrm{Hz} - 1\,\mathrm{MHz}$.

6.3.2 Frequency jumps with the Berlin laser system

According to the PLL theory in chapter 4, the DPLL with its digital PFD should be able to achieve frequency jumps as far as the current range of the hardware allows. Since the laser system of the QPort system used piezo elements to extend the cavity and had a rather small current tuning range, the jumping performance could not be evaluated for far frequency jumps. For this purpose, a testing environment with ECDLs was required, which supported a wider laser current tuning range. A suitable laser setup was available in the "Humbold Universität zu Berlin" with their developed ECDLs. Since these lasers were also going to be implemented in the MAIUS-B apparatus alongside the DPLL and the developed frequency control board, this testing environment was very suitable.
Lasers in a space limited setup like sounding rockets serve multiple purposes and need to jump between frequency setpoints in limited time frames, as described in chapter 2 and 3. Furthermore, the pulse length of the $\pi/2$ and π pulses during the interferometry sequence set the performance

requirements to the light fields as described in chapter 3.2. Hence, a better characterization of the possible jumping speed of the DPLL as well as the performance quality between two setpoints was necessary.

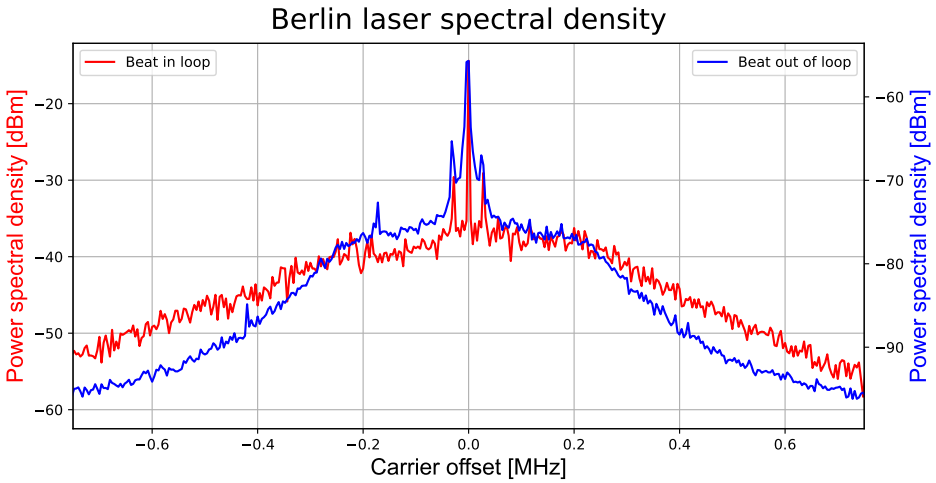

Figure 6.11: Spectral density of the laser beat with the ECDLs from Berlin in loop and after division (red) and out of loop before division (blue). The beat signals had their FWHM at a frequency of $8\,\mathrm{kHz}$ around the carrier in loop and $12\,\mathrm{kHz}$ out of loop with a resolution bandwidth of $1\,\mathrm{kHz}$. The visible peaks around the carrier resulted from the NCO, which imprinted them onto the laser current.

A hardware stack consisting of a laser current driver, the developed frequency control board, a power supply board and an Ethernet communication board was utilized to phaselock a slave ECDL [139] to a master ECDL [140, 141]. The precise measurement setup for the following measurement is illustrated in figure A.13 in the appendix.

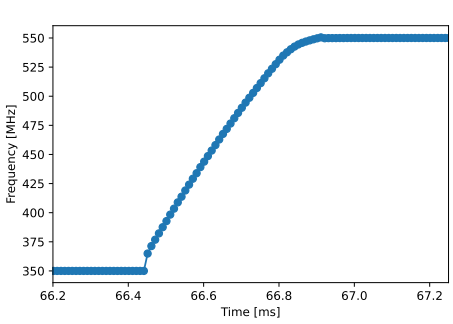

(a)

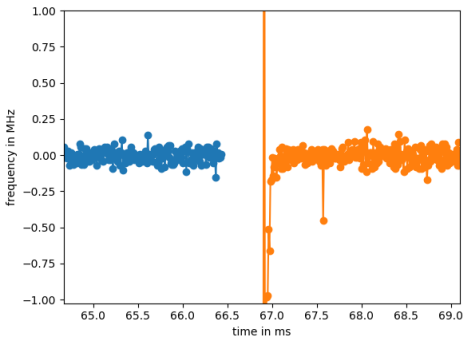

(b)

Figure 6.12: Illustration of the performed jumping sequence over $200\,\mathrm{MHz}$ ($2\,\mathrm{GHz}$ before division) as a function of time. From 6.12a, a settling time of $420\,\mu\mathrm{s}$ was obtained. The frequency deviation is plotted in 6.12b, from which the settling time was also measured to be $420\,\mu\mathrm{s}$.

In this measurement, the beat signal between the two lasers was measured in loop (between the frequency control beat input and the external divider) parallel to an out of loop measurement

with an additional light path to a photo diode with an identical divider. Both external dividers had a factor of $N = 10$. The power spectral density of the two beats with an active DPLL is illustrated in figure 6.11 and showed an almost identical beat signal with a line width of $8\,\mathrm{kHz}$ in loop and about $12\,\mathrm{kHz}$ out of loop around the carrier peak with a resolution bandwidth of $1\,\mathrm{kHz}$.
Succeeding the adjustment of the phaselock parameters, a jumping sequence over $2\,\mathrm{GHz}$ was initiated, which translated to a $200\,\mathrm{MHz}$ jump after a division by $N = 10$ at the beat input of the frequency control board. The jumping sequence is illustrated in figure 6.12a. It showed the measured signal starting to increase in value around $66.4\,\mathrm{ms}$ and settling to a constant value at $66.82\,\mathrm{ms}$ which resulted in a total time of $420\,\mu\mathrm{s}$ to complete the jump. Additionally, the frequency deviation was plotted and is illustrated in figure 6.12b.

6.3.3 Discussion of DPLL results for frequency jumps

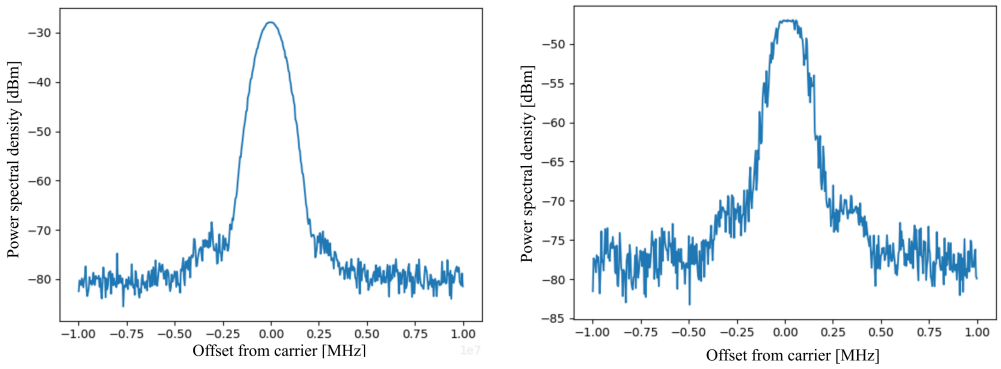

(a) (b)

Figure 6.13: Power spectral density of the Berlin laser before (6.13a) and after (6.13b) the jumping sequence with a RBW of $100\,\mathrm{kHz}$. It is visible that the beat signal of the phaselocked laser is noisier after the jump.

Following the characterization of the DPLL with a laser system, the jumping speed between frequency setpoints of the phaselocked laser needed to be evaluated. The first jumping sequence was carried out with the QPort laser system and revealed a settling time of $40\,\mu\mathrm{s}$ for a $280\,\mathrm{MHz}$ jump. In order to evaluate if the frequency to voltage converter was limiting the measurement, an additional measurement was carried out with a DDS. It revealed, that the jumping time was correctly obtained, since the converter measured a jump of the DDS output (which could jump between frequencies in ns) in under $35\,\mu\mathrm{s}$.
Furthermore, it was visible that the performance got worse when changing the frequency setpoint since the rms phase noise for the laser beat increased from $490\,\mathrm{mrad}$ before the jump to around $1\,\mathrm{rad}$ after the jump was completed.
The frequency of the ECDL slave laser in the QPort laser system was steered through its current by the TBus hardware as well as through its cavity length by piezo elements through additional control hardware already present at the QPort experiment. Since the piezo element could not be adjusted to a compatible TBus board in order to control it simultaneously the jumping sequence was limited by the laser current which translated to a frequency tuning range around $280\,\mathrm{MHz}$ without mode hops. Therefore, an environment was utilized in Berlin with lasers that had a wider mode hop free tuning range accessible to the DPLL. Here it was shown that a $2\,\mathrm{GHz}$ jump could be achieved with the phaselock in a time frame of about $420\,\mu\mathrm{s}$ and that the line width of the laser beat was very similar when measured in loop (about $8\,\mathrm{kHz}$) and out of loop (around $12\,\mathrm{kHz}$).

Similar to the measurements at the QPort experiment for a jumping sequence, the data obtained in this measurement setup displayed that the rms phase noise changed after the jumping sequence to a different setpoint with identical PLL parameters. This could be observed through a comparison of the beat signals' power spectral densities at the initial setpoint and the final setpoint, illustrated in figures 6.13a and 6.13b for the measurement in Berlin and in figures 6.9b and 6.9a for the QPort laser system.
The calculation of the phase error in the code revealed the cause for the worse performance. Since the phase error was a value of the sampling time of the FPGA and the inputted beat and reference signal's frequency, its sampling relation changed for different frequency inputs. Therefore, the PID amplification gains could only be optimized for one frequency setpoint and would lead to an oscillating loop for a lower detuned setpoint and a weak phaselock at a higher detuned setpoint. This needs to be considered for double diffraction sequences, since the DPLL has to be optimized for the most critical frequency, which is the frequency of the Raman transition ω_{eg} with a tolarance of Γ_g as explained in section 3.2.

6.4 Raman double diffraction of a ^{87}Rb BEC with the DPLL

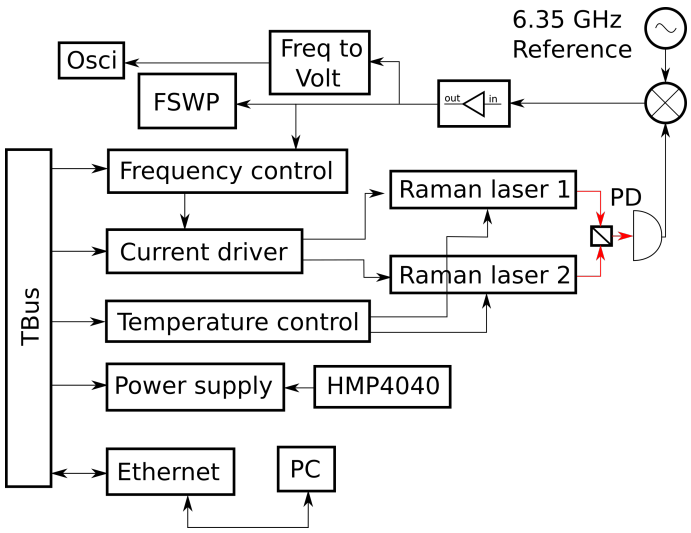

Figure 6.14: Setup of the Raman lasers and electronics system utilized for the measurements at the MAIUS-B physics package using the ground laser system. Compared to the earlier setup at the QPort experiment (figure 6.5), the laser beat is mixed with a $6.35\,\mathrm{GHz}$ microwave signal to scale down the frequency instead of using additional external dividers.

This section presents the realization of a Mach-Zehnder interferometer (MZI) with Raman double diffraction using the DPLL. The Raman laser system was set up by controlling the beat signal between the cooling laser for the 2D-MOT (Raman laser 1) and the laser used for the repumping transition (Raman laser 2) (see chapter 2 for the transitions). Raman laser 2 was phaselocked by the DPLL beforehand to the Raman transition frequency. The first Raman laser jumped to the frequency of the $|F=2\rangle \rightarrow |i\rangle \rightarrow |F=1\rangle$ transition after the ARP sequence, driven with a set detuning of $\Delta \approx 1\,\mathrm{GHz}$. Subsequently, the second Raman laser needed to follow within a limited time frame to set up the light field as well as achieving the accuracy described in section 3.2.
The following measurements were carried out and are described in the next sections:

(i) optimization of the phaselock's loop filter parameters for the frequency setpoints of the Raman transition in regards to jumping speed and rms phase noise

(ii) tuning of the beam splitter and mirror pulses in their pulse length and intensity for Raman double diffraction of ^{87}Rb

(iii) optimization for maximum diffraction efficiency of the BEC into the $\pm|2\hbar k\rangle$ momentum states from the initial state $|0\rangle$ by scanning the Rabi oscillation of the Raman transition

(iv) combination to an interferometer with a free evolution time T, which was set to an operating point beforehand

(v) intentional tilt of the apparatus in order to measure the tilt through the atoms populating the ground and excited states after the interferometry sequence, calculated by measuring the population of the excited states as a function of the free evolution time T

The measurements were accomplished using the second generation of the laser frequency controller and third generation of the laser current driver in the MAIUS-B ground laser system. The flight physics package for MAIUS-B was used as a source for BECs. A detailed description of the systems can be found in [38, 131, 137].

6.4.1 Experimental setup

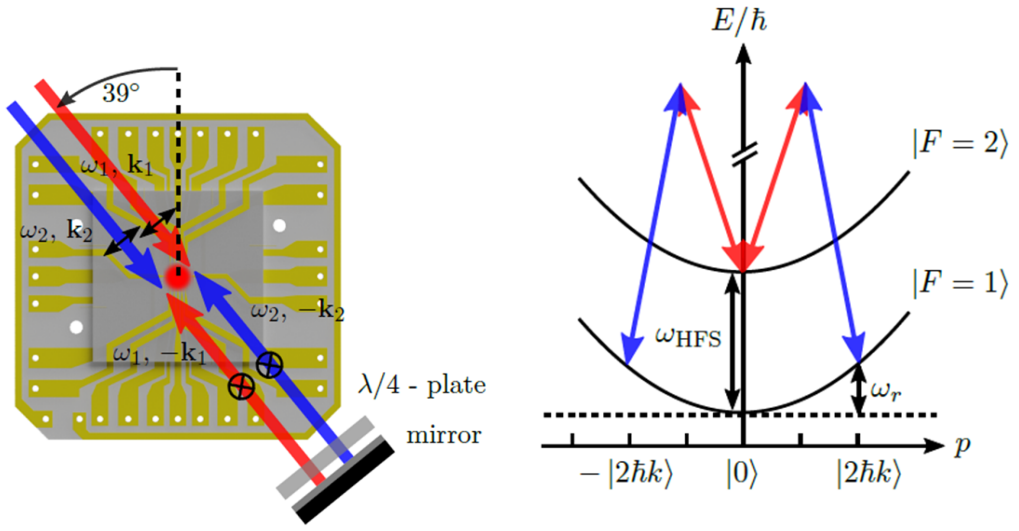

(a) (b)

Figure 6.15: Illustration of the light fields used for Raman double diffraction in the following measurements. The light fields were set up so that they were co-propagating which is shown by the pairs $(\omega_1, k_1), (\omega_2, -k_2)$ and $(\omega_2, k_2), (\omega_1, -k_1)$ in 6.15a. They enabled the atoms in the initial momentum state $|0\rangle$ to be transferred into both momentum states $\pm|2\hbar k\rangle$ (shown in 6.15b) and absorb the momentum $k_1 + k_2$ of the light field, so that they were inertial sensitive, which was described in section 3.1.3 [4, 5].

The lasers of the MAIUS-B ground system were ECDLs whose frequencies were controlled through their laser current as well as through their cavity length by a piezo controller. The implemented electronic boards are part of the TBus standard, although they belonged to an older iteration. Since the newer iteration of the boards used for the previous measurements included design changes, which were not relevant for these measurements, the results were comparable. Following these measurements, the DPLL code was updated as well. However, the results can be

compared too, since the latest version of the phaselock used in earlier sections for the characterization showed an improved performance regarding rms phase noise and noise suppression.
The light fields created by the lasers were fed into optical fibers in a crossed polarization formation, which translated to a $\sigma^+\sigma^-$ overlapping light field in the interferometry chamber. This light beam setup represented an alternative beam setup to the Lin||Lin configuration, which is explained in detail here [142]. Furthermore, the light fields were setup in order to transfer a high momentum of $k_1 + k_2$ to the atoms, making them inertial sensitive, as described in section 3.1.3. The light fields are illustrated in figure 6.15a.
Showing the possibility of Raman double diffraction with the DPLL was one of the goals of this thesis. The lasers used for the interferometry sequences were the cooling laser for the 2D-MOT (MO, Raman laser 1) and the laser responsible for the repumping transition (SL, Raman laser 2). The Raman transition $|F = 2\rangle \rightarrow |i\rangle \rightarrow |F = 1\rangle$ was carried out with a detuning $\Delta \approx 1\,\mathrm{GHz}$ between $|i\rangle$ and F' as described in chapter 3.1.3 and $\omega_{eg} = 6.8347\,\mathrm{GHz}$ for the Raman transition. The MO jumped to ω_{eg} after the ARP was completed (described in chapter 2) and the SL, which was phaselocked by the DPLL needed to follow in a limited time frame of $\leq 1\,\mathrm{ms}$. The Rabi pulses needed to be optimized towards diffraction efficiency into the excited states.
The electronic system setup is illustrated in figure 6.14 and was different to the previous setup at the QPort experiment. The addition of the $6.35\,\mathrm{GHz}$ mixing signal achieved laser beat frequencies processable for the frequency control board without the addition of external dividers. Furthermore, the piezo element was also steered simultaneously by an additional digital PID in the frequency control board during these sequences to achieve far frequency jumps.
The line width of the ground state Γ_g, which depended on the pulse duration $\tau_{BS,M}$ of the beam splitter and mirror (as described in section 3.2), was the crucial parameter during this sequence. The pulse lengths were set to $\tau_{BS} = 20\,\mu\mathrm{s}, \tau_M = 40\,\mu\mathrm{s}$ during these sequences and the free evolution time was set to $T = 1\,\mathrm{ms}$.

6.4.2 Optimization of the DPLL for the interferometry sequences

Earlier described measurements of frequency jumps had shown that the loop filter parameters for the gains would need an adjustment to the different frequency setpoints during the interferometry sequences (see section 6.3). Since on-the-flight changing of PID parameters was not achievable with the DPLL, the optimization focus for the parameters was the transition frequency after external division. The DPLL setpoint for the beat signal between Raman laser 1 & 2 lied at $\omega_{eg} = 484.03\,\mathrm{MHz}$ following a jump from a starting frequency of $\omega_{pre} = 218.03\,\mathrm{MHz}$, which was the frequency of the beat signal for the two lasers during laser cooling. These frequency setpoints were the result of the mixed signal between the laser beat and the $6.35\,\mathrm{GHz}$ microwave reference. The cooling and the repump frequency of ^{87}Rb are $266\,\mathrm{MHz}$ apart. By mixing $\omega_{eg} = 6.834\,\mathrm{GHz}$ with the $6.35\,\mathrm{GHz}$ signal, the resulting frequency for cooling sequences is ω_{pre} and the frequency for the Raman transition is ω_{eg}. The beat frequencies for the sequences are shown in table 6.3.
The one-sided phase noise spectral density measurements of the phaselocked laser beat at ω_{eg} and ω_{pre} is illustrated in figure 6.16 which resulted in a rms phase noise of $710\,\mathrm{mrad}$ for ω_{eg} and $900\,\mathrm{mrad}$ for ω_{pre} integrated over a bandwidth of $10\,\mathrm{Hz} - 10\,\mathrm{MHz}$.

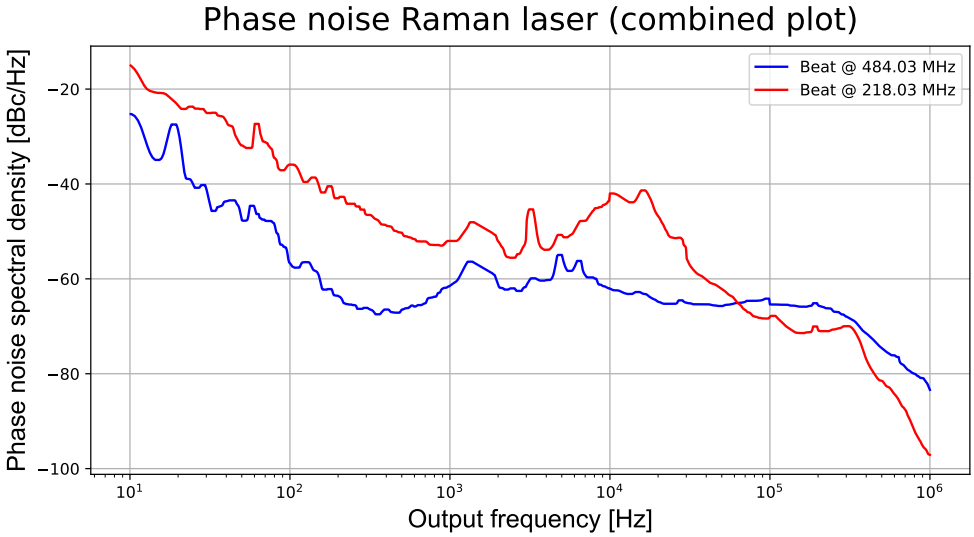

Figure 6.16: One-sided phase noise spectral density of the laser beat between Raman laser 1 and Raman laser 2 with a bandwidth of $10\,\mathrm{Hz} - 10\,\mathrm{MHz}$. Raman laser 2 was phaselocked to a beat frequency of $\omega_{pre} = 218.03\,\mathrm{MHz}$ during laser cooling prior to the interferometry sequence (blue). Laser 1 jumped to the Raman transition and laser 2 needed to follow in $\leq 1\,\mathrm{ms}$ to set up the light fields. The loop filter parameters were therefore optimized for a fast frequency jump to reach $\omega_{eg} = 484.03\,\mathrm{MHz}$ (red). The rms phase noise was optimized for ω_{eg} to $710\,\mathrm{mrad}$ close to the critical gain. $900\,\mathrm{mrad}$ was the rms phase noise of ω_{pre}.

The population probability of Raman double diffraction depends on the light field intensity and the pulse duration, which was shown through equation 3.7 in chapter 3. Since Raman laser 2 needed to follow Raman laser 1 in order to setup the light fields for the sequence in $\leq 1\,\mathrm{ms}$, the phaselock needed to be adjusted accordingly whilst maintaining a low rms phase noise to drive the Rabi oscillation as efficient as possible. Therefore, the jumping speed between the frequency setpoints needed to be as fast as possible without surpassing the critical gain of the DPLL and creating oscillations of the loop. Hence, the phaselock's loop filter parameters were set to achieve a jumping time of $\leq 1\,\mathrm{ms}$. Additional to the laser current, the PID controller for the piezo was set to a high P and I gain in order to achieve the far frequency jump within the time limit of $\leq 1\,\mathrm{ms}$, since the laser current tuning range was insufficient for the frequency jump of this sequence. The PID parameters were set to:

- proportional gain $P = 410$
- integral gain $I = 18$
- derivative gain $D = -70$
- internal divider $N = 16$

Succeeding the adjustment of the phaselock parameters for the Raman transition, the setup of the MZI began.

Table 6.3: Beat frequencies before and during the interferometry sequence of the lasers used for the Raman transition. After being mixed with the $6.35\,\mathrm{GHz}$ microwave signal, the laser beat signal had the value of the mixed frequency, which was read out by the laser frequency control board after amplification.

Beat between	Value	Frequency in GHz	DPLL setpoint in MHz
Cooler & Repumper	ω_{pre}	6.568	218.03
Raman 1 & Raman 2	ω_{eg}	6.835	484.03

6.4.3 Tuning of beam splitter and mirror pulses

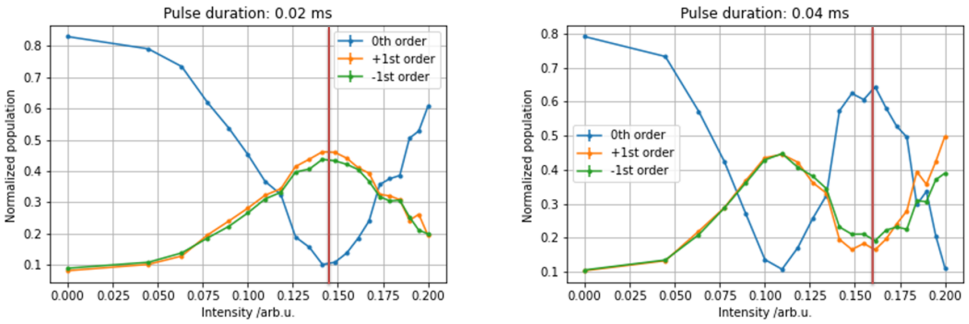

(a) (b)

Figure 6.17: Light beam intensity in arbitrary units for the beam splitter 6.17a and the mirror pulse 6.17b as a function of the normalized population of the ground and excited states. The blue curve illustrates the population of the ground state, the orange and green curve illustrate the population of the two excited states. The pulse duration for the beam splitter was $20\,\mu s$ and for the mirror $40\,\mu s$. The intensities for the pulses were found at the red lines, which represent the light beam intensity steered through the current of the AOMs in the path.

A MZI with a free evolution time of $T = 1\,\mathrm{ms}$ was aimed at during these measurement sequences. The beam splitter and mirror pulses were also set to a fixed pulse duration of $\tau_{BS} = 20\,\mu s$ and $\tau_M = 40\,\mu s$. In order to achieve those pulses with an optimal diffraction efficiency, the beam splitter and mirror pulses required to be scanned as a function of the light field intensity. The light field intensity was controlled with an acousto-optic modulator (AOM) which steered the intensity as a function of the inputted RF signal amplitude, that was created by the TBus DDS card [30]. The arbitrary units in the graph represented the values, which could be entered as the amplitude of the RF signal and created an amplitude modulation in the AOM.

The light power of the light fields in the interferometry fiber amounted to $0.7\,\mathrm{mW}$ for the SL and $1\,\mathrm{mW}$ for the MO with a deviation of $\pm 0.05\,\mathrm{mW}$. The ratio between the two light fields was $^{slave}/_{master} = 1.7$ in order to compensate the AC-Stark shift of the transition states, which is explained in section 3.2.

Starting with the first beam splitter, the light field intensity was scanned and is illustrated in graph 6.17a. The purpose of scanning the Rabi oscillation over the light beam intensity was to find the value where the most atoms where diffracted into the two excited states, prior to

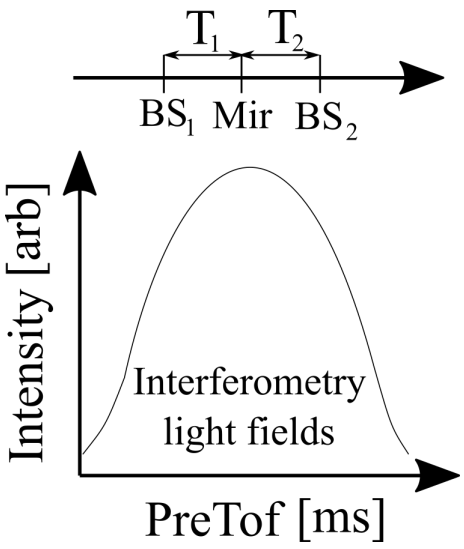

Figure 6.18: Graphic illustration of the definition of PreTof. The interferometry light fields of Raman laser 1 & 2 had a Gaussian intensity profile. PreTof was defined as the time before the ensemble fell out of the interferometry light fields ("pre time of flight"). During the interferometry measurements, the mirror (Mir) was aimed to be timed at the middle of the PreTof, which lied at the intensity maximum of the light fields. This moment in time was chosen in order to enable the longest possible free fall times $T_{1,2}$ and the beam splitters ($BS_{1,2}$) were adjusted accordingly.

being transferred back. The scan began at a time $5\,\mathrm{ms}$ PreToF, which was defined as the time prior to the ensemble falling out of the light fields of Raman laser 1 & 2. The definition of PreTof is illustrated graphically in figure 6.18. The results showed a maximum diffraction for a DDS amplitude of $0.077\,\mathrm{arb}$, where an efficiency of $97\,\%$ was measured.
Following the intensity scan of the first beam splitter pulse, the intensity for the mirror pulse and the second beam splitter pulse was carried out. During this measurement, the Doppler shift δ_{Dop} of the atoms towards the light field due to the momentum absorption of the first pulse and the gravity acceleration needed to be compensated by adjusting the DDS frequency.
The intensity scan for the mirror pulse is illustrated in graph 6.17b. For a pulse duration of $40\,\mu\mathrm{s}$, the DDS amplitude of $0.08\,\mathrm{arb}$ showed where most of the atoms went through half a Rabi oscillation period, thus indicating the intensity value of the light fields for the mirror pulse with an efficiency of $79\,\%$.
A similar procedure was carried out for the second beam splitter pulse. In comparison to the first pulse, the Doppler shift δ_{Dop} needed to be compensated. The optimal intensity for the second beam splitter pulse was at an amplitude of $0.071\,\mathrm{arb}$ with a diffraction efficiency of $93\,\%$.

6.4.4 Interferometry sequence

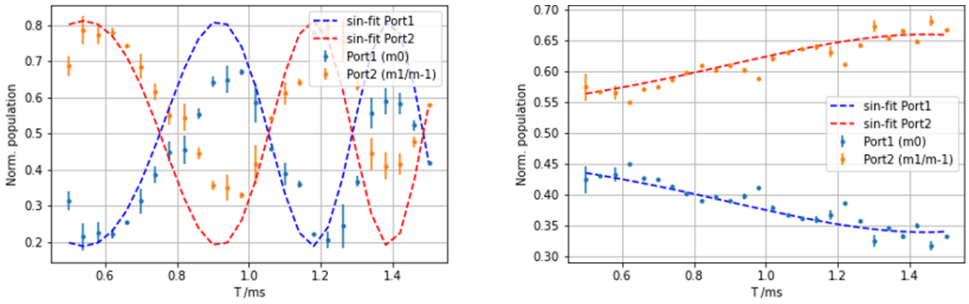

(a) (b)

Figure 6.19: Interferometry sequence with a fit for a sine wave with an increasing frequency for the ground state (red) and the excited states (red). During these measurements, the apparatus was once tilted by an angle $\phi = 0.29\,^\circ$ (figure 6.19a) and later by an angle $\phi = 0.84\,^\circ$ (figure 6.19b). In order to obtain the tilt angle by measuring the population of the excited states, the free evolution time T was scanned from $0.5\,\mathrm{s}$ to $1.5\,\mathrm{s}$ by changing the timing of the beam splitters illustrated in figure 6.18. Illustrating the population as a function of T was an accelerated sine wave, which equation 6.1 showed.

Using the pulse settings obtained from the intensity scans of the beam splitters and the mirror in addition to the tuning of the loop filter parameters of the phaselock for jumping speed, accuracy and rms phase noise, a MZI setup with Double Raman diffraction was tested. A free evolution time of $1\,\mathrm{ms}$ was chosen. T_1 between the first beam splitter and mirror pulse and T_2 between the mirror and second beam splitter pulse were set equal $T_1 = T_2 = T$. The complete sequence consisted therefore of:

- beam splitter pulse with a duration of $20\,\mu\mathrm{s}$ and a light field intensity of $0.077\,\mathrm{arb}$ resulting in a diffraction efficiency of $97\,\%$
- $1\,\mathrm{ms}$ of free evolution time T_1
- mirror pulse with a duration of $40\,\mu\mathrm{s}$ and a light field intensity of $0.08\,\mathrm{arb}$ and an efficiency of $79\,\%$

- $1\,\mathrm{ms}$ of free evolution time T_2
- beam splitter pulse with a duration of $20\,\mu\mathrm{s}$ and a light field intensity of $0.071\,\mathrm{arb}$ resulting in a diffraction efficiency of $93\,\%$ and closing the interferometer.

The acceleration due to the earths gravitation $\Phi_{acc,g}$ would not add a phase difference to the diffracted atomic ensembles, if the laser beams were aligned perpendicular to the earths acceleration. Therefore, the physics package was tilted intentionally, in order to measure the tilt by the population difference between the states. It is illustrated by the tilt of the atom chip towards $\vec{g}$ in figure 6.20.

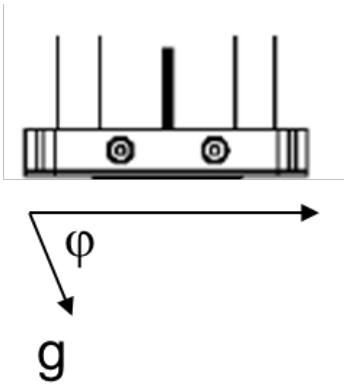

Figure 6.20: Illustration of the angle ϕ, by which the apparatus was tilted intentionally so that it was measurable through the MZI sequence. The atom chip in the 3D-chipMOT chamber represents the whole physics package in this figure, which was described in chapter 2.

Since the acceleration phase 1.2 is defined as a function of T^2, the probability to find an atom in the ground state changed from equation 3.9 to:

$$P(|\pm 1\rangle) = sin(sin(\frac{\phi}{360^\circ} \cdot 2\pi) \cdot |g| \cdot T^2). \tag{6.1}$$

Outlining the population of the states (equation 3.6) as a function of the free evolution time therefore led to an accelerated sine wave. The results of the MZI sequence are illustrated in figure 6.19a for a tilt of $\phi = 0.84^\circ$ and in figure 6.19b for a tilt of $\phi = 0.29^\circ$ with the blue curve representing the atoms in the ground state $|g\rangle$ and the red curve the atoms in the excited states $\pm|e\rangle$. This confirmed the successful realization of Raman double diffraction and a MZI with the DPLL.

6.4.5 Subsequent adjustments

Through evaluation of the population of the $\pm$1st order states at different free fall times for the PreToF, the diffraction into the two excited states revealed to be asymmetrical, which can be seen in graph 6.21a and 6.21b with the intentional tilt of the apparatus being 0. The graphs illustrate the population of the states as a function of the detuning of the Raman laser 2 frequency around the carrier ω_{eg}. This led to the conclusion, that an additional tilt of the apparatus towards a different spatial direction introduced an acceleration to the atomic ensemble. An angle of $\neq 0$ led to a detuning difference between the two interferometer arms and therefore a different population probability of the states. The unintentional acceleration was corrected by comparison of the

population of the excited states at PreTof $2\,\mathrm{ms}$ and $10\,\mathrm{ms}$ whilst tilting the apparatus until both scans where symmetrical.

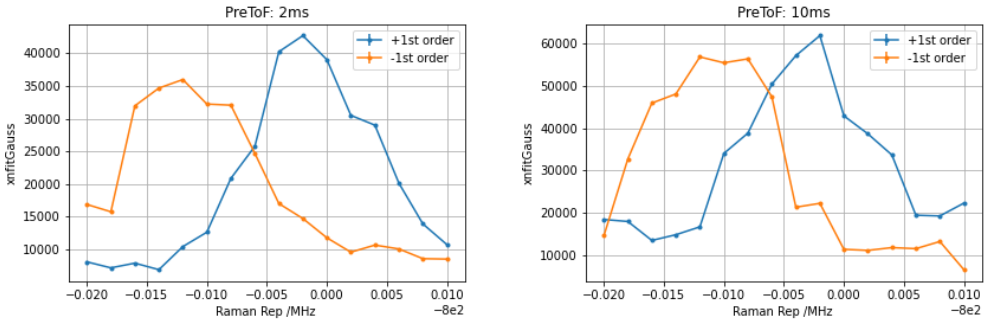

(a) (b)

Figure 6.21: Frequency scan of population around Raman detuning for Pretof $2\,\mathrm{ms}$ 6.21a and $10\,\mathrm{ms}$ 6.21b before adjusting the apparatus tilt and DKC.

Furthermore, the scans showed a different frequency detuning for the maximum diffraction of the two states which suggested an initial non-zero velocity of the atoms towards the light beams' direction, which led to different detunings to reach the two momentum states. The reason for the leftover velocity of the atomic ensemble suggested, that the DKC required optimization, since it was the final sequence prior to the interferometry sequence. Following the adjustment for DKC, the PreTof scans for $2\,\mathrm{ms}$ and $10\,\mathrm{ms}$ as a function of the detuning were repeated and showed the symmetrical diffraction into the two states illustrated in graphs 6.22a and 6.22b.

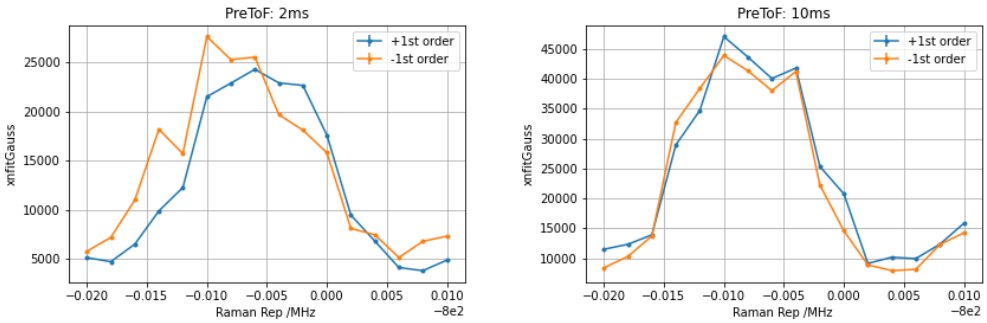

(a) (b)

Figure 6.22: Frequency scan of population around the Raman detuning for Pretof $2\,\mathrm{ms}$ 6.22a and $10\,\mathrm{ms}$ after an adjusted apparatus tilt and DKC.

Ultimately, a measurement was carried out to observe Rabi oscillations for a longer pulse duration of $60\,\mu\mathrm{s}$ and higher light beam intensity. The measurement is illustrated in figure 6.23. The Rabi oscillation for longer durations and a higher light beam intensity revealed a higher damping of the oscillation.

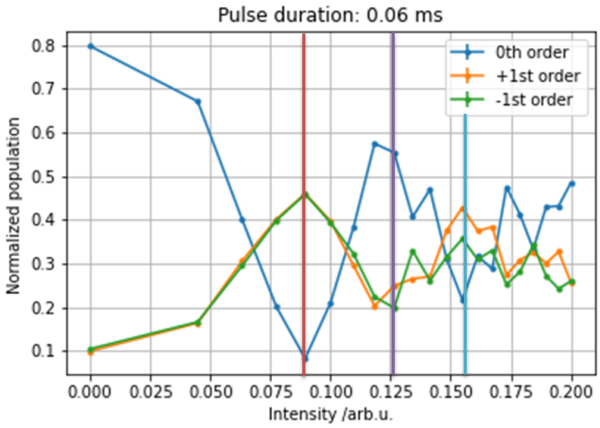

Figure 6.23: Illustration of the Rabi oscillation with a longer pulse duration of $60\,\mu s$ and higher light beam intensity. A second Rabi cycle is visible but with damping.

6.4.6 Discussion of DPLL results for interferometry with Raman double diffraction

The measurements in this section presented the successful realization of a MZI with Raman double diffraction using the DPLL. The chosen experiment was the ground laser system and flight physics package of the neighboring MAIUS-B experiment. Since the ground laser system was already using the TBus standardized hardware (with older iterations of the laser frequency control board and laser current driver), the setup of the phaselock was achieved in less than a day. The first Raman laser was locked to the ^{87}Rb D_2 transition with a detuning of $\Delta = 1\,\mathrm{GHz}$ to the F' states, hence the intermediate state $|i\rangle$. The second Raman laser was phaselocked by the DPLL to the first laser with a frequency difference of ω_{eg} to achieve the $|F=2\rangle \rightarrow |i\rangle \rightarrow |F=1\rangle$ transition. The detuning δ consisting of the Doppler detuning δ_{Dop}, recoil shift δ_r and AC-Stark shift δ_{ac} were calculated beforehand by the experimental staff and compensated by the frequency setpoint of the laser beat and laser intensity relation between the two Raman lasers.
The chosen setpoint for the second Raman laser was at a beat frequency of $\omega_{eg} = 484.03\,\mathrm{MHz}$ between Raman laser 1 & 2, mixed with the $6.35\,\mathrm{GHz}$ microwave reference. The DPLL needed to achieve the jumping sequence to ω_{eg} from a previous setpoint of $\omega_{pre} = 218.03\,\mathrm{MHz}$ during laser cooling within a time frame of $\leq 1\,\mathrm{ms}$. ω_{eg} set the requirements to the phaselock as well as the pulse duration. Since it was chosen to be $\tau_{BS} = 20\,\mu s, \tau_M = 40\,\mu s$, the requirements to the phaselock were set by the line broadening of the pulse duration. The line width of the laser beat had to be below $\Gamma_g = 1\,\mathrm{kHz}$ around the carrier for the chosen pulse durations $\tau_{BS,M}$. The DPLL was therefore optimized to the setpoint ω_{eg}, which resulted in an oscillation of the PLL at ω_{pre}, which was neither relevant for the interferometry sequence nor for the laser cooling sequences. Subsequent to the setup of the PLL to the setpoints, intensity scans of the Raman transition were conducted to find the optimal intensity for τ_{BS} were the atoms of the ensemble were in a superposition between the two momentum states $\pm|2\hbar k\rangle$ and the initial state $|0\rangle$ was almost unpopulated. Afterwards, the same measurement was carried out to find the intensity for the mirror pulse τ_M. During these measurements, the DDS frequency controlling the AOMs was adjusted to compensate the Doppler shift. Lastly, the second beam splitter pulse was examined in a similar way as the first two intensity scans. The measurements showed a diffraction efficiency of $\approx 97\,\%$ for the first beam splitter pulse, $\approx 79\,\%$ for the mirror pulse and $\approx 93\,\%$ for the second beam splitter pulse with an optimized DPLL to ω_{eg}.

Ultimately, a MZI setup was conducted with the previously obtained intensity scans and PLL optimization. Since the AI, without adding an intentional phase difference, would show a total phase difference of $\delta\Phi = 0$ through detection of the state population, an intentional apparatus tilt was introduced for two angle settings. The tilt of the apparatus was measured to be $\phi = 0.84\,^\circ$ in the first and $\phi = 0.29\,^\circ$ in the second measurement. Those angles were calculated by the population of the excited states after the interferometry sequence.
The diffraction into the two momentum states turned out to be asymmetric, whose cause was a leftover momentum of the atoms due to the prior DKC sequence. The damping visible in the interferometry sequence and the additional measurement of the Rabi oscillation for a longer pulse duration of $60\,\mu\mathrm{s}$ and a higher light beam intensity was either the result of the chosen setpoint for Raman laser 2, which was not exactly at the transition frequency ω_{eg} or it was the result of the rms phase noise of the laser.
Since the laser phase noise in double diffraction does not have an impact to the interferometry sequence according to theory in the first order, it can only affect the beam splitter or mirror pulses by losing enough power during the light pulses. Since the beam splitters had an efficiency of over $90\,\%$ and the mirror pulse an efficiency around $80\,\%$, the more probable cause would be a slightly wrong frequency setpoint for the interferometry sequence. Since the mirror had double the pulse length of the beam splitters, the line width broadening of the pulse was half compared to the beam splitters. If the setpoint frequency was sufficiently close, so that most of the laser power was within the relevant frequency span for the transition during the beam splitters, it might have been slightly wrong for the mirror. For an identical light field intensity this would result in a reduced diffraction efficiency of the mirror pulse, which was measured, since the efficiency dropped by more than $10\,\%$ compared to the beam splitters. Unfortunately, this could not be investigated further, since the laser system failed shortly after these measurements were conducted. Nevertheless, a successful demonstration of Raman double diffraction with the developed DPLL was performed during this thesis.

CHAPTER 7

Outlook

This thesis presents the realization of a digital phase locked loop (DPLL) for the usage in atom interferometry. The phaselock was integrated into the current version of the TBus Laser Frequency controller, which was developed during this work.
As a main advantage, the DPLL can be employed fast to enable double Raman processes for different laser systems. In this thesis two standard lasers could be phaselocked to each other by simply connecting them to a TBus stack consisting of the laser frequency controller, current driver, power supply and communication board. After a fast adjustment of the laser current and the PID parameters, the laser beat could be phaselocked at the desired frequency setpoint.
The performance of the DPLL was evaluated by its phase noise suppression. The rms phase noise for the laser systems was measured between $400\,\mathrm{mrad}$ and $800\,\mathrm{mrad}$ for a frequency span from $100\,\mathrm{Hz}$ to $1\,\mathrm{MHz}$ in addition to spot noise measurements at every decade. They revealed rising phase noise values of $\approx 20\,{}^{dBc}/_{\mathrm{Hz}}$ between $100\,\mathrm{Hz}$ and $1\,\mathrm{kHz}$ of the NCO reference, whose origin was the $10\,\mathrm{MHz}$ reference oscillator from the TBus stack. The spot noise difference of $\approx 20\,{}^{dBc}/_{\mathrm{Hz}}$ between the reference oscillator, the NCO and the phaselocked laser beat observable at $100\,\mathrm{Hz}$ was added by the internal FPGA PLL [123], since the reference oscillator passed one FPGA before the measurement and the NCO and laser beat passed a second FPGA before being measured.
The phase noise difference of $\approx 40\,{}^{dBc}/_{\mathrm{Hz}}$ between the NCO signal and the laser beat was a result of the integral gain realization in the PID code, which could be observed by comparing the phase noise plots between the signals in figure 6.8. Since the successful implementation demanded a reduction of the error signal for the I gain calculation, the integral part of the PID rounded down the phase error values between the laser beat and the NCO for the calculation. As a result, small error values were rounded to 0 for the integral gain and the phase noise suppression was reduced in the process.
Fast frequency jumps between different setpoints were also a requirement to the DPLL, since they enable the reduction of lasers needed for different experimental sequences. The phaselock achieved a jumping time of $420\,\mu\mathrm{s}$ for a frequency jump of $2\,\mathrm{GHz}$ and $35\,\mu\mathrm{s}$ for $280\,\mathrm{MHz}$. This jumping time was sufficiently short in order to use the laser addressing the repumping transition also to drive the Raman transitions. The PID parameters needed to be adjusted to fixed values corresponding to a specific setpoint, since they change for different setpoints when they are far apart.

The realization of an atom interferometer started by tuning the light field intensity for the beam splitter and mirror pulses. Following the calculation of the laser frequencies by including the detuning from the Doppler shift, the recoil shift and the AC-Stark shift, the DPLL was locked to the calculated setpoint. Since the lasers addressing the ^{87}Rb repumping transition where also used to drive the Raman transition, the DPLL was optimized for a low jumping time between the frequency setpoints. Performing a frequency jump there is always a trade off between shortening the time of the jump and keeping a narrow linewidth with low phase noise. Since double diffraction techniques are not affected by the phase noise in the first order a low jumping time was preferred.

Therefore the DPLL parameters were chosen to favor a fast frequency jump. The frequency jump is performed between the setpoint for laser cooling $\omega_{pre} = 218.03\,\mathrm{MHz}$ and the setpoint for the Raman transition $\omega_{eg} = 484.03\,\mathrm{MHz}$. A low jumping time for the laser was achieved by increasing the I gain as high as possible at the frequency setpoint which drove the Raman transition. Since the length of the beam splitters and mirror pulses set the requirements to the linewidth of the lasers, the loop filter parameters were optimized for ω_2. This led to a phaselocked laser close to the critical gain, which resulted in an oscillating loop at ω_1. As explained earlier the requirements for laser cooling where less critical than for Raman double diffraction, which was the reason for the optimization to the setpoint at ω_2.
This thesis successfully demonstrated coherent splitting and reflection of a BEC with the described laser system. Whilst measuring longer pulses for the Rabi oscillation, a damping was measured. This damping was visible in the mirror pulse already, were the efficiency went down more than $10\,\%$ compared to beam splitter pulses. This damping could be explained either by the rms phase noise of the phaselock or by a slightly wrong frequency setpoint of the light fields. Since phase noise does eventually lead to frequency noise which can produce a damped Rabi oscillation, the frequency fluctuations should have already influenced the beam splitter pulses visibly. Therefore, the more probable explanation was a slightly wrong frequency setpoint of the light fields. However, with a laser phase noise of $400\,\mathrm{mrad}$ to $800\,\mathrm{mrad}$, double diffraction was still achieved.
Lastly, an interferometry sequence with the adjusted mirror and beam splitter pulses was executed, to measure an intentional tilt of the MAIUS-B apparatus, which demonstrated that an AI was realized with the developed DPLL.
Comparing the developed phaselock model with state of the art optical PLLs shows, that the performance cannot hold up against highly optimized systems [100, 143, 144]. Interferometers, which use double diffraction techniques as well, have shown Rabi oscillations with less damping [20, 145]. Established Raman laser systems with analog or hybrid PLLs reach a suppression of phase noise spectral densities inside their control bandwidth down to a level of $\approx -110\,{}^{dBc}/_{\mathrm{Hz}}$ with a control bandwidth around $3.5\,\mathrm{MHz}$ [146]. Using ECDLs whose initial natural linewidth is even narrower, between $10\,\mathrm{kHz}$ and $20\,\mathrm{kHz}$ [147], also increases the performance of the Raman system. All these systems require a high amount of work and time to be optimized, but are superior to the developed DPLL.
Nevertheless, the setup time of the DPLL to a laser system and the fast optimization to different frequency setpoints due to its digital nature introduces other advantages. For small space applications, e.g. micro satellites, a digital system is very favorable, since parameters of the loop can be adjusted without soldering and with a communication from far away. Furthermore, the digitally tunable NCO reference, even though it is inferior to other reference signals, enables tuning setpoints as high as the laser current tuning range accessible by the DPLL code which can be from $100\,\mathrm{MHz}$ up to $2\,\mathrm{GHz}$, without counting in external dividers. Additionally, already existing laser systems can use the developed phaselock to increase their performance with little effort. For high precision space applications, the DPLL needs further improvement in regards to phase noise suppression and control bandwidth to compete with other systems. Due to its digital nature, it would surpass analog or hybrid PLLs in space applications once the improvements are realized.

Atom interferometers have grown in importance during the last decades in various fields of research. Especially orbit based inertial sensors are a goal for earth science exploration and fundamental physical research. In order to realize drop tower and sounding rocket based experiments like the missions of the QUANTUS family to achieve longer free evolution times, smaller, lighter and more efficient control electronics are indispensable. The DPLL developed in this thesis presents a great leap towards this goal. It not only reduces the amount of electronics necessary for laser locks, so that smaller apparatuses that will be needed for orbital missions can soon become

feasible, it also greatly improves the workflow in the laboratory, by dramatically easing down the integration of a new laser into the test system. It also allows a more dynamic use of a single laser, that can easily be applied and locked to a new target frequency without replacing analog components. Beyond the planned application of this phaselock during the MAIUS-B mission on a sounding rocket and the BECCAL mission on the ISS it represents a level of miniaturization and efficiency that can potentially be applied in micro satellite or free flying missions.
There are several ways of improving the current DPLL model. The first logical step would be improving the DPLL can be achieved by the implementation of a higher order loop filter. Such a filter can potentially surpass the phase noise suppression and the control bandwidth of the existing filter. Such a higher order loop filter is challenging with the current FPGA compiler. Since this thesis represents the first iteration of the phaselock working with atomic ensembles, this feature was out of scope.
Another way to increase the phaselock performance can potentially be realized based on the data this thesis provides by optimizing the loop parameters to the results. Furthermore, other phaselock optimizing techniques which are already realized and characterized in analog phaselocks [97, 102] can be realized digitally and can potentially enhance the performance of the DPLL further.
It was noticed during this thesis that the parameters for the loop filter did not fit perfectly during a jumping sequence between two far off frequency setpoints. An enhancement in order to bypass the adjustment of the PID parameters manually, a second internal loop could be implemented to adjust the setpoints automatically. This can be realized by including a direct phase noise measurement in the phaselock program, which the second loop would use as a reference for optimizing the loop filter parameters. The optimal values for the PID could then be saved in an internal storage for multiple setpoints chosen by the user. For dynamic frequency jumps or sweeps, controlling the parameters could be realized by using more advanced algorithms, which could surpass common laser phaselocks in regards to their flexibility for frequency setpoints and tuning range.

Due to the digital nature the DPLL does not consume additional space in a hardware setup and is also more efficient compared to analog or hybrid PLLs since it is implemented on a FPGA. With these characteristics and the aforementioned improvements, the shown DPLL can potentially enable DFB diode lasers to be used for atom interferometry which can potentially make them feasible on micro satellites. With two lasers, the presented DPLL could enable the realization of an interferometer, which is capable of achieving Raman diffraction with cold atoms in a highly space limited environment such as a CubeSat. By realizing such a small AI in regards to space, efficiency, weight and cost, a new threshold would be set for the realization of atom interferometers in space. This thesis presents the very first all digital phaselock designed for atom interferometry that is of an efficiency level to be used in future orbital missions. The system was successfully tested with ECDL lasers from Berlin, at the QPort laser system and at the MAIUS-B system. The data gathered during these tests lays the foundation for further improvements for this technique which can potentially enable interferometry on micro satellites.

APPENDIX A

Appendix

A.1 ^{87}Rb D_2 line data

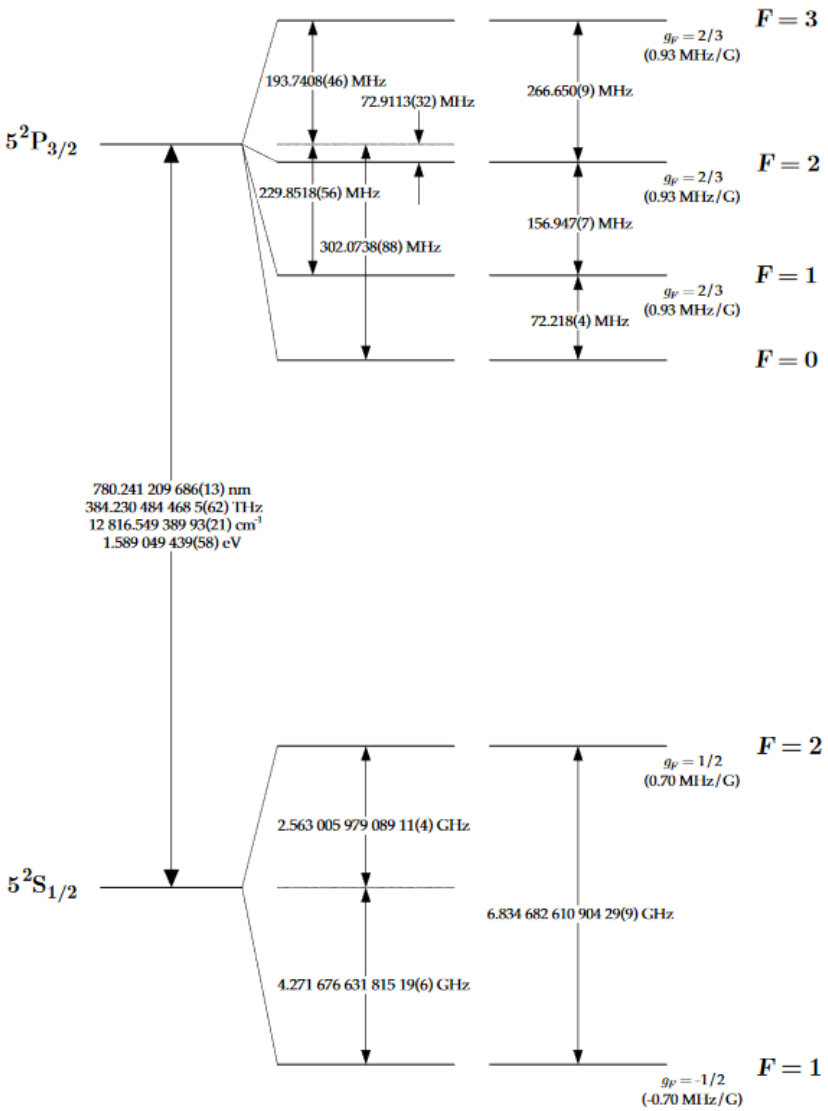

Figure A.1: ^{87}Rb D_2 line data [1]

A.2 Bragg diffraction

Bragg diffraction [50] is another possible interferometry type. Here, the atomic ensemble experiences light pulses, that transfer it to an intermediate state $|i\rangle$ and back, similar to Raman diffraction, but the transition is between the same internal energy states [92]. Assuming a Bragg transition $|F = 1, m_F = 0\rangle \rightarrow |i\rangle \rightarrow |F = 1, m_F = 0\rangle$, the wave functions in equation 3.2 and 3.3 change to:

$$|g\rangle = |F = 1, 0\rangle \tag{A.1}$$

$$|e\rangle = |F = 1, \hbar\vec{k}_{eff}\rangle \tag{A.2}$$

simplifying equation 3.8 for the detuning to:

$$\delta = \delta_{Dop} - \delta_r \tag{A.3}$$

An atomic ensemble with initial momentum $|0\rangle$ can be utilized for single and double diffraction with Bragg transitions as well [81, 89, 148]. Since the detuning between initial and final state is much smaller than for Raman transitions, Bragg diffraction can be realized through a combination of a laser and two AOMs with a frequency difference of the detuning δ [81]. The disadvantage of Bragg diffraction is that the atomic ensemble, after the interferometry sequence, only differ in their spacial position and not their internal states. Hence, the detection following the interferometry sequence is more challenging with an expanding atomic cloud compared to Raman diffraction.

A.3 VHDL code

A.3.1 Numeric Controlled Oscillator (NCO)

A.3.2 Phase Frequency Detector (PFD)

Listing A.1: Source code of the phase error calculation. The PFD measures the phase difference between the beat and the reference signal and gives out two signals, Up and Down. These signals are then processed by the TRC in Grey code and converted back to binary by a decoder for further processing. After decoding, 8 phase shifted, $1\,\mathrm{bit}$ Up and Down signals reflect the phase error.

```
1
2  library ieee;
3
4  use ieee.std_logic_1164.all;
5  use ieee.numeric_std.all;
6
7  entity PhaseErrorConverter is
8  port (
9  clk_A, clk_B, clk_C, clk_D            : in std_logic; -- 300+ MHz
10 clk_sys                     : in std_logic;  -- 100 MHz
11 REF                       : in std_logic; -- roughly 25 MHz
12 LAS                       : in std_logic; -- roughly 25 MHz
13 A_up_out, B_up_out, C_up_out, D_up_out      : out unsigned(3 downto 0);
14 A_down_out, B_down_out, C_down_out, D_down_out  : out unsigned(3 downto 0)
15 );
16 end entity;
17
18 architecture arch of PhaseErrorConverter is
19 constant TRC_len : integer := 4;
20 constant BIN_len : integer := 4;
21
22 component PhaseFrequencyDetector is
23 port(
24 RF : in std_logic;
25 LO : in std_logic;
26 Up   : out std_logic;
27 Down : out std_logic
28 );
29 end component;
30
31 component D_FF is
32 port(
33 clk : in std_logic;
34 D   : in std_logic;
35 Q   : out std_logic
36 );
37 end component;
38
39 component TwistedRingCounter is
40 generic(
41 N : integer range 1 to 20 := 4;
42 Saturation : string := "off"  -- "on" or "off"
43 );
44 port(
45 clk : in std_logic;
46 reset : in std_logic;
47 cnt : out std_logic_vector(N-1 downto 0); -- unregistered output
48 reg : out std_logic_vector(N-1 downto 0)  -- registerered output (falling edge)
49 );
50 end component;
51
52 component TRC2BIN is
53 generic(
54 TRC_len : integer := 4;
55 BIN_len : integer := 4
56 );
57 port(
```

```
58 TRC : in std_logic_vector(TRC_len-1 downto 0);
59 BIN : out unsigned(BIN_len-1 downto 0)
60 );
61 end component;
62
63 signal up, up_A, up_B, up_C, up_D           : std_logic:='0';
64 signal down, down_A, down_B, down_C, down_D     : std_logic:='0';
65 signal TRC_A_up, TRC_B_up       : std_logic_vector(TRC_len-1 downto 0);
66 signal TRC_C_up, TRC_D_up     : std_logic_vector(TRC_len-1 downto 0);
67 signal TRC_A_down, TRC_B_down   : std_logic_vector(TRC_len-1 downto 0);
68 signal TRC_C_down, TRC_D_down   : std_logic_vector(TRC_len-1 downto 0);
69 signal BIN_A_up, BIN_B_up     : unsigned(BIN_len-1 downto 0);
70 signal BIN_C_up, BIN_D_up     : unsigned(BIN_len-1 downto 0);
71 signal BIN_A_down, BIN_B_down   : unsigned(BIN_len-1 downto 0);
72 signal BIN_C_down, BIN_D_down   : unsigned(BIN_len-1 downto 0);
73
74 begin
75 PFD:    PhaseFrequencyDetector port map (LAS, REF, up, down);
76 Sync_up_A:  D_FF port map(clk_A,up,up_A);
77 Sync_up_B:  D_FF port map(clk_B,up,up_B);
78 Sync_up_C:  D_FF port map(clk_C,up,up_C);
79 Sync_up_D:  D_FF port map(clk_D,up,up_D);
80 Sync_down_A:D_FF port map(clk_A,down,down_A);
81 Sync_down_B:D_FF port map(clk_B,down,down_B);
82 Sync_down_C:D_FF port map(clk_C,down,down_C);
83 Sync_down_D:D_FF port map(clk_D,down,down_D);
84 TRC_A_u:  TwistedRingCounter port map(clk_A,up_A,TRC_A_up,open);
85 TRC_B_u:  TwistedRingCounter port map(clk_B,up_B,TRC_B_up,open);
86 TRC_C_u:  TwistedRingCounter port map(clk_C,up_C,TRC_C_up,open);
87 TRC_D_u:  TwistedRingCounter port map(clk_D,up_D,TRC_D_up,open);
88 TRC_A_d:  TwistedRingCounter port map(clk_A,down_A,TRC_A_down,open);
89 TRC_B_d:  TwistedRingCounter port map(clk_B,down_B,TRC_B_down,open);
90 TRC_C_d:  TwistedRingCounter port map(clk_C,down_C,TRC_C_down,open);
91 TRC_D_d:  TwistedRingCounter port map(clk_D,down_D,TRC_D_down,open);
92 BIN_A_u:  TRC2BIN  port map(TRC_A_up,BIN_A_up);
93 BIN_B_u:  TRC2BIN  port map(TRC_B_up,BIN_B_up);
94 BIN_C_u:    TRC2BIN  port map(TRC_C_up,BIN_C_up);
95 BIN_D_u:    TRC2BIN  port map(TRC_D_up,BIN_D_up);
96 BIN_A_d:    TRC2BIN  port map(TRC_A_down,BIN_A_down);
97 BIN_B_d:    TRC2BIN  port map(TRC_B_down,BIN_B_down);
98 BIN_C_d:    TRC2BIN  port map(TRC_C_down,BIN_C_down);
99 BIN_D_d:    TRC2BIN  port map(TRC_D_down,BIN_D_down);
100
101 A_up_out <= BIN_A_up;
102 B_up_out <= BIN_B_up;
103 C_up_out <= BIN_C_up;
104 D_up_out <= BIN_D_up;
105 A_down_out <= BIN_A_down;
106 B_down_out <= BIN_B_down;
107 C_down_out <= BIN_C_down;
108 D_down_out <= BIN_D_down;
109
110 end architecture;
111
112
```

Listing A.2: Source code of the PFD. The phase and frequency difference between the beat (RF) and reference signal (LO) is measured by this part of the code. The PFD outputs an Up and a Down signal.

```
1
2 library ieee;
3
4 use ieee.std_logic_1164.all;
5 use ieee.numeric_std.all;
6
7 entity PhaseFrequencyDetector is
8 port(
9 RF : in std_logic;
```

```
10 LO : in std_logic;
11 Up   : out std_logic;
12 Down : out std_logic
13 );
14 end entity;
15
16 architecture arch of PhaseFrequencyDetector is
17 signal U,D : std_logic;
18 begin
19 Up<=U;
20 Down<=D;
21 process (RF,LO,U,D)
22 begin
23 if U='1' and D='1' then
24 D<='0';
25 U<='0';
26 else
27 if rising_edge(RF) then
28 D<='1';
29 end if;
30 if rising_edge(LO) then
31 U<='1';
32 end if;
33 end if;
34 end process;
35
36 end architecture;
37
38
```

Listing A.3: Source code of the $1\,\mathrm{bit}$ D flip-flop.

```
1
2 library ieee;
3
4 use ieee.std_logic_1164.all;
5 use ieee.numeric_std.all;
6
7 entity D_FF is
8 port(
9 clk : in std_logic;
10 D   : in std_logic:='0';
11 Q   : out std_logic
12 );
13 end entity;
14
15 architecture arch of D_FF is
16
17
18 begin
19 process(clk)
20
21
22 begin
23
24 if rising_edge(clk) then
25 Q<=D;
26
27 end if;
28 end process;
29 end architecture;
```

A.3.3 Twisted Ring Counter (TRC)

Listing A.4: Source code of the Twisted Ring Counter (TRC). This part of the phaselock code converts the Up and Down signal from binary code to Grey code.

```
1
2  library ieee;
3
4  use ieee.std_logic_1164.all;
5  use ieee.numeric_std.all;
6
7  entity TwistedRingCounter is
8  generic(
9  N : integer range 1 to 20 := 4;
10 Saturation : string := "off"  -- "on" or "off"
11 );
12 port(
13 clk : in std_logic;
14 reset : in std_logic;
15 cnt : out std_logic_vector(N-1 downto 0); -- unregistered output
16 reg : out std_logic_vector(N-1 downto 0)  -- registerered output (falling edge)
17 );
18 end entity;
19
20 architecture arch of TwistedRingCounter is
21 signal Q :  std_logic_vector(N-1 downto 0):=(others=>'0');
22 begin
23 cnt<=Q;
24 process (clk, reset)
25 begin
26 if reset='0' then
27 Q<=(others=>'0');
28 else
29 if rising_edge(clk) then
30 Q(N-1)<=not Q(0);
31 if Saturation="on" then
32 if Q(0)='1' and Q(1)='0' then
33 for I in 0 to N-2 loop
34 Q(I)<=Q(I); -- saturated
35 end loop;
36 else
37 for I in 0 to N-2 loop
38 Q(I)<=Q(I+1); -- normal counting
39 end loop;
40 end if;
41 else
42 -- no saturation
43 for I in 0 to N-2 loop
44 Q(I)<=Q(I+1);
45 end loop;
46 end if;
47 end if;
48 end if;
49 end process;
50
51 process (reset)
52 begin
53 if falling_edge(reset) then
54 reg<=Q;
55 end if;
56 end process;
57
58
59 end architecture;
60
61
```

A.3.4 Decoder

Listing A.5: Source code of the decoder. This decoder has the purpose of decoding the Up and Down signal from Grey code to binary code.

```
1
```

```
2  library ieee;
3
4  use ieee.std_logic_1164.all;
5  use ieee.numeric_std.all;
6
7  entity TRC2BIN is
8  generic(
9  TRC_len : integer := 4;
10 BIN_len : integer := 4
11 );
12 port(
13 TRC : in std_logic_vector(TRC_len-1 downto 0);
14 BIN : out unsigned(BIN_len-1 downto 0)
15 );
16 end entity;
17
18
19
20 architecture arch of TRC2BIN is
21 function CountLeft(X : std_logic_vector; C : std_logic) return integer is
22 variable i : integer;
23 begin
24 i:=X'left;
25 while ((i>=0) and (X(i)=C)) loop
26 i:=i-1;
27 end loop;
28 return (X'left-i);
29 end function;
30 begin
31 assert (2**BIN_len>=2*TRC_len) report "TRC2BIN: length of output does not fit to input.";
32 process (TRC)
33 begin
34 -- number of valid TRC states: 2 * TRC_len
35 -- number of BIN states: 2^BIN_len
36 if TRC=(TRC'range=>'0') then
37 BIN<=to_unsigned(0,BIN'length);
38 else
39 if TRC(TRC'left)='1' then
40 BIN <= to_unsigned(CountLeft(TRC,'1'),BIN'length);
41 -- count number of ones on the left side of TRC
42 else
43 BIN<= TRC_LEN + to_unsigned(CountLeft(TRC,'0'),BIN'length);
44 -- count number of zeros on the left side of TRC
45 end if;
46 end if;
47 end process;
48 end architecture;
49
50
```

A.3.5 Synchronizer

Listing A.6: Source code of the Synchronizer consisting of several subcomponents. The code synchronizes the phase shifted Up and Down signals from the 4 $300\,\mathrm{MHz}$ clocks to the $100\,\mathrm{MHz}$ clock and calculates the error signal via subtraction.

```
1
2  library ieee;
3
4  use ieee.std_logic_1164.all;
5  use ieee.numeric_std.all;
6
7  entity Sync_total is
8  port(
9  clk_A, clk_B, clk_C, clk_D            : in std_logic;
10 clk_sys                               : in std_logic;
11 A_up_in, B_up_in, C_up_in, D_up_in        : in unsigned(3 downto 0);
```

```
12 A_down_in, B_down_in, C_down_in, D_down_in    : in unsigned(3 downto 0);
13 error                              : out signed(7 downto 0)
14 );
15 end entity;
16
17 architecture arch of Sync_total is
18
19 component TRC_adder is
20 port(
21 clk_300     : in std_logic;
22 TRCBIN_in   : in unsigned(3 downto 0);
23 TRCBIN_sum    : out unsigned(7 downto 0)
24 );
25 end component;
26
27 component D_FF_long is
28
29 generic(
30 D_FF_length : integer range 1 to 8:=8
31 );
32 port(
33 clk : in std_logic;
34 D   : in unsigned(D_FF_length-1 downto 0);
35 Q   : out unsigned(D_FF_length-1 downto 0)
36 );
37 end component;
38
39 component Sync is
40 port(
41 clk_in        : in std_logic;
42 clk_drive     : in std_logic;
43 sync_out      : out std_logic
44 );
45 end component;
46
47 component DE_FF_long is
48 generic(
49 D_FF_length : integer range 1 to 8:=8
50 );
51 port(
52 clk : in std_logic;
53 D   : in unsigned(D_FF_length-1 downto 0);
54 e   : in std_logic;
55 Q   : out unsigned(D_FF_length-1 downto 0)
56 );
57 end component;
58
59
60 signal  out_A_up, out_B_up, out_C_up, out_D_up      : unsigned(7 downto 0);
61 signal  out_A_down, out_B_down, out_C_down, out_D_down  : unsigned(7 downto 0);
62 signal  out_A_up2, out_B_up2, out_C_up2, out_D_up2    : unsigned(7 downto 0);
63 signal  out_A_down2, out_B_down2, out_C_down2, out_D_down2  : unsigned(7 downto 0);
64 signal  sync_A_up, sync_B_up, sync_C_up, sync_D_up    : unsigned(7 downto 0);
65 signal  sync_A_down, sync_B_down, sync_C_down, sync_D_down  : unsigned(7 downto 0);
66 signal  drive_A_up, drive_B_up, drive_C_up, drive_D_up  : unsigned(7 downto 0);
67 signal  drive_A_down, drive_B_down, drive_C_down, drive_D_down : unsigned(7 downto 0);
68 signal  sum_up, sum_down                : unsigned(7 downto 0);
69 signal  enable_A, enable_B, enable_C, enable_D      : std_logic:='0';
70 signal  output                      : signed(7 downto 0);
71
72 begin
73
74 -- Addding of 4 Bit counter inputs for 3x 300 MHz clock cycles
75 Adder_A_up : TRC_adder port map(clk_A, A_up_in, out_A_up);
76 Adder_B_up : TRC_adder port map(clk_B, B_up_in, out_B_up);
77 Adder_C_up : TRC_adder port map(clk_C, C_up_in, out_C_up);
78 Adder_D_up : TRC_adder port map(clk_D, D_up_in, out_D_up);
79 Adder_A_down : TRC_adder port map(clk_A, A_down_in, out_A_down);
80 Adder_B_down : TRC_adder port map(clk_B, B_down_in, out_B_down);
81 Adder_C_down : TRC_adder port map(clk_C, C_down_in, out_C_down);
```

```
82  Adder_D_down : TRC_adder port map(clk_D, D_down_in, out_D_down);
83  -- Synchronizing added inputs to 300 MHz shifted clocks (Safety measure)
84  Flop_A_up: D_FF_long port map(clk_A, out_A_up, out_A_up2);
85  Flop_B_up: D_FF_long port map(clk_B, out_B_up, out_B_up2);
86  Flop_C_up: D_FF_long port map(clk_C, out_C_up, out_C_up2);
87  Flop_D_up: D_FF_long port map(clk_D, out_D_up, out_D_up2);
88  Flop_A_down: D_FF_long port map(clk_A, out_A_down, out_A_down2);
89  Flop_B_down: D_FF_long port map(clk_B, out_B_down, out_B_down2);
90  Flop_C_down: D_FF_long port map(clk_C, out_C_down, out_C_down2);
91  Flop_D_down: D_FF_long port map(clk_D, out_D_down, out_D_down2);
92  -- Synchronizing the 4x300 MHz clocks with phase shifts to the 1x100 MHz clock
93  -- to generate synchronized enable signals
94  Sync_A: Sync port map(clk_A, clk_sys, enable_A);
95  Sync_B: Sync port map(clk_B, clk_sys, enable_B);
96  Sync_C: Sync port map(clk_C, clk_sys, enable_C);
97  Sync_D: Sync port map(clk_D, clk_sys, enable_D);
98  -- Synchronizing the inputs to the enable signals at 300 MHz
99  -- (gives out signal every 3 clock cycles), which is readable
100 -- for the 100 MHz clk flip flop
101 Flop2_A_up: DE_FF_long port map(clk_A, out_A_up2, enable_A, drive_A_up);
102 Flop2_B_up: DE_FF_long port map(clk_B, out_B_up2, enable_B, drive_B_up);
103 Flop2_C_up: DE_FF_long port map(clk_C, out_C_up2, enable_C, drive_C_up);
104 Flop2_D_up: DE_FF_long port map(clk_D, out_D_up2, enable_D, drive_D_up);
105 Flop2_A_down: DE_FF_long port map(clk_A, out_A_down2, enable_A, drive_A_down);
106 Flop2_B_down: DE_FF_long port map(clk_B, out_B_down2, enable_B, drive_B_down);
107 Flop2_C_down: DE_FF_long port map(clk_C, out_C_down2, enable_C, drive_C_down);
108 Flop2_D_down: DE_FF_long port map(clk_D, out_D_down2, enable_D, drive_D_down);
109 -- Synchronizing the inputs to the 100 MHz clock
110 Flop3_A_up: D_FF_long port map(clk_sys, drive_A_up, sync_A_up);
111 Flop3_B_up: D_FF_long port map(clk_sys, drive_B_up, sync_B_up);
112 Flop3_C_up: D_FF_long port map(clk_sys, drive_C_up, sync_C_up);
113 Flop3_D_up: D_FF_long port map(clk_sys, drive_D_up, sync_D_up);
114 Flop3_A_down: D_FF_long port map(clk_sys, drive_A_down, sync_A_down);
115 Flop3_B_down: D_FF_long port map(clk_sys, drive_B_down, sync_B_down);
116 Flop3_C_down: D_FF_long port map(clk_sys, drive_C_down, sync_C_down);
117 Flop3_D_down: D_FF_long port map(clk_sys, drive_D_down, sync_D_down);
118
119 process(clk_sys)
120 begin
121 if rising_edge(clk_sys) then
122 sum_up <= resize(sync_A_up,error'length)+resize(sync_B_up,error'length)
123 +resize(sync_C_up,error'length)+resize(sync_D_up,error'length);
124 sum_down <= resize(sync_A_down,error'length)+resize(sync_B_down,error'length)
125 +resize(sync_C_down,error'length)+resize(sync_D_down,error'length);
126 end if;
127
128 if rising_edge(clk_sys) then
129 error<=signed(sum_up) - signed(sum_down);
130 end if;
131
132 end process;
133 end architecture;
```

Listing A.7: Source code of one synchronizer subfunction.

```
1
2  library ieee;
3
4  use ieee.std_logic_1164.all;
5  use ieee.numeric_std.all;
6
7  entity Sync is
8  port(
9  clk_in      : in std_logic;
10 clk_drive   : in std_logic;
11 sync_out    : out std_logic
12 );
13 end entity;
14
15 architecture arch of Sync is
```

```
16
17 component D_FF is
18 port(
19 clk : in std_logic;
20 D   : in std_logic;
21 Q   : out std_logic
22 );
23 end component;
24
25 signal  out1, out2, out3, out4, out5  : std_logic:='0';
26 signal  andout              : std_logic:='0';
27
28 begin
29 A1  : D_FF  port map(clk_in,clk_drive,out1);
30 A2  : D_FF  port map(clk_in,out1,out2);
31 A3  : D_FF  port map(clk_in,out2,out3);
32 A4  : D_FF  port map(clk_in,out3,out4);
33
34 andout <= out3 and not out4;
35
36 Aout: D_FF  port map(clk_in,andout,sync_out);
37
38 end architecture;
```

Listing A.8: Source code of one synchronizer subfunction.

```
1
2 library ieee;
3
4 use ieee.std_logic_1164.all;
5 use ieee.numeric_std.all;
6
7 entity TRC_adder is
8 port(
9 clk_300     : in std_logic;
10 TRCBIN_in   : in unsigned(3 downto 0);
11 TRCBIN_sum    : out unsigned(7 downto 0)
12 );
13 end entity;
14
15 architecture arch of TRC_adder is
16
17 component D_FF_long is
18
19 generic(
20 D_FF_length : integer range 1 to 8:=8
21 );
22
23 port(
24 clk : in std_logic;
25 D   : in unsigned(D_FF_length-1 downto 0);
26 Q   : out unsigned(D_FF_length-1 downto 0)
27 );
28 end component;
29
30 signal out1, out2, out3, out4   : unsigned(7 downto 0):= (others => '0');
31 signal TRCBIN_sum1, TRCBIN_sum2 : unsigned(7 downto 0):= (others => '0');
32 signal TRCBIN             : unsigned(7 downto 0):= (others => '0');
33
34 begin
35 TRCBIN <= resize(TRCBIN_in,8);
36 sync1:  D_FF_long port map(clk_300, TRCBIN, out1);
37 sync2:  D_FF_long port map(clk_300, out1, out2);
38 sync3:  D_FF_long port map(clk_300, out2, out3);
39 sync4:  D_FF_long port map(clk_300, out3, out4);
40 sync5:  D_FF_long port map(clk_300, TRCBIN_sum1, TRCBIN_sum2);
41
42 process(clk_300)
43 begin
44 if rising_edge(clk_300) then
```

```
TRCBIN_sum1 <= out1 + out2;
end if;

if rising_edge(clk_300) then
TRCBIN_sum <= TRCBIN_sum2 + out4;
TRCBIN_sum <= out1;
end if;
end process;

end architecture;
```

Listing A.9: Source code of the DE flip-flop with an adjustable bit length.

```

library ieee;

use ieee.std_logic_1164.all;
use ieee.numeric_std.all;

entity DE_FF_long is
generic(
D_FF_length : integer range 1 to 8:=4
);
port(
clk : in std_logic;
D   : in unsigned(D_FF_length-1 downto 0):= (others => '0');
e   : in std_logic;
Q   : out unsigned(D_FF_length-1 downto 0)
);
end entity;

architecture arch of DE_FF_long is


begin
process(clk,e)


begin

if rising_edge(clk) then
if e='1' then
Q<=D;
end if;
end if;
end process;
end architecture;

```

Listing A.10: Source code of the D flip-flop with an adjustable bit length.

```

library ieee;

use ieee.std_logic_1164.all;
use ieee.numeric_std.all;

entity D_FF_long is
generic(
D_FF_length : integer range 1 to 8:=4
);
port(
clk : in std_logic;
D   : in unsigned(D_FF_length-1 downto 0):= (others => '0');
Q   : out unsigned(D_FF_length-1 downto 0)
```

```
15 );
16 end entity;
17
18 architecture arch of D_FF_long is
19
20
21 begin
22 process(clk)
23
24
25 begin
26
27 if rising_edge(clk) then
28 Q<=D;
29
30 end if;
31 end process;
32 end architecture;
```

A.3.6 PID

Listing A.11: Source code of the proportional integral derivative (PID) loop filter. The purpose of the PID is to generate a control signal to stear the laser current. The filter recieves the synchronized phase error from the synchronizer and generates a control signal for the current driver board via an integral, a parallel and a derivative response. This code has $16\,\mathrm{bit}$ inputs for the PID amplification gains so that they can be adjusted by the user.

```
1  library ieee;
2
3  use ieee.std_logic_1164.all;
4  use ieee.numeric_std.all;
5
6  entity PIID is
7  port(
8  clk     : in std_logic;
9  Ist     : in signed(7 downto 0):= (others => '0');
10 P_const   : in signed(15 downto 0);
11 I_const   : in signed(15 downto 0);
12 D_const   : in signed(15 downto 0);
13 FastOut : out signed(14 downto 0);
14 Setpoint  : out signed(15 downto 0)
15 );
16 end entity;
17
18 architecture arch of PIID is
19
20 signal error : signed(15 downto 0):=to_signed(0,16);
21
22 begin
23 process(clk)
24 variable preerror       : signed(14 downto 0):=to_signed(0,15);
25 variable P        : signed(15 downto 0):= (others => '0');
26 variable D        : signed(15 downto 0):= (others => '0');
27 variable I        : signed(31 downto 0):= (others => '0');
28 variable I_shift      : signed(17 downto 0):= (others => '0');
29 variable I_resize     : signed(16 downto 0):= (others => '0');
30 variable P_product      : signed(31 downto 0):= (others => '0');
31 variable I_product      : signed(31 downto 0):= (others => '0');
32 variable D_product      : signed(31 downto 0):= (others => '0');
33 variable sngSetpoint      : signed(14 downto 0):= (others => '0');
34 variable sum        : signed(14 downto 0):= (others => '0');
35
36 subtype GIGASIGNED is signed(31 downto 0);
37 function saturate(
38 input   : signed(31 downto 0):= (others => '0');
39 min     : signed(31 downto 0);
```

```
40 max     : signed(31 downto 0))
41 return GIGASIGNED is
42 begin
43 if input<min then return to_signed(to_integer(min), 32);
44 elsif input>max then return to_signed(to_integer(max), 32);
45 else return input;
46 end if;
47 end function;
48
49 subtype sng15 is signed(14 downto 0);
50 function saturate15(
51 input   : signed(31 downto 0):= (others => '0');
52 min     : signed(14 downto 0);
53 max     : signed(14 downto 0))
54 return sng15 is
55 begin
56 if resize(input,15)<min then return to_signed(to_integer(min), 15);
57 elsif resize(input,15)>max then return to_signed(to_integer(max), 15);
58 else return resize(input,15);
59 end if;
60 end function;
61
62
63 begin
64 if rising_edge(clk) then
65 sum:=saturate15(P_product+I_product+D_product,to_signed(-8191,15),to_signed(8191,15));
66 end if;
67
68 if rising_edge(clk) then
69
70 P_product := (P*P_const);
71 I_product := (I_shift*I_const(13 downto 0));
72 D_product := (D*D_const);
73
74 end if;
75
76 if rising_edge(clk) then
77
78 P       :=resize(-Ist,16);
79 D       :=resize(resize(-Ist,16)-error,16);
80 I       :=saturate(I-resize(-Ist,32),to_signed(-67108864,32),to_signed(67108863,32));
81 I_shift   :=I(24 downto 7);
82 end if;
83
84 if rising_edge(clk) then
85 error <= resize(-Ist,16);
86 FastOut<= sum;
87 Setpoint <=shift_left(resize(-Ist,16),2);
88 end if;
89
90 end process;
91 end architecture;
92
93
```

A.4 Control theory calculations

In this chapter, the intermediate steps for the calculation of the transfer function in the Laplace domain as well as the damping coefficient and the natural radian frequency are displayed.

A.4.1 Laplace transfer function

$$H(s) = \frac{G(s)}{1+G(s)} = \frac{K_d {}^{K_o}/_{s} F(s)}{s + K_d {}^{K_o}/_{s} F(s)} \tag{A.4}$$

$$\leftrightarrow H(s) = \frac{K_d K_o F(s)}{s + K_d K_o F(s)} \tag{A.5}$$

$$\leftrightarrow H(s) = \frac{K_d K_o (K_P + {}^{K_I}/_{s} + K_D \cdot s)}{s + K_d K_o (K_P + {}^{K_I}/_{s} + K_D \cdot s)} \tag{A.6}$$

$$\leftrightarrow H(s) = \frac{K_d K_o (K_P + {}^{K_I}/_{s} + K_D \cdot s)}{s + K_d K_o (K_P + {}^{K_I}/_{s} + K_D \cdot s)} \cdot \frac{s}{s} \tag{A.7}$$

$$\leftrightarrow H(s) = \frac{s^2 \cdot (K_d K_o K_D) + s \cdot (K_d K_o K_P) + (K_d K_o K_I)}{s^2 \cdot (1 + K_d K_o K_D) + s \cdot (K_d K_o K_P) + (K_d K_o K_I)} \tag{A.8}$$

$$\leftrightarrow H(s) = \frac{s^2 \cdot {}^{K_d K_o K_D}/_{1+K_d K_o K_D} + s \cdot {}^{K_d K_o K_P}/_{1+K_d K_o K_D} + {}^{K_d K_o K_I}/_{1+K_d K_o K_D}}{s^2 + s \cdot {}^{K_d K_o K_P}/_{1+K_d K_o K_D} + {}^{K_d K_o K_I}/_{1+K_d K_o K_D}} \tag{A.9}$$

A.4.2 Damping coefficient and natural radian frequency

$$s^2 + 2\zeta\omega_n + \omega_n^2 = 1 + G(s) = 0 \tag{A.10}$$

$$\leftrightarrow s^2 + 2\zeta\omega_n + \omega_n^2 \stackrel{!}{=} s^2 + s \cdot {}^{K_d K_o K_P}/_{1+K_d K_o K_D} + {}^{K_d K_o K_I}/_{1+K_d K_o K_D} \tag{A.11}$$

$$\rightarrow \omega_n = \sqrt{\frac{K_d K_o K_I}{1 + K_d K_o K_D}} \tag{A.12}$$

$$\rightarrow 2\zeta\omega_n = 2\zeta\sqrt{\frac{K_d K_o K_I}{1 + K_d K_o K_D}} \stackrel{!}{=} \frac{K_d K_o K_P}{1 + K_d K_o K_D} \tag{A.13}$$

$$\leftrightarrow \zeta = \frac{{}^{K_d K_o K_P}/_{2(1+K_d K_o K_D)}}{\sqrt{{}^{K_d K_o K_I}/_{1+K_d K_o K_D}}} \tag{A.14}$$

$$\leftrightarrow \zeta = \frac{(K_d K_o K_P)\sqrt{1 + K_d K_o K_D}}{2(1 + K_d K_o K_D)\sqrt{K_d K_o K_I}} \tag{A.15}$$

$$\zeta = \frac{K_P}{2}\sqrt{\frac{K_d K_o}{(1 + K_d K_o K_D) K_I}} = \frac{K_P}{2K_I}\omega_n \tag{A.16}$$

A.5 The TBus standard

The TBus standard serves as an internal design guideline for PCBs specially crafted to meet the requirements of laser-based experiments conducted in microgravity environments. Its primary focus is on optimizing performance for compact, self-contained systems such as drop tower capsules and sounding rockets. It was originally developed by Dr. Thijs Wendrich for the application in the QUANTUS drop tower missions. Within the LASUS project, founded by the DLR, several PCBs with integrated microelectronics for the use in atom optic experiments have been created. In the context of this thesis, PCBs conforming to the TBus standard are commonly referred to as "cards" or "boards." These cards can be physically stacked together and establish connections through two board-to-board connectors—one for analog signals and the other for digital signals. While these connectors share similarities with the PC104 standard, they differ in terms of pin arrangement and placement, making them mechanically incompatible. Access to a stack of TBus cards is facilitated through an interface card.

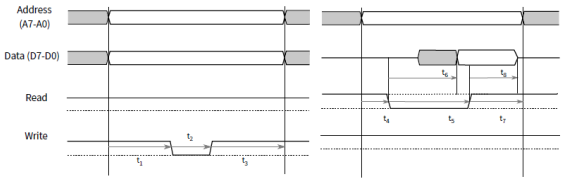

Figure A.2: Illustration of a standard TBus read and write cycle with the times $t_{1,2,3}$ for the write operation and $t_{4,5,6,7,8}$ for the read operation. A more detailed description can be found here [38].

The TBus offers several connectivity options, including USB, NI-FPGA, Ethernet, and POF. Moreover, a connection between the TBus and the PC104 bus can be established using an adapter board. The laser frequency control board which was developed during this thesis is part of the TBus standard as well as the electronic boards that were utilized in order to obtain the measurements with the DPLL in chapter 6.

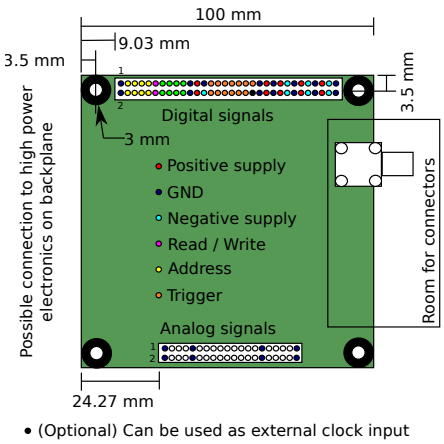

Figure A.3: Illustration of a standard TBus board layout. The exact pin configuration can be found here [30].

The TBus is an 8-bit bus system (8 data lines, 8 address lines, 2 command lines, 13 trigger lines and one clock line). A typical read and write cycle of the TBus is illustrated in figure A.2. The communication between the stacks uses a 3-byte protocol. It can be clocked externally at $10\,\mathrm{MHz}$ or $24\,\mathrm{MHz}$. Each card within a stack obtains a specific address via a rotary encoder. The configuration of 8 address lines theoretically permits up to 255 unique addresses for each stack. To enable the addressing of multiple registers on more complicated boards, the address byte's uppermost 4 bits are employed to designate a card, while the lower 4 bits are used to pinpoint registers on the given card. This setup theoretically permits addressing 16 cards, each equipped with 16 registers, for every stack. The communication is enabled via the TBus Dynamic Link Library (DLL). In order to

specify the address space of a TBus environment, two additional files are required. A stack.xml file for every stack specifies the address as well as the interface and card type in a stack. A card.xml for every card in a stack describes the register addresses of this card.
The mechanical design of TBus cards is a $100\,\mathrm{mm} \times 100\,\mathrm{mm}$ PCB with the PC104 connectors on the sides. The mechanical design is illustrated in figure A.3. The height of the PC104 connectors of $16\,\mathrm{mm}$ and the PCB thickness of $1.6\,\mathrm{mm}$ lead to a height of $17.6\,\mathrm{mm}$ for a card in a stack.
The TBus was originally designed to have seven different supply voltages. However, seven voltages were not practical for the application in the MAIUS-B apparatus, since every supply voltage corresponds to a heavy battery pack. Therefore, the amount of supply voltages was reduced to three. The system which was used to obtain the data for Raman double diffraction with the DPLL used boards in the original TBus standard, whilst the characterization measurements of the phaselock were carried out with boards in the newer TBus standard. However, the relevant electronic paths of the boards for the measurements with the DPLL stayed the same, which enabled a valid comparison of the phaselock's performance. A more detailed description of the TBus standard is provided here [38].

A.6 Schematics and block diagram

A.6.1 Laser frequency control board

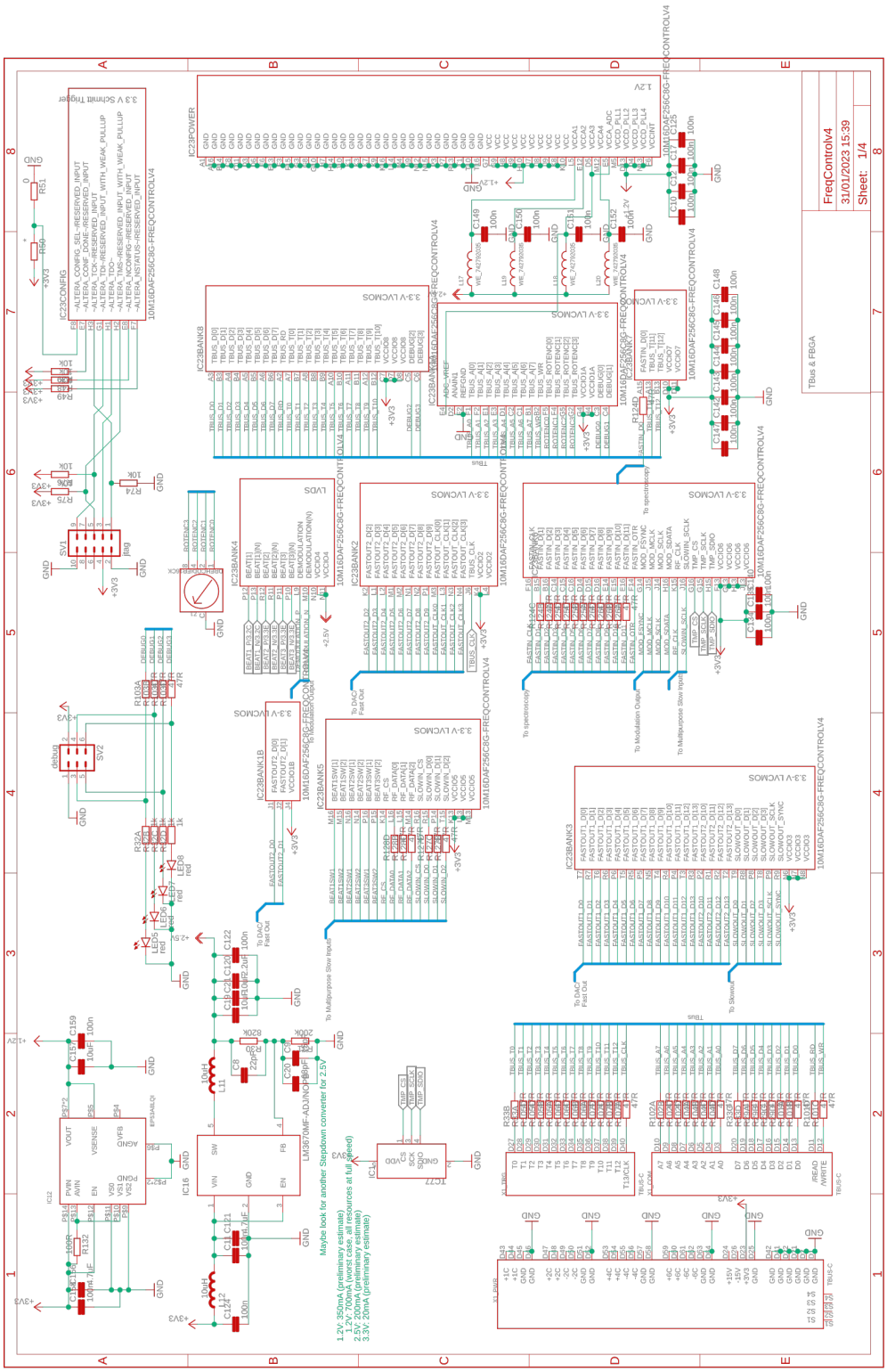

Figure A.4: Schematic of the laser frequency control board. This sheet shows the connections of the board between the digital TBus and the FPGA as well as the power supply connection.

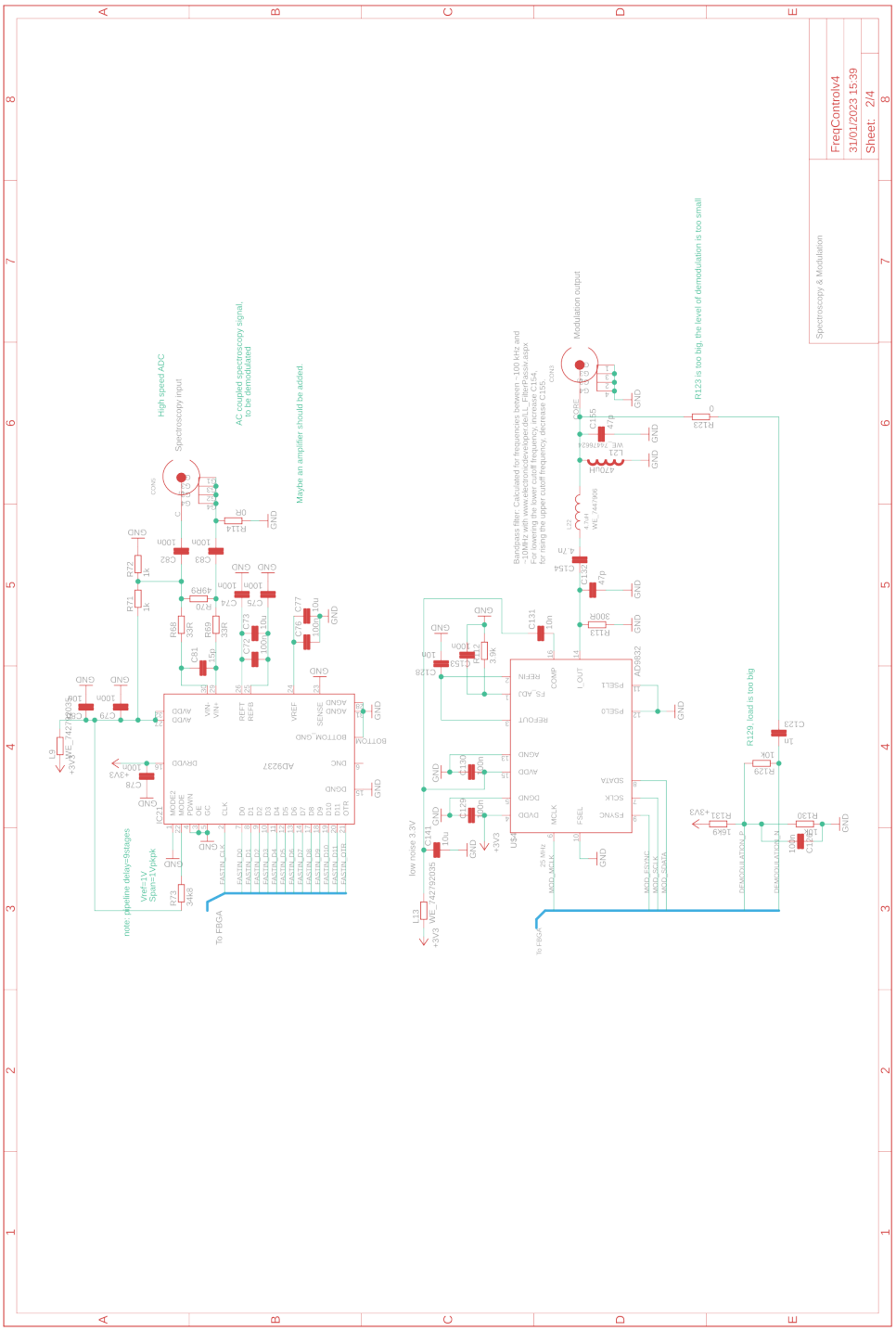

Figure A.5: Schematic of the DDS modulation output and Spectroscopy input of the laser frequency control board. This sheet shows the in- and output used to stabilize a laser to an atomic transition through frequency modulation spectroscopy e.g. via a gas cell.

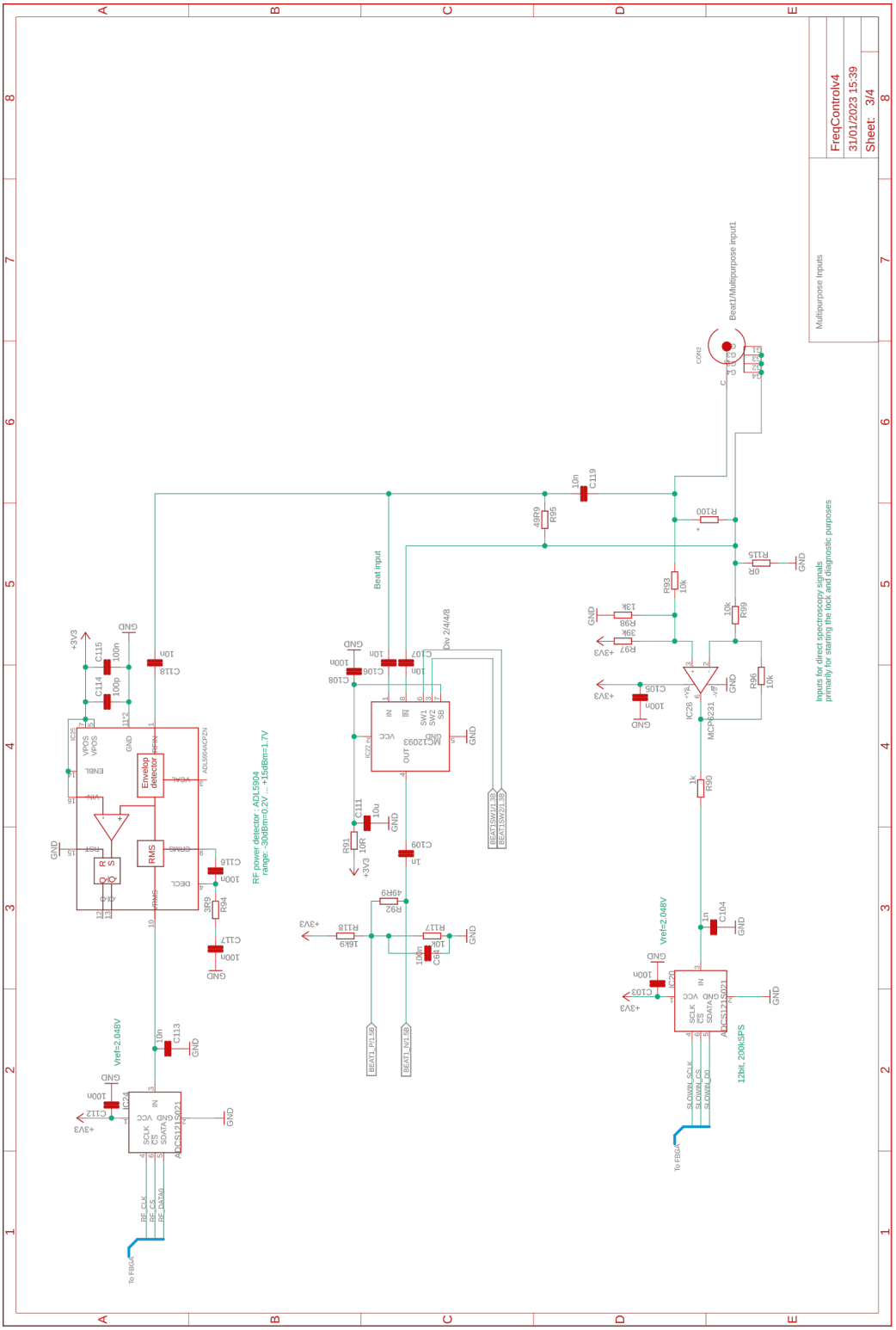

Figure A.6: Schematic of one multipurpose input of the laser frequency control board. This sheet shows the input which enables the readout of high frequency beat signals up to $2\,\mathrm{GHz}$, RF power and low frequency spectroscopy signals.

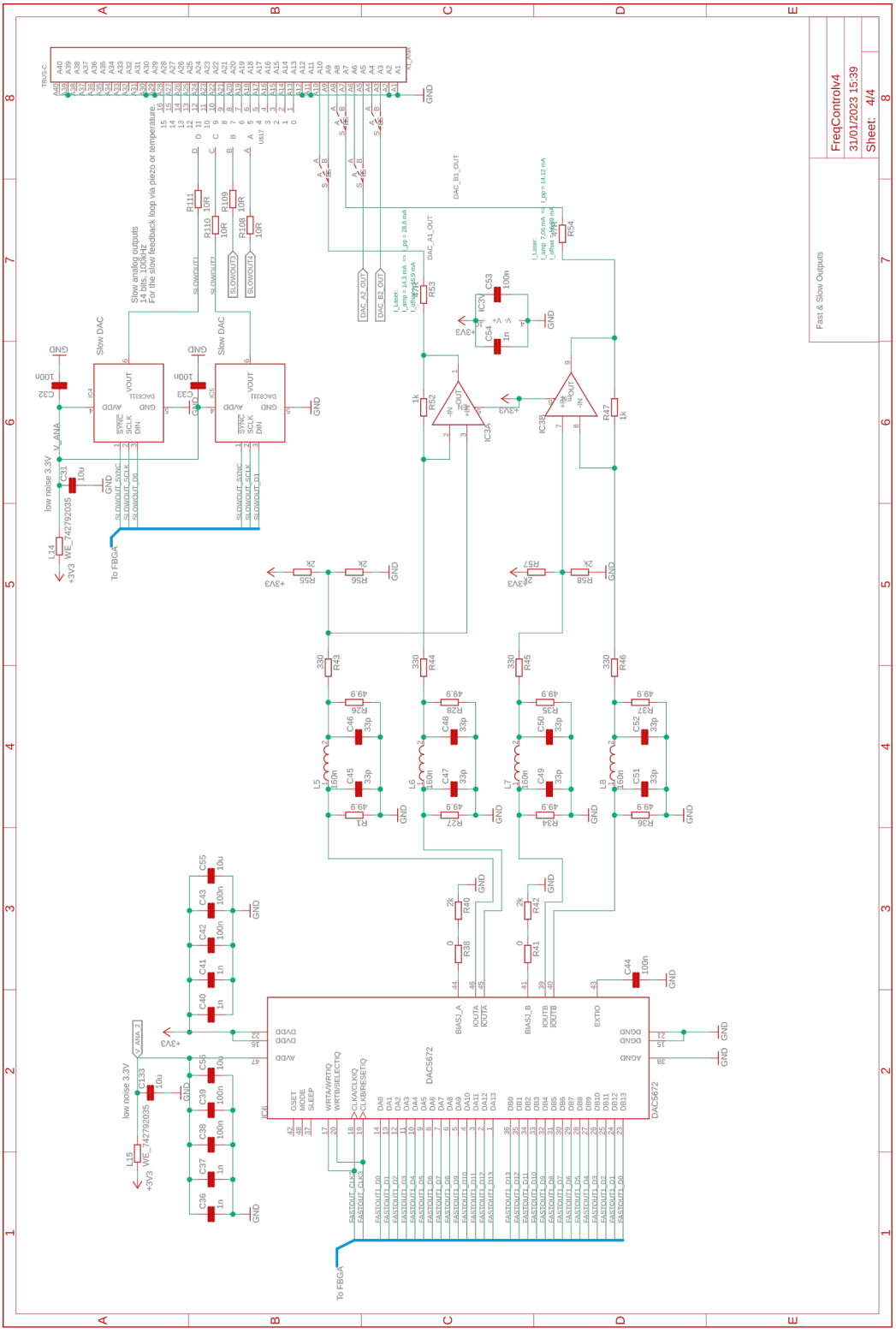

Figure A.7: Schematic of the fast and slow outputs of the laser frequency control board to the analog TBus. The fast output illustrated on this sheet is used for transmitting a control signal to the current drivers, while the slow output transmits a control signal to the temperature controller or piezo controller.

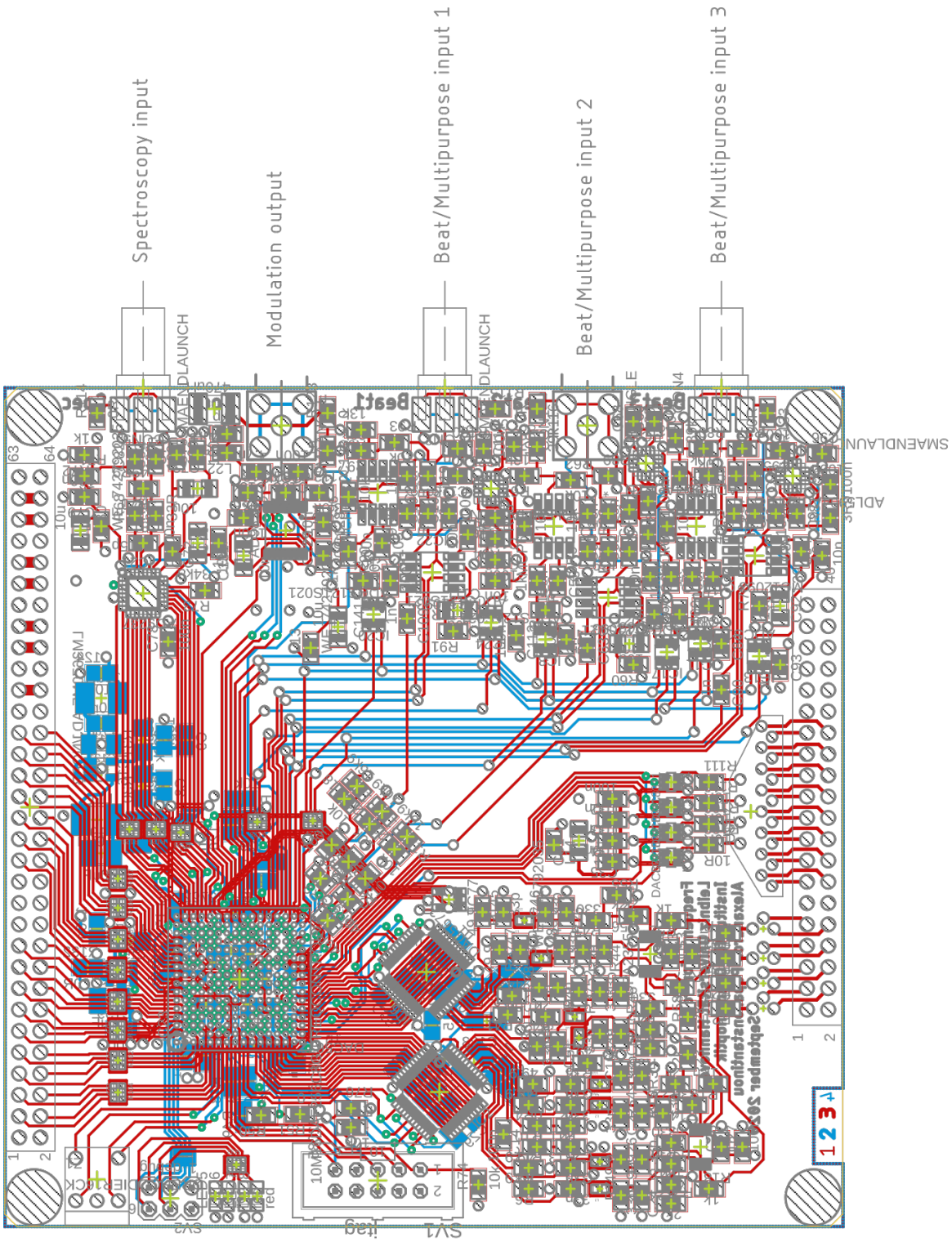

Figure A.8: Illustration of the PCB layout of the laser frequency control board.

A.6.2 Laser current driver

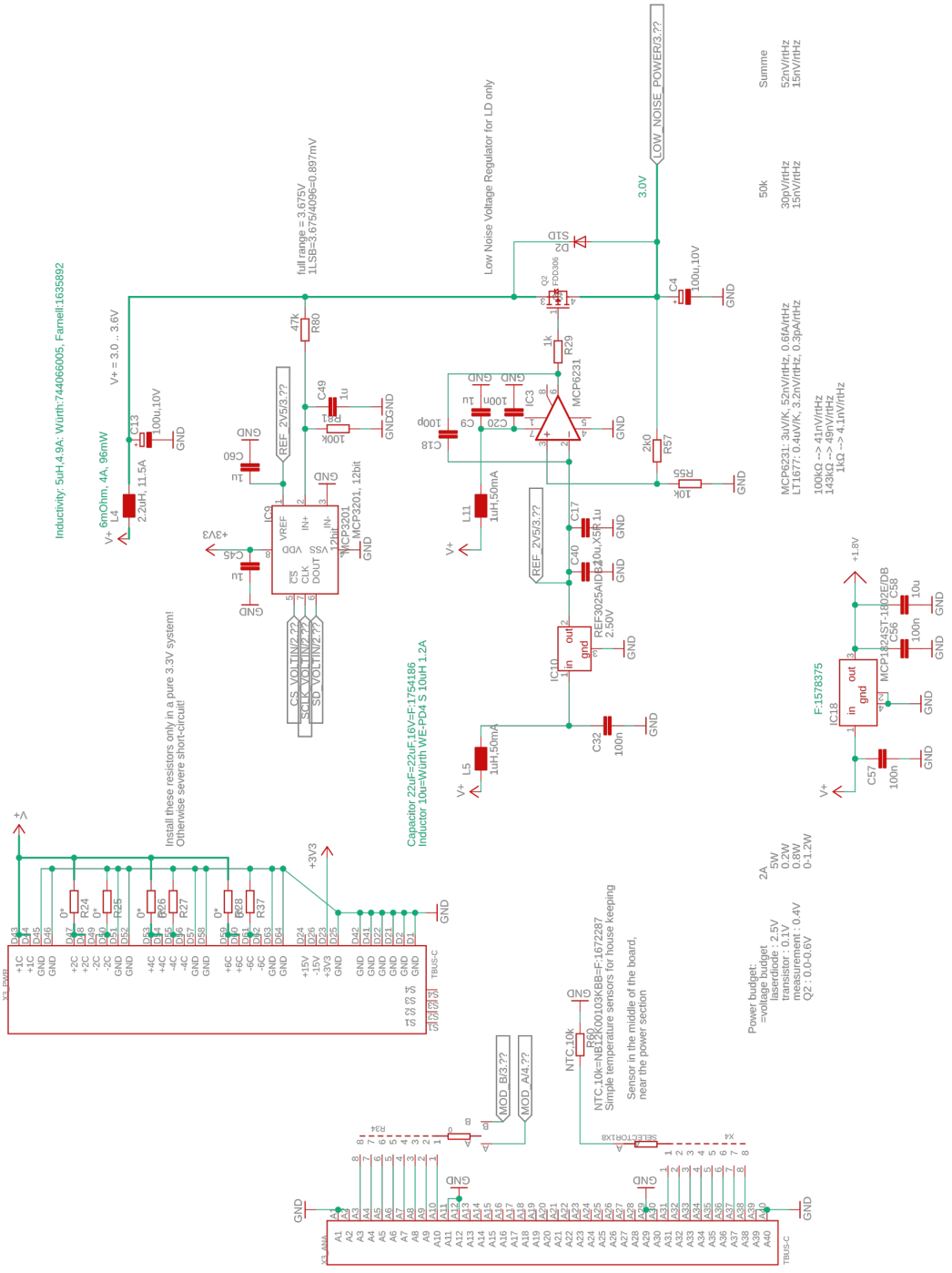

Figure A.9: Schematic of the laser current driver board. This sheet shows the connections of the board between the analog TBus as well as the power supply connection and the electronic components which create a low noise power source for the laser current.

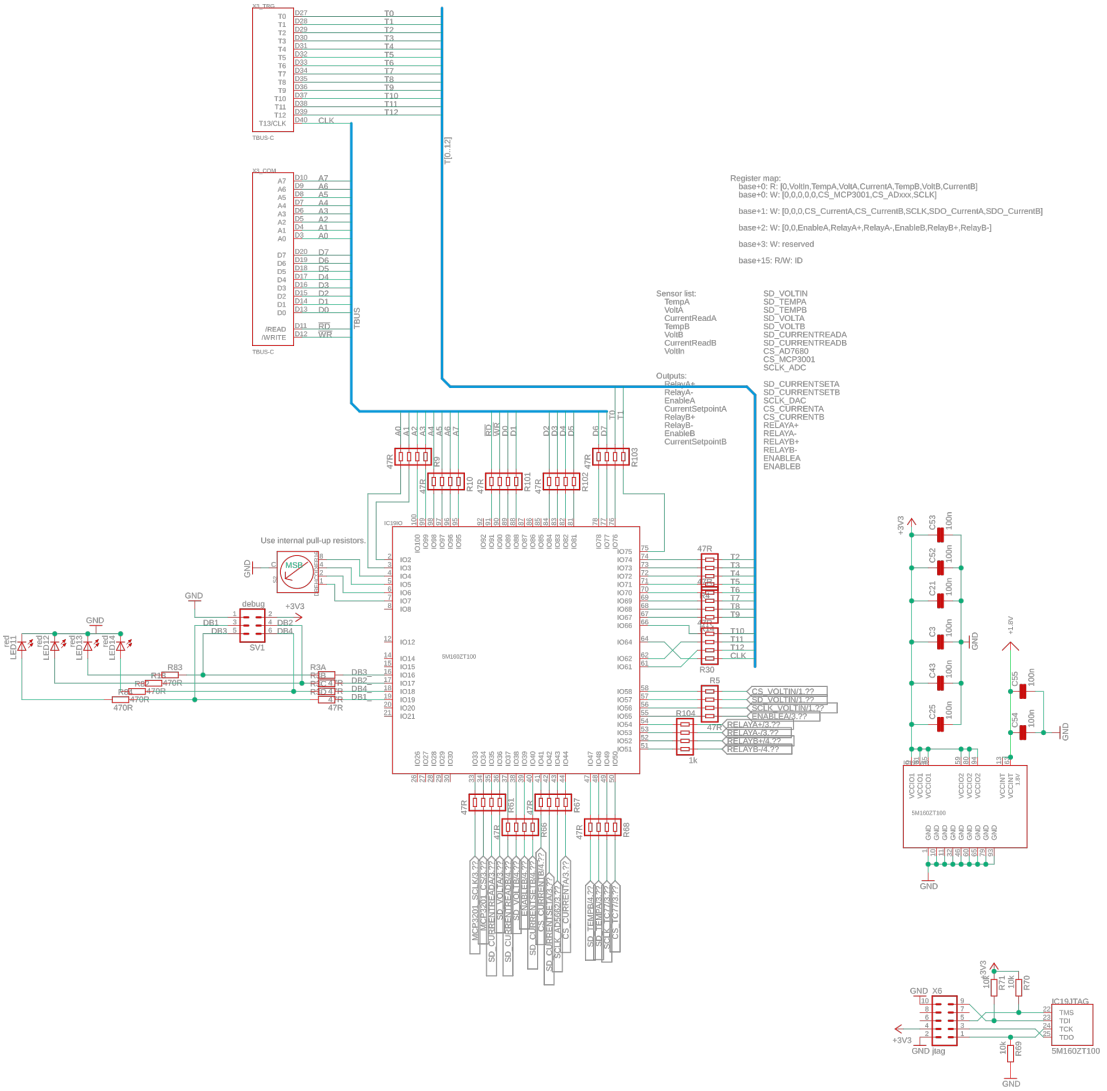

Figure A.10: Schematic of the laser current driver board. This sheet shows the connections of the board between the digital TBus and the FPGA.

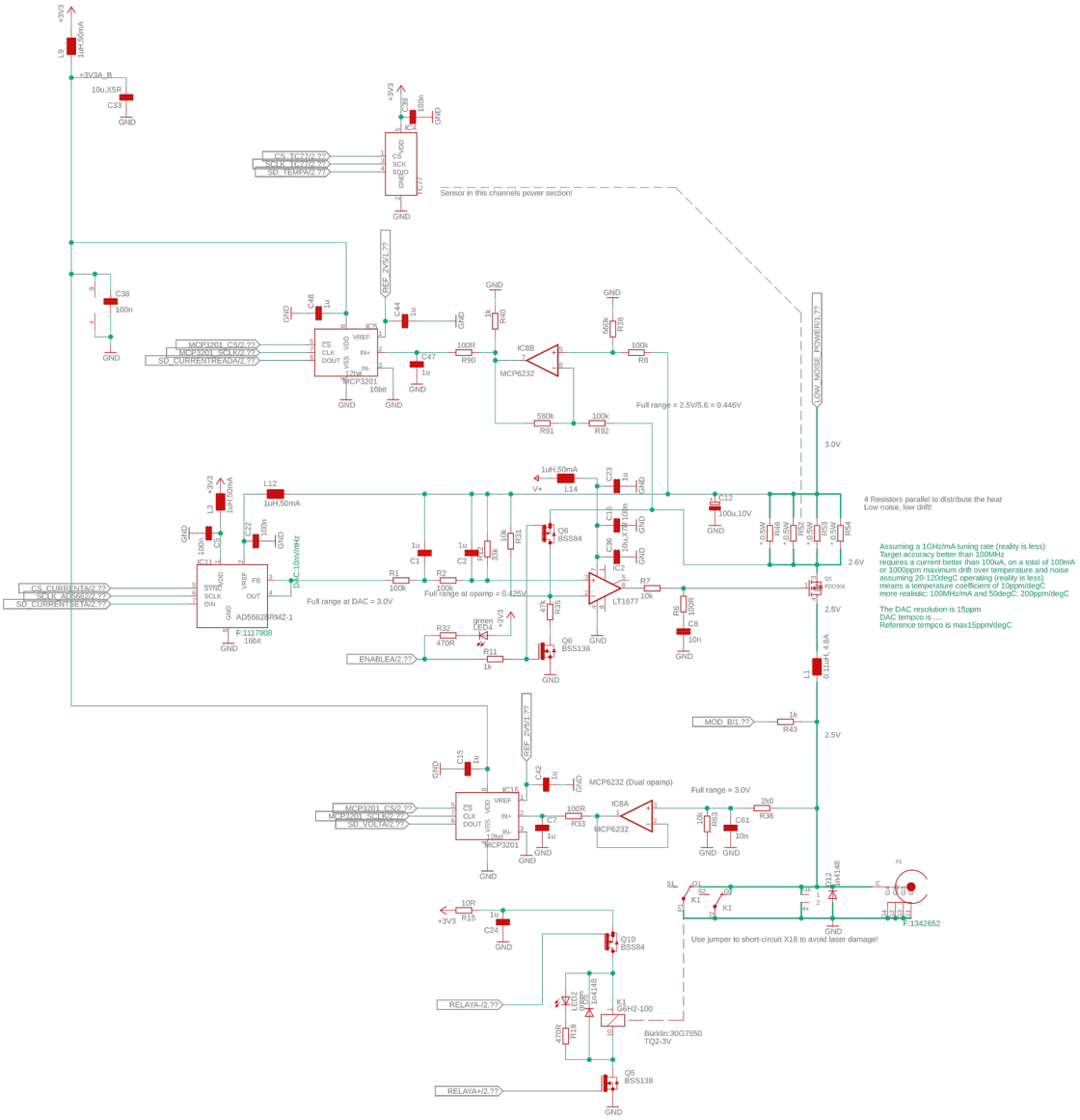

Figure A.11: Schematic of the laser current driver board. This sheet shows one current output of the board. Its solder options set the operating point for the laser current, converted from the low noise $5\,\mathrm{V}$ power source. The output of the laser frequency control board is modulated onto the operating current, which is also shown on this sheet.

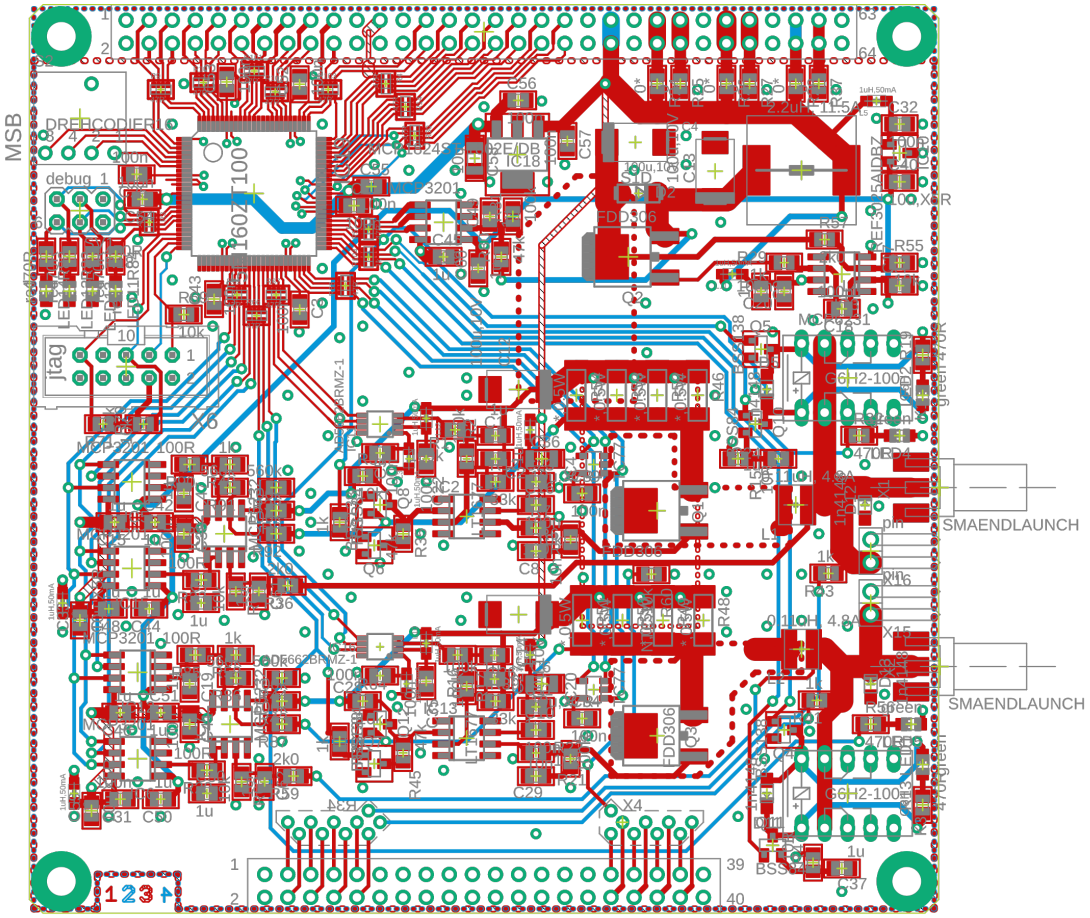

Figure A.12: Illustration of the PCB layout of the laser current driver board.

A.7 Additional measurements

A.7.1 Experimental setups

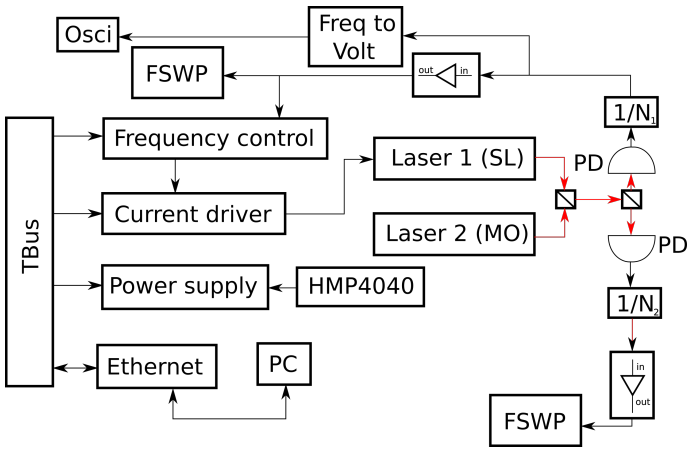

Figure A.13: Jumping setup with ECDLs developed in Berlin for the MAIUS-B experiment.

A.7.2 Spot noise

Table A.1: Spot noise measurement results for the VCO

Signal	Spot Noise	Frequency
VCO free running	$-10.01\,{}^{dBc}/_{\mathrm{Hz}}$	$100\,\mathrm{Hz}$
	$-42.82\,{}^{dBc}/_{\mathrm{Hz}}$	$1\,\mathrm{kHz}$
	$-66.62\,{}^{dBc}/_{\mathrm{Hz}}$	$10\,\mathrm{kHz}$
	$-104.95\,{}^{dBc}/_{\mathrm{Hz}}$	$100\,\mathrm{kHz}$
	$-143.02\,{}^{dBc}/_{\mathrm{Hz}}$	$1\,\mathrm{MHz}$
VCO phaselocked	$-64.19\,{}^{dBc}/_{\mathrm{Hz}}$	$100\,\mathrm{Hz}$
	$-94.42\,{}^{dBc}/_{\mathrm{Hz}}$	$1\,\mathrm{kHz}$
	$-92.95\,{}^{dBc}/_{\mathrm{Hz}}$	$10\,\mathrm{kHz}$
	$-92.96\,{}^{dBc}/_{\mathrm{Hz}}$	$100\,\mathrm{kHz}$
	$-113.43\,{}^{dBc}/_{\mathrm{Hz}}$	$1\,\mathrm{MHz}$

Table A.3: Spot noise measurement results for the reference oscillator, the QPort laser beats and the NCO with active DPLL

Signal	Spot Noise	Frequency
Reference Oscillator	$-95.85\,^{dBc}/_{\mathrm{Hz}}$	100 Hz
	$-131.16\,^{dBc}/_{\mathrm{Hz}}$	1 kHz
	$-138.06\,^{dBc}/_{\mathrm{Hz}}$	10 kHz
	$-132.01\,^{dBc}/_{\mathrm{Hz}}$	100 kHz
	$-133.44\,^{dBc}/_{\mathrm{Hz}}$	1 MHz
NCO with MO locked	$-73.18\,^{dBc}/_{\mathrm{Hz}}$	100 Hz
	$-120.45\,^{dBc}/_{\mathrm{Hz}}$	1 kHz
	$-123.96\,^{dBc}/_{\mathrm{Hz}}$	10 kHz
	$-124.17\,^{dBc}/_{\mathrm{Hz}}$	100 kHz
	$-125.07\,^{dBc}/_{\mathrm{Hz}}$	1 MHz
NCO with free running MO	$-72.85\,^{dBc}/_{\mathrm{Hz}}$	100 Hz
	$-109.71\,^{dBc}/_{\mathrm{Hz}}$	1 kHz
	$-113.46\,^{dBc}/_{\mathrm{Hz}}$	10 kHz
	$-116.32\,^{dBc}/_{\mathrm{Hz}}$	100 kHz
	$-118.28\,^{dBc}/_{\mathrm{Hz}}$	1 MHz
SL locked with locked MO	$-55.13\,^{dBc}/_{\mathrm{Hz}}$	100 Hz
	$-57.07\,^{dBc}/_{\mathrm{Hz}}$	1 kHz
	$-56.40\,^{dBc}/_{\mathrm{Hz}}$	10 kHz
	$-66.99\,^{dBc}/_{\mathrm{Hz}}$	100 kHz
	$-83.85\,^{dBc}/_{\mathrm{Hz}}$	1 MHz
SL locked with MO free running	$-47.55\,^{dBc}/_{\mathrm{Hz}}$	100 Hz
	$-60.15\,^{dBc}/_{\mathrm{Hz}}$	1 kHz
	$-64.46\,^{dBc}/_{\mathrm{Hz}}$	10 kHz
	$-61.24\,^{dBc}/_{\mathrm{Hz}}$	100 kHz
	$-84.51\,^{dBc}/_{\mathrm{Hz}}$	1 MHz

Table A.2: Spot noise measurement results for the NCO and the reference oscillator

Signal	Spot Noise	Frequency
NCO	$-75.41\,^{dBc}/_{\mathrm{Hz}}$	100 Hz
	$-121.37\,^{dBc}/_{\mathrm{Hz}}$	1 kHz
	$-125.62\,^{dBc}/_{\mathrm{Hz}}$	10 kHz
	$-126.51\,^{dBc}/_{\mathrm{Hz}}$	100 kHz
	$-125.65\,^{dBc}/_{\mathrm{Hz}}$	1 MHz
Reference oscillator	$-95.85\,^{dBc}/_{\mathrm{Hz}}$	100 Hz
	$-131.16\,^{dBc}/_{\mathrm{Hz}}$	1 kHz
	$-138.06\,^{dBc}/_{\mathrm{Hz}}$	10 kHz
	$-132.01\,^{dBc}/_{\mathrm{Hz}}$	100 kHz
	$-133.44\,^{dBc}/_{\mathrm{Hz}}$	1 MHz

A.7.3 Frequency to Volt converter characterization

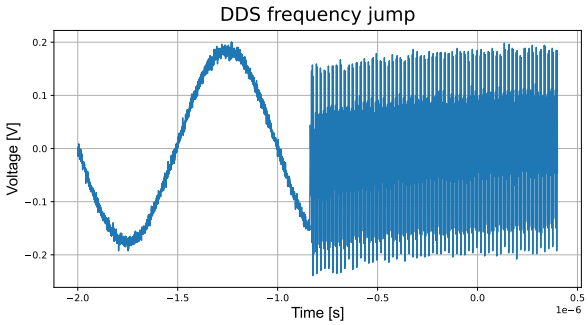

Figure A.14: Illustration of the change in frequency of a DDS in Volt as a function of time. The change in frequency happens in $< 1\ \mu\mathrm{s}$

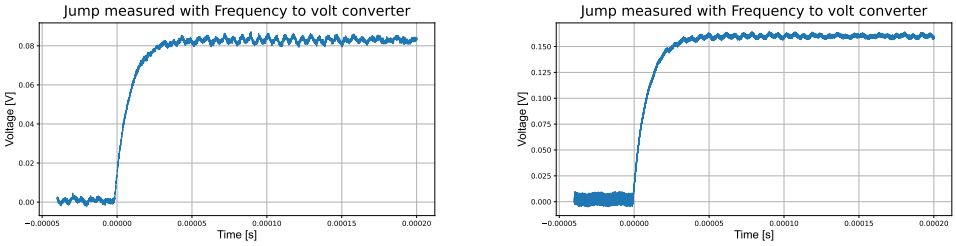

(a) (b)

Figure A.15: Illustration of the change in frequency of a DDS in Volt as a function of time processed by the frequency to volt converter. The curve is close to the measured curves for the laser beat and the limit to how fast the converter reacts is around $35\ \mu\mathrm{s}$ for both jumps over $80\ \mathrm{MHz}$ (illustrated in figure A.15a) and $200\ \mathrm{MHz}$ (illustrated in figure A.15b).

APPENDIX B

Literature

[1] D. A. Steck, "Rubidium 87 D line data," 2001.

[2] W. D. Phillips, "Nobel lecture: Laser cooling and trapping of neutral atoms," *Reviews of Modern Physics*, vol. 70, no. 3, p. 721, 1998.

[3] M. A. Popp, *Compact, low-noise current drivers for quantum sensors with atom chips*. PhD thesis, Gottfried Wilhelm Leibniz Universität Hannover, 2018.

[4] S. Hartmann, J. Jenewein, E. Giese, S. Abend, A. Roura, E. M. Rasel, and W. P. Schleich, "Regimes of atomic diffraction: Raman versus Bragg diffraction in retroreflective geometries," *Physical Review A*, vol. 101, no. 5, p. 053610, 2020.

[5] B. Piest, *Bose-Einstein condensation of K-41 and Rb-87 on an atom chip for sounding rocket missions*. PhD thesis, Gottfried Wilhelm Leibniz Universität Hannover, 2021.

[6] H. Georgi and S. L. Glashow, "Unity of all elementary-particle forces," *Physical Review Letters*, vol. 32, no. 8, p. 438, 1974.

[7] N. Malossi, Q. Bodart, S. Merlet, T. Lévèque, A. Landragin, and F. P. Dos Santos, "Double diffraction in an atomic gravimeter," *Physical review A*, vol. 81, no. 1, p. 013617, 2010.

[8] W. Herr, *Eine kompakte Quelle quantenentarteter Gase hohen Flusses für die Atominterferometrie unter Schwerelosigkeit*. PhD thesis, 2013.

[9] J. Hartwig, S. Abend, C. Schubert, D. Schlippert, H. Ahlers, K. Posso-Trujillo, N. Gaaloul, W. Ertmer, and E. M. Rasel, "Testing the universality of free fall with rubidium and ytterbium in a very large baseline atom interferometer," *New Journal of Physics*, vol. 17, no. 3, p. 035011, 2015.

[10] E. M. Rasel, D. Schlippert, and E. Wodey, "Der VLBAI-teststand: Ein Fallturm für Atome," *Unimagazin 3/4 (2018)*, 2018.

[11] J. Rudolph, W. Herr, C. Grzeschik, T. Sternke, A. Grote, M. Popp, D. Becker, H. Müntinga, H. Ahlers, A. Peters, *et al.*, "A high-flux BEC source for mobile atom interferometers," *New Journal of Physics*, vol. 17, no. 6, p. 065001, 2015.

[12] P. Stromberger, J. Pahl, M. Cornelius, A. Wenzlawski, P. Windpassinger, and C. Deppner, "QUANTUS-2: Quantum gases under microgravity," *43rd COSPAR Scientific Assembly. Held 28 January-4 February*, vol. 43, p. 2143, 2021.

[13] S. T. Seidel, *Eine Quelle für die Interferometrie mit Bose-Einstein-Kondensaten auf Höhenforschungsraketen*. PhD thesis, 2014.

[14] M. D. Lachmann, *Materiewelleninterferenzen im Weltraum*. PhD thesis, Gottfried Wilhelm Leibniz Universität Hannover, 2020.

[15] N. Gaaloul and E. Rasel, "Quantum test of the equivalence principle: The STE-QUEST mission," *Bulletin of the American Physical Society*, vol. 58, 2013.

[16] C. Schubert, J. Hartwig, H. Ahlers, K. Posso-Trujillo, N. Gaaloul, U. Velte, A. Landragin, A. Bertoldi, B. Battelier, P. Bouyer, *et al.*, "Differential atom interferometry with ^{87}Rb and ^{85}Rb for testing the UFF in STE-QUEST," *arXiv preprint arXiv:1312.5963*, 2013.

[17] D. Aguilera, H. Ahlers, B. Battelier, A. Bawamia, A. Bertoldi, R. Bondarescu, K. Bongs, P. Bouyer, C. Braxmaier, L. Cacciapuoti, *et al.*, "STE-QUEST: Test of the universality of free fall using cold atom interferometry," *Classical and Quantum Gravity*, vol. 31, no. 11, p. 115010, 2014.

[18] K. Frye, S. Abend, W. Bartosch, A. Bawamia, D. Becker, H. Blume, C. Braxmaier, S.-W. Chiow, M. A. Efremov, W. Ertmer, *et al.*, "The Bose-Einstein condensate and cold atom laboratory," *EPJ Quantum Technology*, vol. 8, no. 1, p. 1, 2021.

[19] U. Velte, *Orbit simulations and optical phase locking techniques for an atom interferometric test of the universality of free fall*. PhD thesis, Gottfried Wilhelm Leibniz Universität Hannover, 2018.

[20] T. Lévèque, A. Gauguet, F. Michaud, F. P. Dos Santos, and A. Landragin, "Enhancing the area of a Raman atom interferometer using a versatile double diffraction technique," *Physical review letters*, vol. 103, no. 8, p. 080405, 2009.

[21] B. P. Abbott, R. Abbott, T. Abbott, M. Abernathy, F. Acernese, K. Ackley, C. Adams, T. Adams, P. Addesso, R. Adhikari, *et al.*, "Observation of gravitational waves from a binary black hole merger," *Physical review letters*, vol. 116, no. 6, p. 061102, 2016.

[22] P. Berg, S. Abend, G. Tackmann, C. Schubert, E. Giese, W. P. Schleich, F. Narducci, W. Ertmer, and E. Rasel, "Composite-light-pulse technique for high-precision atom interferometry," *Physical review letters*, vol. 114, no. 6, p. 063002, 2015.

[23] K. S. Hardman, P. J. Everitt, G. D. McDonald, P. Manju, P. B. Wigley, M. Sooriyabandara, C. C. Kuhn, J. E. Debs, J. D. Close, and N. P. Robins, "Simultaneous precision gravimetry and magnetic gradiometry with a Bose-Einstein condensate: A high precision, quantum sensor," *Physical review letters*, vol. 117, no. 13, p. 138501, 2016.

[24] A. Einstein, *The meaning of relativity: Including the relativistic theory of the non-symmetric field*, vol. 32. Princeton university press, 2014.

[25] C. Wetterich, "Probing quintessence with time variation of couplings," *Journal of Cosmology and Astroparticle Physics*, vol. 2003, no. 10, p. 002, 2003.

[26] T. Damour, F. Piazza, and G. Veneziano, "Violations of the equivalence principle in a dilaton-runaway scenario," *Physical Review D*, vol. 66, no. 4, p. 046007, 2002.

[27] S. Schlamminger, K.-Y. Choi, T. Wagner, J. Gundlach, and E. Adelberger, "Test of the equivalence principle using a rotating torsion balance," *Physical Review Letters*, vol. 100, no. 4, p. 041101, 2008.

[28] P. Touboul, G. Métris, M. Rodrigues, Y. André, Q. Baghi, J. Bergé, D. Boulanger, S. Bremer, P. Carle, R. Chhun, *et al.*, "Microscope mission: First results of a space test of the equivalence principle," *Physical review letters*, vol. 119, no. 23, p. 231101, 2017.

[29] J. Williams, R. Dicke, P. Bender, C. Alley, W. Carter, D. Currie, D. Eckhardt, J. Faller, W. Kaula, J. Mulholland, *et al.*, "New test of the equivalence principle from lunar laser ranging," *Physical Review Letters*, vol. 36, no. 11, p. 551, 1976.

[30] W. Thijs, "LASUS wiki electronics, Leibniz Univerität Hannover, Institut für Quantenoptik," *Lasus Wiki Electronics*, 2013.

[31] A. Einstein, "Quantentheorie des einatomigen idealen Gases. zweite Abhandlung," *Albert Einstein: Akademie-Vorträge: Sitzungsberichte der Preußischen Akademie der Wissenschaften 1914–1932*, pp. 245–257, 2005.

[32] J. Rudolph, N. Gaaloul, Y. Singh, H. Ahlers, W. Herr, T. A. Schulze, S. T. Seidel, C. Rode, V. Schkolnik, W. Ertmer, *et al.*, "Degenerate quantum gases in microgravity," *Microgravity Science and Technology*, vol. 23, no. 3, pp. 287–292, 2011.

[33] M. Sahelgozin, *Design and construction of a transportable quantum gravimeter and realization of an atom-chip magnetic trap*. PhD thesis, Gottfried Wilhelm Leibniz Universität Hannover, 2019.

[34] M. D. Lachmann, H. Ahlers, D. Becker, A. N. Dinkelaker, J. Grosse, O. Hellmig, H. Müntinga, V. Schkolnik, S. T. Seidel, T. Wendrich, *et al.*, "Ultracold atom interferometry in space," *Nature communications*, vol. 12, no. 1, p. 1317, 2021.

[35] T. van Zoest, N. Gaaloul, Y. Singh, H. Ahlers, W. Herr, S. Seidel, W. Ertmer, E. Rasel, M. Eckart, E. Kajari, *et al.*, "Bose-Einstein condensation in microgravity," *Science*, vol. 328, no. 5985, pp. 1540–1543, 2010.

[36] T. van Zoest, *Realisierung erster quantenentarteter Gase unter Schwerelosigkeit*. PhD thesis, Gottfried Wilhelm Leibniz Universität Hannover, 2008.

[37] D. Becker, M. D. Lachmann, S. T. Seidel, H. Ahlers, A. N. Dinkelaker, J. Grosse, O. Hellmig, H. Müntinga, V. Schkolnik, T. Wendrich, *et al.*, "Space-borne Bose-Einstein condensation for precision interferometry," *Nature*, vol. 562, no. 7727, pp. 391–395, 2018.

[38] W. Bartosch, *The electronic and experimental setup of the MAIUS-2 and MAIUS-3 sounding rocket missions*. PhD thesis, Gottfried Wilhelm Leibniz Universität Hannover, 2021.

[39] T. Muller, T. Wendrich, M. Gilowski, C. Jentsch, E. Rasel, and W. Ertmer, "Sagnac interferometry with cold atoms," in *EQEC'05. European Quantum Electronics Conference, 2005.*, p. 239, IEEE, 2005.

[40] C. Nshii, M. Vangeleyn, J. P. Cotter, P. F. Griffin, E. Hinds, C. N. Ironside, P. See, A. Sinclair, E. Riis, and A. S. Arnold, "A surface-patterned chip as a strong source of ultracold atoms for quantum technologies," *Nature nanotechnology*, vol. 8, no. 5, pp. 321–324, 2013.

[41] H. J. Metcalf and P. Van der Straten, *Laser cooling and trapping*. Springer Science & Business Media, 1999.

[42] W. Demtröder, *Experimentalphysik 3: Atome, Moleküle und Festkörper*. Springer-Verlag, 2016.

[43] S. Chaudhuri, S. Roy, and C. Unnikrishnan, "Realization of an intense cold Rb atomic beam based on a two-dimensional magneto-optical trap: Experiments and comparison with simulations," *Physical Review A*, vol. 74, no. 2, p. 023406, 2006.

[44] K. Dieckmann, R. Spreeuw, M. Weidemüller, and J. Walraven, "Two-dimensional magneto-optical trap as a source of slow atoms," *Physical Review A*, vol. 58, no. 5, p. 3891, 1998.

[45] S. Wildermuth, P. Krüger, C. Becker, M. Brajdic, S. Haupt, A. Kasper, R. Folman, and J. Schmiedmayer, "Optimized magneto-optical trap for experiments with ultracold atoms near surfaces," *Physical Review A*, vol. 69, no. 3, p. 030901, 2004.

[46] P. Krüger, X. Luo, M. W. Klein, K. Brugger, A. Haase, S. Wildermuth, S. Groth, I. Bar-Joseph, R. Folman, and J. Schmiedmayer, "Trapping and manipulating neutral atoms with electrostatic fields," *Physical review letters*, vol. 91, no. 23, p. 233201, 2003.

[47] J. Reichel, W. Hänsel, and T. Hänsch, "Atomic micromanipulation with magnetic surface traps," *Physical Review Letters*, vol. 83, no. 17, p. 3398, 1999.

[48] J. Reichel and V. Vuletic, *Atom chips*. John Wiley & Sons, 2011.

[49] W. Petrich, M. H. Anderson, J. R. Ensher, and E. A. Cornell, "Stable, tightly confining magnetic trap for evaporative cooling of neutral atoms," *Physical Review Letters*, vol. 74, no. 17, p. 3352, 1995.

[50] A. Roura, C. Schubert, D. Schlippert, and E. M. Rasel, "Measuring gravitational time dilation with delocalized quantum superpositions," *Physical Review D*, vol. 104, no. 8, p. 084001, 2021.

[51] D. Schlippert, J. Hartwig, H. Albers, L. L. Richardson, C. Schubert, A. Roura, W. P. Schleich, W. Ertmer, and E. M. Rasel, "Quantum test of the universality of free fall," *Physical Review Letters*, vol. 112, no. 20, p. 203002, 2014.

[52] T. J. Wendrich, *High resolution rotation sensor based on cold atom interferometry*. PhD thesis, Gottfried Wilhelm Leibniz Universität Hannover, 2010.

[53] E. Rasel, "Cold atom optics on ground and in space," in *35th COSPAR Scientific Assembly*, vol. 35, p. 3856, 2004.

[54] P. D. Lett, R. N. Watts, C. I. Westbrook, W. D. Phillips, P. L. Gould, and H. J. Metcalf, "Observation of atoms laser cooled below the Doppler limit," *Physical review letters*, vol. 61, no. 2, p. 169, 1988.

[55] S. Chu, L. Hollberg, J. E. Bjorkholm, A. Cable, and A. Ashkin, "Three-dimensional viscous confinement and cooling of atoms by resonance radiation pressure," *Physical review letters*, vol. 55, no. 1, p. 48, 1985.

[56] J. Dalibard and C. Cohen-Tannoudji, "Laser cooling below the Doppler limit by polarization gradients: simple theoretical models," *JOSA B*, vol. 6, no. 11, pp. 2023–2045, 1989.

[57] C. J. Foot, *Atomic physics*, vol. 7. OUP Oxford, 2004.

[58] C. Adams and E. Riis, "Laser cooling and trapping of neutral atoms," *Progress in quantum electronics*, vol. 21, no. 1, pp. 1–79, 1997.

[59] W. Happer, "Optical pumping," *Reviews of Modern Physics*, vol. 44, no. 2, p. 169, 1972.

[60] H. F. Hess, "Evaporative cooling of magnetically trapped and compressed spin-polarized hydrogen," *Physical Review B*, vol. 34, no. 5, p. 3476, 1986.

[61] M. H. Anderson, J. R. Ensher, M. R. Matthews, C. E. Wieman, and E. A. Cornell, "Observation of Bose-Einstein condensation in a dilute atomic vapor," *science*, vol. 269, no. 5221, pp. 198–201, 1995.

[62] C. C. Bradley, C. Sackett, J. Tollett, and R. G. Hulet, "Evidence of Bose-Einstein condensation in an atomic gas with attractive interactions," *Physical review letters*, vol. 75, no. 9, p. 1687, 1995.

[63] S. Amri, R. Corgier, D. Sugny, E. M. Rasel, N. Gaaloul, and E. Charron, "Optimal control of the transport of Bose-Einstein condensates with atom chips," *Scientific reports*, vol. 9, no. 1, p. 5346, 2019.

[64] P. R. Berman, *Atom interferometry*. Academic press, 1997.

[65] W. Ketterle, "Nobel lecture: When atoms behave as waves: Bose-Einstein condensation and the atom laser," *Reviews of Modern Physics*, vol. 74, no. 4, p. 1131, 2002.

[66] E. A. Cornell and C. E. Wieman, "Nobel lecture: Bose-Einstein condensation in a dilute gas, the first 70 years and some recent experiments," *Reviews of Modern Physics*, vol. 74, no. 3, p. 875, 2002.

[67] H. Ammann and N. Christensen, "Delta kick cooling: A new method for cooling atoms," *Physical review letters*, vol. 78, no. 11, p. 2088, 1997.

[68] J. Rudolph, *Matter-wave optics with Bose-Einstein condensates in microgravity*. PhD thesis, Gottfried Wilhelm Leibniz Universität Hannover, 2016.

[69] T. Kovachy, J. M. Hogan, A. Sugarbaker, S. M. Dickerson, C. A. Donnelly, C. Overstreet, and M. A. Kasevich, "Matter wave lensing to picokelvin temperatures," *Physical review letters*, vol. 114, no. 14, p. 143004, 2015.

[70] E. Maréchal, S. Guibal, J.-L. Bossennec, R. Barbé, J.-C. Keller, and O. Gorceix, "Longitudinal focusing of an atomic cloud using pulsed magnetic forces," *Physical Review A*, vol. 59, no. 6, p. 4636, 1999.

[71] J. Camparo and R. Frueholz, "A dressed atom interpretation of adiabatic rapid passage," *Journal of Physics B: Atomic and Molecular Physics*, vol. 17, no. 20, p. 4169, 1984.

[72] M. Dupont-Nivet, M. Casiulis, T. Laudat, C. I. Westbrook, and S. Schwartz, "Microwave-stimulated Raman adiabatic passage in a Bose-Einstein condensate on an atom chip," *Physical Review A*, vol. 91, no. 5, p. 053420, 2015.

[73] C. Cohen-Tannoudji and S. Reynaud, "Dressed-atom description of resonance fluorescence and absorption spectra of a multi-level atom in an intense laser beam," *Journal of Physics B: Atomic and Molecular Physics*, vol. 10, no. 3, p. 345, 1977.

[74] A. Baksic, H. Ribeiro, and A. A. Clerk, "Speeding up adiabatic quantum state transfer by using dressed states," *Physical review letters*, vol. 116, no. 23, p. 230503, 2016.

[75] T. Sternke, *An ultracold high-flux source for matter-wave interferometry in microgravity*. PhD thesis, Universität Oldenburg, 2018.

[76] W. Bartosch, "Development and demonstration of a laser-system with digital frequency control for atom cooling," Master's thesis, Gottfried Wilhelm Leibniz Universität Hannover, 2015.

[77] L. De Broglie, "Waves and quanta," *Nature*, vol. 112, no. 2815, pp. 540–540, 1923.

[78] B. E. Saleh and M. C. Teich, *Grundlagen der Photonik*. John Wiley & Sons, 2008.

[79] W. Ertmer, R. Blatt, J. Hall, and M. Zhu, "Laser manipulation of atomic beam velocities: Demonstration of stopped atoms and velocity reversal," *Physical review letters*, vol. 54, no. 10, p. 996, 1985.

[80] D. S. Weiss, B. C. Young, and S. Chu, "Precision measurement of the photon recoil of an atom using atomic interferometry," *Physical review letters*, vol. 70, no. 18, p. 2706, 1993.

[81] H. Ahlers, H. Müntinga, A. Wenzlawski, M. Krutzik, G. Tackmann, S. Abend, N. Gaaloul, E. Giese, A. Roura, R. Kuhl, *et al.*, "Double Bragg interferometry," *Physical review letters*, vol. 116, no. 17, p. 173601, 2016.

[82] J. Baudon, R. Mathevet, and J. Robert, "Atomic interferometry," *Journal of Physics B: Atomic, Molecular and Optical Physics*, vol. 32, no. 15, p. R173, 1999.

[83] Y. Ji, Y. Chung, D. Sprinzak, M. Heiblum, D. Mahalu, and H. Shtrikman, "An electronic Mach-Zehnder interferometer," *Nature*, vol. 422, no. 6930, pp. 415–418, 2003.

[84] A. D. Cronin, J. Schmiedmayer, and D. E. Pritchard, "Optics and interferometry with atoms and molecules," *Reviews of Modern Physics*, vol. 81, no. 3, p. 1051, 2009.

[85] J. Kasprzak, M. Richard, S. Kundermann, A. Baas, P. Jeambrun, J. M. J. Keeling, F. Marchetti, M. Szymańska, R. André, J. Staehli, *et al.*, "Bose-Einstein condensation of exciton polaritons," *Nature*, vol. 443, no. 7110, pp. 409–414, 2006.

[86] S. Christopoulos, G. B. H. Von Högersthal, A. Grundy, P. Lagoudakis, A. Kavokin, J. Baumberg, G. Christmann, R. Butté, E. Feltin, J.-F. Carlin, *et al.*, "Room-temperature polariton lasing in semiconductor microcavities," *Physical review letters*, vol. 98, no. 12, p. 126405, 2007.

[87] S. Abend, *Atom-chip gravimeter with Bose-Einstein condensates*. PhD thesis, Gottfried Wilhelm Leibniz Universität Hannover, 2017.

[88] C. J. Bordé, "Atomic interferometry with internal state labelling," *Physics letters A*, vol. 140, no. 1-2, pp. 10–12, 1989.

[89] M. Kozuma, L. Deng, E. W. Hagley, J. Wen, R. Lutwak, K. Helmerson, S. Rolston, and W. D. Phillips, "Coherent splitting of Bose-Einstein condensed atoms with optically induced Bragg diffraction," *Physical Review Letters*, vol. 82, no. 5, p. 871, 1999.

[90] M. Kasevich and S. Chu, "Atomic interferometry using stimulated Raman transitions," *Physical review letters*, vol. 67, no. 2, p. 181, 1991.

[91] F. Sorrentino, K. Bongs, P. Bouyer, L. Cacciapuoti, M. De Angelis, H. Dittus, W. Ertmer, A. Giorgini, J. Hartwig, M. Hauth, *et al.*, "A compact atom interferometer for future space missions," *Microgravity Science and Technology*, vol. 22, pp. 551–561, 2010.

[92] J. M. Hogan, D. Johnson, and M. A. Kasevich, "Light-pulse atom interferometry," *arXiv preprint arXiv:0806.3261*, 2008.

[93] B. Barrett, L. Antoni-Micollier, L. Chichet, B. Battelier, T. Lévèque, A. Landragin, and P. Bouyer, "Dual matter-wave inertial sensors in weightlessness," *Nature communications*, vol. 7, no. 1, p. 13786, 2016.

[94] D. Schlippert, *Quantum tests of the universality of free fall*. PhD thesis, Gottfried Wilhelm Leibniz Universität Hannover, 2014.

[95] F. Riehle, *Frequency standards: basics and applications*. John Wiley & Sons, 2006.

[96] J. Rutman, "Characterization of phase and frequency instabilities in precision frequency sources: Fifteen years of progress," *Proceedings of the IEEE*, vol. 66, no. 9, pp. 1048–1075, 1978.

[97] J. Crawford, *Advanced phase-lock techniques*. Artech, 2007.

[98] C. Jentsch, *Konzeption und Aufbau eines Experimentes zur quantenlimitierten Inertialsensorik mit lasergekühlten Rubidiumatomen*. PhD thesis, Gottfried Wilhelm Leibniz Universität Hannover, 2004.

[99] D. Banerjee, *PLL performance, simulation and design*. Dog Ear Publishing, 2006.

[100] S. H. Yim, S.-B. Lee, T. Y. Kwon, and S. E. Park, "Optical phase locking of two extended-cavity diode lasers with ultra-low phase noise for atom interferometry," *Applied Physics B*, vol. 115, pp. 491–495, 2014.

[101] W. F. Egan, *Phase-lock basics*. John Wiley & Sons, 2007.

[102] F. M. Gardner, *Phaselock techniques*. John Wiley & Sons, 2005.

[103] P. Horowitz and W. Hill, *The Art of Electronics*. Cambridge University Press Cambridge, 2002.

[104] L. Zhou, S. Long, B. Tang, X. Chen, F. Gao, W. Peng, W. Duan, J. Zhong, Z. Xiong, J. Wang, *et al.*, "Test of equivalence principle at 10^{-8} level by a dual-species double-diffraction Raman atom interferometer," *Physical review letters*, vol. 115, no. 1, p. 013004, 2015.

[105] K. Wang, Z. Yao, R. Li, S. Lu, X. Chen, J. Wang, and M. Zhan, "Hybrid wide-band, low-phase-noise scheme for Raman lasers in atom interferometry by integrating an acousto-optic modulator and a feedback loop," *Applied Optics*, vol. 55, no. 5, pp. 989–992, 2016.

[106] T. Schuldt, C. Schubert, M. Krutzik, L. G. Bote, N. Gaaloul, J. Hartwig, H. Ahlers, W. Herr, K. Posso-Trujillo, J. Rudolph, *et al.*, "Design of a dual species atom interferometer for space," *Experimental Astronomy*, vol. 39, pp. 167–206, 2015.

[107] S. Lu, Y. Zhou, F. Zhu, J. Sun, Y. Yang, R. Zhu, S. Hu, X. Zhang, X. Zhu, X. Hou, *et al.*, "Digital-analog hybrid optical phase-lock loop for optical quadrature phase-shift keying," *Chinese Optics Letters*, vol. 18, no. 9, p. 090602, 2020.

[108] M. Kumm, H. Klingbeil, and P. Zipf, "An FPGA-based linear all-digital phase-locked loop," *IEEE Transactions on Circuits and Systems I: Regular Papers*, vol. 57, no. 9, pp. 2487–2497, 2010.

[109] A. Papakonstantinou, "Development of an all-digital FPGA-based laser phaselock," Master's thesis, Gottfried Wilhelm Leibniz Universität Hannover, 2017.

[110] Z. Xu, K. Huang, and X. Lu, "A digital optical phase-locked loop based on field programmable gate array and its applications," vol. 2, pp. 795–799, 2014.

[111] B. Zhao and D. L. Yan, "A low-power digital design of all digital PLL for 2.4 g wireless communication applications," in *2016 International Symposium on Integrated Circuits (ISIC)*, pp. 1–4, IEEE, 2016.

[112] P. N. Yelne and P. T. Karule, "Design of frequency modulated receiver using digital phase locked loop," in *2015 International Conference on Communications and Signal Processing (ICCSP)*, pp. 0889–0892, IEEE, 2015.

[113] M. Fuentes, P. Zinemanas, P. Cancela, and J. A. Apolinário, "Detection of enf discontinuities using PLL for audio authenticity," in *2016 IEEE 7th Latin American Symposium on Circuits & Systems (LASCAS)*, pp. 79–82, IEEE, 2016.

[114] J. Brown, "A digital phase and frequency-sensitive detector," *Proceedings of the IEEE*, vol. 59, no. 4, pp. 717–718, 1971.

[115] M. Soyuer and R. G. Meyer, "Frequency limitations of a conventional phase-frequency detector," *IEEE Journal of solid-state circuits*, vol. 25, no. 4, pp. 1019–1022, 1990.

[116] M. D. Book, "Phase-locked loop systems," *Motorola Semiconductor Products Inc.*,, 1973.

[117] J. Lunze, *Regelungstechnik 1*, vol. 10. Springer, 2013.

[118] J. Crowe, K. Tan, T. Lee, R. Ferdous, M. Katebi, H.-P. Huang, J.-C. Jeng, K. Tang, G. Chen, K. Man, *et al.*, *Phase-locked loop methods and PID control*. Springer, 2005.

[119] J. Lunze, *Regelungstechnik 2*, vol. 6. Springer, 2005.

[120] M. A. Johnson and M. H. Moradi, *PID control*. Springer, 2005.

[121] G. C. Goodwin, S. F. Graebe, M. E. Salgado, *et al.*, *Control system design*, vol. 240. Prentice Hall Upper Saddle River, 2001.

[122] V. F. Kroupa, *Direct digital frequency synthesizers*. John Wiley & Sons, 1998.

[123] Intel, "Intel MX 10 FPGA device datasheet."

[124] A. Das, S. Dash, A. Sahoo, and B. C. Babu, "Design and implementation of FPGA based linear all digital phase-locked loop," in *2012 Annual IEEE India Conference (INDICON)*, pp. 280–285, IEEE, 2012.

[125] R. und Schwarz, "R & S FSWP phase noise analyzer and VCO tester."

[126] R. und Schwarz, "R & S RTM3000 oscilloscope."

[127] R. und Schwarz, "R & S HMP4040 Netzgerät."

[128] O. Semiconductor, "MC12093 low power prescaler with stand-by mode."

[129] T. Instruments, "DAC5672 14 bit 275 MSPS."

[130] K. Libbrecht and J. L. Hall, "A low-noise high-speed diode laser current controller," *Review of scientific instruments*, vol. 64, no. 8, pp. 2133–2135, 1993.

[131] M. Elsen, B. Piest, F. Adam, O. Anton, P. Arciszewski, W. Bartosch, D. Becker, J. Böhm, S. Boles, K. Döringshoff, *et al.*, "A dual-species atom interferometer payload for operation on sounding rockets," *arXiv preprint arXiv:2305.08634*, 2023.

[132] Minicircuits, "POS-300+ datasheet."

[133] Abracon, "OCXO AOCJY2-E 10MHz."

[134] S. Bode, "Realization of a laser system for the generation of a ^{87}Rb BEC," Diplomarbeit, Gottfried Wilhelm Leibniz Universität Hannover, 2011.

[135] K. Stolzenberg, "Realisation of a phase stabilised laser system for the manipulation of quantum degenerate gases," Master's thesis, Gottfried Wilhelm Leibniz Universität Hannover, 2018.

[136] N. Photonics, "Koheras HARMONIC fiber laser system."

[137] A. Herbst, "A laser system for testing the MAIUS-B payload," Master's thesis, Gottfried Wilhelm Leibniz Universität Hannover, 2018.

[138] Minicircuits, "ZFL-500LN+ amplifier."

[139] E. Luvsandamdin, C. Kürbis, M. Schiemangk, A. Sahm, A. Wicht, A. Peters, G. Erbert, and G. Tränkle, "Micro-integrated extended cavity diode lasers for precision potassium spectroscopy in space," *Optics express*, vol. 22, no. 7, pp. 7790–7798, 2014.

[140] C. Kürbis, A. Bawamia, M. Krueger, R. Smol, A. Peters, A. Wicht, and G. Tränkle, "Extended cavity diode laser master-oscillator-power-amplifier for operation of an iodine frequency reference on a sounding rocket," *Applied Optics*, vol. 59, no. 2, pp. 253–262, 2020.

[141] A. Wicht, A. Bawamia, M. Krüger, C. Kürbis, M. Schiemangk, R. Smol, A. Peters, and G. Tränkle, "Narrow linewidth diode laser modules for quantum optical sensor applications in the field and in space," in *Components and packaging for laser systems III*, vol. 10085, pp. 103–118, SPIE, 2017.

[142] M. He, X. Chen, J. Fang, G. Ge, J. Li, D. Zhang, L. Zhou, J. Wang, and M. Zhan, "Phase shift of double-diffraction Raman interference due to high-order diffraction states," *Physical Review A*, vol. 103, no. 6, p. 063310, 2021.

[143] W. Li, X. Pan, N. Song, X. Xu, and X. Lu, "A phase-locked laser system based on double direct modulation technique for atom interferometry," *Applied Physics B*, vol. 123, pp. 1–8, 2017.

[144] Z.-K. Hu, B.-L. Sun, X.-C. Duan, M.-K. Zhou, L.-L. Chen, S. Zhan, Q.-Z. Zhang, and J. Luo, "Demonstration of an ultrahigh-sensitivity atom-interferometry absolute gravimeter," *Physical Review A*, vol. 88, no. 4, p. 043610, 2013.

[145] B. Canuel, F. Leduc, D. Holleville, A. Gauguet, J. Fils, A. Virdis, A. Clairon, N. Dimarcq, C. J. Bordé, A. Landragin, *et al.*, "Six-axis inertial sensor using cold-atom interferometry," *Physical review letters*, vol. 97, no. 1, p. 010402, 2006.

[146] J. Le Gouët, T. Mehlstäubler, J. Kim, S. Merlet, A. Clairon, A. Landragin, and F. Pereira Dos Santos, "Limits to the sensitivity of a low noise compact atomic gravimeter," *Applied Physics B*, vol. 92, pp. 133–144, 2008.

[147] X. Baillard, A. Gauguet, S. Bize, P. Lemonde, P. Laurent, A. Clairon, and P. Rosenbusch, "Interference-filter-stabilized external-cavity diode lasers," *Optics Communications*, vol. 266, no. 2, pp. 609–613, 2006.

[148] M. Krutzik, *Matter wave interferometry in microgravity*. PhD thesis, Humboldt-Universität zu Berlin, 2014.

APPENDIX C

List of abbreviations

NASA National Aeronautics and Space Administration

DPLL digital phase locked loop

MAIUS Materiewelleninterferometer unter Schwerelosigkeit

QUANTUS Quantengase unter Schwerelosigkeit

BECCAL Bose-Einstein Condensate and Cold Atom Laboratory

MOT magneto-optical trap

DFB distributed feedback

DLR Deutsches Zentrum für Luft und Raumfahrt

DKC Delta kick collimation

ECDL external cavity diode laser

AC alternating current

DC direct current

DAC digital analog converter

ADC analog digital converter

MOT magneto-optical trap

FPGA field programmable gate array

FFT fast Fourier transform

PID proportional integral derivative

AOM acousto-optic modulator

rms root mean square

FTW frequency tuning word

BEC Bose-Einstein-Condensate

ISS International Space Station

POF plastic optical fibre

LASUS Laser unter Schwerelosigkeit

DDS Direct Digital Synthesizer

PLL Phase Locked Loop

NCO Numeric Controlled Oscillator

VCO Voltage Controlled Oscillator

IC Integrated Circuit

PFD Phase Frequency Detector

LVDS low volt differential signalling

AI atom interferometer

2D-MOT 2-dimensional magneto-optical trap

3D-MOT 3-dimensional magneto-optical trap

3D-chipMOT 3-dimensional chip magneto-optical trap

C-MOT Compression magneto-optical trap

EEP Einstein Equivalence Principle

UFF universality of the free fall

MSB most significant bit

ARP Adiabatic rapid passage

TRC Twisted Ring Counter

RF radio frequency

MZI Mach-Zehnder interferometer

PCB printed circuit board

IC integrated circuit

FWHM full width half maximum

RBW resolution bandwidth

MO master oscillator

SL slave oscillator

APPENDIX D

Puplications

- M. Elsen, B. Piest, F. Adam, O. Anton, P. Arciszewski, W. Bartosch, D. Becker, J. Böhm, S. Boles, K. Döringshoff, A. Papakonstantinou et al., "A dual-species atom interferometer payload for operation on sounding rockets", arXiv preprint arXiv:2305.08634, 2023
- Frye, Kai and Abend, Sven and Bartosch, Wolfgang and Bawamia, Ahmad and Becker, Dennis and Blume, Holger and Braxmaier, Claus and Chiow, Sheng-Wey and Efremov, Maxim A and Ertmer, Wolfgang and Papakonstantinou, Alexandros et. al., "The Bose-Einstein condensate and cold atom laboratory", 2021

APPENDIX E

Acknowledgments

E.1 Acknowledgments

Diese Arbeit wurde in den 6 Jahren ihrer Entstehung von vielen Menschen beinflusst, geprägt und unterstützt. Diesen Menschen möchte ich an dieser Stelle danken.
Starten möchte ich mit Ernst Rasel, da ohne ihn diese Arbeit garnicht erst möglich gewesen wäre. Nachdem ich bereits die Master Arbeit erfolgreich bestanden hatte und den Entschluss gefasst hatte, dass ich noch gerne eine Promotion machen möchte, gab er mir quasi blindes Vertrauen mit den Worten: "Das ist super, dass der Thijs einen weiteren Kollegen für das Elektronik Team gewinnen konnte", woraufhin ich eingestellt wurde. Dies bringt mich direkt zum nächsten Kollegen, welchem ich besonderen Dank aussprechen möchte: Thijs Wendrich.
Thijs hat mich als unbeschriebenes Blatt während des Studiums als HiWi eingestellt, mit ebenfalls quasi blindem Vertrauen unter der einzigen prämisse, dass ich mich reinhänge und offen bin, neue Sachen zu lernen. Aufgrund meines bereits bestehenden Interesses an Elektronik, viel es mir nicht schwer, mich für seine jahrelange Arbeit in den Projekten der QUANTUS Familie zu begeistern. Vielen Dank, dass du immer ein offenes Ohr hattest und egal welche Frage aufkam, du mir immer geholfen hast. Vielen Dank natürlich auch für das Korrekturlesen der Arbeit. Entschuldigung an dieser Stelle, für meine doch sehr ungewöhnlichen Arbeitszeiten, welche dieses Jahr während des Zusammenschreibens doch sehr ausgeartet sind. Ich verspreche, ab jetzt wird es besser.
Den nächsten Kollegen denen ich danken möchte sind Wolle, Isa und Christian während der gemeinsamen Zeit im Elektronik Team im gemeinsamen Büro. Das Team kann wirklich niemand beschreiben, es gab so viele unzählige Momente, wo wir im Büro so laut gelacht haben, dass es alle Nachbarn mitbekommen haben, wegen Sachen, an die ich mich nichtmal erinnern kann. Genauso viele Momente gab es auch, wo wir lautstark über Probleme in der Elektronik diskutiert haben und sie so gemeinsam lösen konnten. Ruhig diskutieren können alle, lautstark diskutieren und dann die Lösung finden nicht. Nicht zu vergessen möchte ich Matthias Koch noch danken, welcher remote immer für Fragen bzgl. der Firmware zur Verfügung stand und meine Arbeit ebenfalls korrekturgelesen hat.
Den nächsten Personen denen ich danken möchte sind alle Kollegen aus dem MAIUS und BECCAL Projekt und aus den Institut. Besonderer Dank gilt hierbei Baptist und Jonas, welche mich bei den Messungen am MAIUS-B Experiment tatkräftig unterstützt haben und Pawel, welcher mir beim Debuggen der Firmware sehr unter die Arme gegriffen hat. Aber hier hat die Hilfe nicht aufgehört, nach Feierabend und hier ebenfalls ab und zu schreiend, aber immer freundlich, wurden Problemlösungen voran getrieben... There's a pattern here as you can see. And by the way, sorry for my taste in music, that you needed to go through when it was my turn in the lab. Your playlists will probably never recover.
Sebastian und Knut vom benachbarten QPort Experiment bin ich ebenfalls großen Dank verschuldet. Nicht nur habt ihr mir bei der Charakaterisierung des Phasenlocks euer Lasersystem zur Verfü-

gung gestellt, bei Problemen wenn es nicht funktionieren wollte, habt ihr mir auch sehr geholfen beim debuggen, sei es durch euer Fachwissen oder durch eure motivierenden Sprüche wie z.B. "Komm, wie schwer kann das sein". Auch wenn ihr danach einen Knall oder einen Schreikrampf gekriegt habt... Schreien, da war doch was...
Weiteren langjährigen Kollegen, mit denen ich bereits seit Beginn des Studiums das Vergnügen hatte sie zu kennen und gemeinsam zu arbeiten möchte ich hier auch danken. Dies wären z.B. Matze, Hendrik und Nina. Mit Hendrik und Nina habe ich ganz zu Beginn der Promotion zusammen im Labor gearbeitet und Matze ist gegen Ende im Nachbarbüro eingezogen und hat mir sehr geholfen, dass er einem Elektroniker wie mir mit der Atominterferometrie auf die Sprünge geholfen hat. Das sind natürlich nicht ansatzweise alle ehemaligen und aktuellen Kollegen. Diesen möchte ich an dieser Stelle gesammelt danken.
Einen ebenfalls großen Beitrag und deswegen zu großen Dank bin ich Silke Ospelkaus, Luis Santos und Sven Herrmann verpflichtet, welche sich bereiterklärt haben diese Arbeit zu begutachten.
Bei Dienstreisen, Vertragsverlängerungen, Planung des Dänemark Seminars, auch beim Promotionsverfahren und jeglichem anderen bürokratischen Notfall war das Sekrätariat stets zur Stelle mir zu helfen. Deswegen möchte ich hier auch meinen Dank aussprechen an Anne-Dore Göldner-Pauer, Stephanie Kaisik, Madeleine-Yasmin Miltsch, Birgit Ohlendorf, Tatjana Loos und Bianca Thiel, wo ich immer mit einem Lächeln empfangen wurde.
Meinen Freunden möchte ich natürlich auch danken und mitteilen: Ab jetzt bin ich wieder entspannter. Vielen Dank für die Hilfe, wenn ich sie mal brauchte aber vor allem für die Aufmunterung und die Motivation, wenn ich mal einen downer hatte, was zum Glück nur selten war. Dies geht an Andi, Kay, Jan, Wolle, Isa, Börje, Dome und Andre.
Schlussendlich möchte ich meiner Familie danken und da bereits die Kurzfassung auf griechisch war, tue ich dies an dieser Stelle auch.
Στέφανε, μαμά, μπαμπά, σας ευχαριστώ πάρα πολλή που με υποστήριξατε τώσα χρόνια, άλλα ιδιαίτερα φέτος όταν δεν ευκαιρούσα να κανονίσω τίποτα εκτός άπο δουλειά, φαΐ και ύπνο. Πάρα πολλά φιλιά. Παππού και γιαγιά (και οι δύο βεβαίως), σας ευχαριστώ και έσας για την αγαπή. Σας αγαπώ όλους. Και όλοι η οικογένεια στην Ελλάδα, χαιρετισμούς και φιλάκια. Κωνσταντίνα, σ΄ ευχαριστώ πολλή που διόρθωσες την περήληψη μου.
Γιώργο, Αλέκο, Χρήστο, Σταύρο και Κώστα, το γράψιμο κάτο στα κόκκινα τραπέζια και στην βιβλιοθήκη ολή την νύχτα ήτανε τέλεια, με βοήθησε πολλή. Σας ευχαριστώ και εσάς, που το αντέξατε μαζί μου. Πάμε όλοι μαζί ταξίδι τον επόμενο χρόνο (το μπάρ στην Θεσσαλονίκη και για ταξίδι εννοώ), για Χαβάη... με μια ρόδα.

E.2 Eigenständigkeitserklärung

Erklärung der Eigenständigkeit
Hiermit versichere ich, die vorliegende Arbeit eigenständig verfasst und keine anderen als die angegebenen Quellen und Hilfsmittel benutzt sowie die Zitate deutlich kenntlich gemacht zu haben.

(Alexandros Papakonstantinou)